VALERIYA BOSHERNITSAN

# ELECTRICAL CHARACTERIZATION OF RESISTIVE SWITCHING DEVICES

UNIVERSIDADE DO ALGARVE

Faculdade de Ciências e Tecnologia

2023

**VALERIYA BOSHERNITSAN**

# ELECTRICAL CHARACTERIZATION OF RESISTIVE SWITCHING DEVICES

**PhD thesis in Electronic Engineering and Telecommunications (Specialty in Electronics and Optoelectronics)**

**Work done under the supervision of:**

**Supervisor: Prof. Henrique Leonel Gomes**

**Co-supervisor: Prof. José Fernando Morais Lopes Mariano**

**UNIVERSIDADE DO ALGARVE**

Faculdade de Ciências e Tecnologia

2023

# Electrical characterization of resistive switching devices

## Declaração de autoria de trabalho:

Declaro ser a autora deste trabalho, que é original e inédito. Autores e trabalhos consultados estão devidamente citados no texto e constam na listagem de referências incluída.

Candidata

_____

(Valeriya Boshernitsan)

# Acknowledgements

I dedicate my dissertation to my beloved grandfather, he was a famous scientist, professor of Physics, he worked for many years as a Dean of the Faculty of Physics at Odessa Mechnikov National University (Ukraine). My grandfather's name is Georgiy G. Chemeresuk. He was a pure decent person, always helpful and empathic. He was for me an example of a real scientist and a respectable, kind-hearted, sensitive person, and who, unfortunately, did not live enough to see the day of my PhD defense. I spent my childhood with my grandfather in the laboratories of the Faculty of Physics, where science was created, and great discoveries were made. From him, I inherited a love for science, a desire to make this world a better place.

And I want to thank my mother, a famous professor of Neurology, Inna Chemeresiuk, who always supports me in everything in my life, who teaches me by her own example to be strong and never ever give up, to help and support people, to work hard and believe in a better future. My family's example inspired me, and they always supported me in my academic journey.

As a scientist, I want to work for peace and prosperity on Earth. I will teach my students not only Science, but I will also teach them to be good people - kind, decent and honest.

I would like to express my sincere gratitude to my teachers - professors from Odessa, Prof. Valentyn Smyntyna and Prof. Valentyna Skobeeva, for their supervision, support, guidance, and all kinds of help provided during my research. As well as the scientific and personal support of Professor Yuriy Vaksman, Nikolay Malushin, Prof. Yuriy Nitsuk and other colleagues from Odessa I.I. Mechnikov National University.

It is my great pleasure to thank all professors and colleagues that were our collaborators during this research project, for their help, encouragement, and support.

In particular, I would like to thank to Dago de Leeuw (Philips laboratories in Eindhoven, Netherlands) for providing the LiF diodes. Anabela Rolo (Universidade do Minho) for her support in characterization of the nanoparticles, Prof. Eberhard Burkel (Rostock University, Germany) for taken some of the scanning electron photographs of the nanocomposites, Ana Rosa da Costa (Universidade do Algarve, Portugal) for her support in the preparation of the nanocomposites at the Chemistry Department.

I would like to thank the University of Algarve and my supervisor Prof. Henrique Leonel Gomes for providing the research environment and scientific support.

**Acknowledgements: Final support**

This work would not have been possible without funding provided by the Instituto de Telecomunicações, FCT/MCTES through national funds and co-funded by the EU funds under Project UIDB/EEA/50008/2020.


# Abstract

The aim of this thesis is to investigate the electrical properties of resistive switching memories. Two distinct device architectures were explored. One involves a sandwich type of structure based on lithium fluoride (LiF) thin film, and the other is based on the integration of cadmium sulfide (CdS) nanoparticles within various polymer matrices.

The research work encompasses the fabrication and detailed morphological and electrical characterization of the fabricated devices. Electrical and optical measurementscarried were complemented by a morphological characterization of CdS nanoparticles. A variety of electrical techniques, namely, current-voltage measurements, small-signal impedance, constant current stress, and electrical noise-based techniques were used to characterize the devices. The CdS nanoparticles were embedded in different insulating host matrices, including photographic gelatin, polyvinylpyrrolidone (PVP), polystyrene sulfonate ($PSS_{Na}$) and dimethylformamide (DMF). The physical and chemical properties of CdS nanoparticles in those different matrices were investigated. CdS nanoparticles (NPs) have beencharacterized using several techniques such as XRD and SEM analysis, absorption, and photoluminescence (PL) emission spectroscopy. This characterization allowed us to establish the structure of the thin films as well as the role of the pH values, the type of host polymer matrix on the nanoparticle's stabilization. Free-standing films prepared using a highconcentration of nanoparticles in a PVP host matrix were also electrically characterized.

Both types of device structures, the LiF diodes and the CdS based devices undergo an electroforming process that permanently modifies their electrical properties. In the case of LiF diodes, the electroforming creates defects that lead to a memory device with two well-defined resistive states. In the case of the CdS nanoparticles embedded in a PVP matrix, electroforming changes the behavior from a semiconducting type to an insulating behavior. The physical phenomena that lead to the permanently induced changes are discussed in detail. In the case of the CdS the electroforming is described as a Coulomb blockade that leads to the formation of a nanodielectric type of material. In the LiF-based diodes electroforming is described as due to the formation of electrical bistable defects on the LiF layer.

.

**Keywords:** CdS nanoparticles, LiF, non-volatile memory, Negative Differential Resistance (NDR), Resistive Switching, Electrical characterization.

# Resumo extenso

O objetivo desta tese foi estudar as propriedades elétricas de componentes eletrónicos emergentes. Nomeadamente foram estudadas memórias de comutação resistiva onde a camada ativa é um filme fino de fluoreto de lítio (LiF). Foram também estudados dispositivosfabricados com nanopartículas de Sulfeto de cádmio (CdS) embebidas numa matriz poliméricaisolante. As memórias de comutação resistiva (RRAM) baseiam-se na alteração da resistênciaelétrica de um material ou componente quando submetido a uma tensão elétrica.

Esta tese está dividida em duas componentes científicas distintas de acordo com o tipo de material estudado. Uma parte desta tese incidiu nas propriedades elétricas das memórias resistivas fabricadas com fluoreto de lítio (LiF) e um polímero semicondutor, o espirofluoreno. A segunda parte desta tese incidiu sobre nanopartículas de sulfato de cádmio (CdS) incorporadas numa matriz polimérica isoladora.

Ambos os dispositivos foram caracterizados extensivamente por um conjunto de técnicas elétricas, que incluem medidas em modo quasi-estático por exemplo, curvas corrente-tensão (*I-V*) e medidas da impedância (capacidade e resistência) no domínio da frequência. Os filmes com nanopartículas de CdS foram também caracterizados com medidas óticas e complementadas com uma caracterização morfológica.

Os díodos com base em LiF foram produzidos por evaporação nos laboratórios da Philips em Eindhoven, (Holanda). Estes díodos tem uma estrutura do tipo Al / LiF / polímero / Ba. O polímero usado é um polímero semiconductor, o espirofluoreno. Depois da fabricação os díodos foram encapsulados e enviados para Portugal. As nanopartículas de CdS foram produzidas na Universidade do Algarve pelo método da química coloidal com o uso de gelatina como estabilizador.

O estudo dos díodos de LiF incidiu principalmente no estudo do fenómeno conhecido por eletroformação. Quando fabricados os díodos de LiF não tem propriedades de memória. É necessário aplicar um campo elétrico que causa uma rutura dielétrica no dispositivo. Só depois desta rutura o díodo se comporta como uma memória resistiva. O trabalho realizado nesta tese focou-se principalmente no estudo dos processos físicos que ocorrem na interface LiF/polímero antes da rutura dielétrica ocorrer. Em particular, este estudo analisa como o campo elétrico interno devido ao armazenamento das cargas, afeta o comportamento elétrico do dispositivo.

O estudo das nanopartículas de CdS embebidas em filmes de polímeros pretendia inicialmente a construção de memórias resistivas. Esta ideia assentava no pressuposto que os filmes com nanopartículas de CdS também podiam funcionar como memórias, à semelhança de outros sistemas referidos na literatura. No entanto, os filmes poliméricos, com elevadas concentrações de nanopartículas de CdS não mostraram qualquer comutação resistiva reversível e programável por um campo elétrico. Interessante, quando submetidos a um campo elétrico externo as suas propriedades elétricas são alteradas e transforma-se em materiais isoladores. Esta propriedade pode ser usada em memórias não-voláteis que são vulgarmente designadas por memórias do tipo: "Write-once read many times" também designadas pela sigla WORM.

A transformação dos filmes com nanopartículas de CdS em PVP de um material semiconductor em um isolador elétrico foi tentativamente explicada como sendo devido a um efeito de repulsão de Coulomb causado pelas nanopartículas de CdS que ficam carregadas eletricamente o que impedia a condução elétrica no filme. Dado que o fenómeno é induzido pelo campo elétrico externo, foi também designado por eletroformação. Embora neste caso a eletroformação seja a de um material dielétrico, e não das propriedades de comutação resistiva. O fenómeno tem um tempo de vida muito longo (dias ou semanas) pelo que é de certa forma uma memória resistiva apesar de ser eventualmente volátil.

A presença de nanopartículas de CdS nas soluções foi confirmada por espectros de difração de raios-X. Os espectros de XRD mostram a assinatura da estrutura cúbica do CdS. Foi também verificado o efeito dos processos de superfície interfásica na absorção e luminescência, assim como os efeitos quânticos devido às dimensões das nanopartículas. A partir de medidas ópticas, o tamanho médio (raio) das nanopartículas foi estimado entre 2 a 11,0 nm. A luminescência dos filmes na região dos infravermelhos foi associada a defeitos na superfície das nanopartículas de CdS, nomeadamente a lacunas de enxofre.

A investigação das propriedades físicas e químicas das nanopartículas de CdS mostrou que a concentração e os valores de pH da solução influenciam diretamente o tamanho das nanopartículas. A formação de nanopartículas de diferentes tamanhos está relacionada com mudanças no equilíbrio ácido-base como resultado da hidrólise dos componentes de sais.

As nanopartículas de CdS foram incorporadas em diferentes matrizes isolantes, nomeadamente polivinilpirrolidona (PVP), gelatina, dimetilformamida (DMF), poliestireno sulfonato ($PSS_{Na}$).

**Termos chave:** Nanopartículas de CdS, díodos de LiF, memória não volátil, Resistência Diferencial Negativa (NDR), comutação resistiva, caracterização elétrica.

# CONTENTS

## INDEX OF FIGURES

## INDEX OF TABLES

## LIST OF ABBREVIATIONS

| | |
|---|---|
| **BRS** | Bipolar Resistive Switching |
| **CdS** | Cadmium Sulfide |
| **CMOS** | Complementary Metal-Oxide Semiconductor |
| **DB** | Dielectric Breakdown |
| **DC** | Direct Current |
| **DMF** | Dimethylformamide |
| **DRAM** | Dynamic Random-Access Memory |
| **E** | Electric Field |
| **Eg** | Energy Band Gap |
| **ETL** | Electron Transport Layer |
| **HRS** | High Resistance State |
| **HTL** | Hole Transport Layer |
| **IV** | Current Voltage |
| **JV** | Current density Voltage |
| **LED** | Light Emitting Diode |
| **LiF** | Lithium Fluoride |
| **LRS** | Low Resistance State |
| **MIM** | Metal Insulator Metal |
| **MIS** | Metal Insulator Semiconductor |
| **MISFET** | Metal-Insulator-Semiconductor Field-Effect Transistor |
| **MOS** | Metal–Oxide–Semiconductor |
| **MOSFET** | Metal-Oxide Semiconductor Field-Effect Transistor |
| **MRAM** | Magnetic RAM |
| **NC** | Nanocrystal |
| **NDR** | Negative Differential Resistance |
| **NP** | Nanoparticle |
| **NVM** | Non -Volatile Memory |

| | |
|---|---|
| **OLED** | Organic Light Emitting Diode |
| **PL** | Photoluminescence |
| **PVP** | Polyvinylpyrrolidone |
| **$PSS_{Na}$** | Poly (sodium styrene sulfonate) |
| **QD** | Quantum Dot |
| **RAM** | Random Access Memory |
| **RRAM** | Resistive Random-Access Memory |
| **RS** | Resistive Switching |
| **SEM** | Scanning Electron Microscope |
| **SSD** | Solid State Drives |
| **URS** | Unipolar Resistive Switching |
| **XRD** | X - Ray Diffraction |

# Chapter 1

## *General introduction to dissertation and structure*

This chapter presents the motivations, challenges, and research objectives of this thesis. It also provides an overview and a description of the thesis organization.

## 1.1. Introduction.

In this chapter, we present the scientific and technological context underpinning the research conducted in this thesis. Given that this study revolves around the characterization of two distinct materials, namely CdS nanoparticles and the halide LiF, we offer an overview of the scientific and technological significance of these materials.

In the context of diode-like structures involving semiconducting polymers, LiF plays a role as a thin insulating layer. In practical terms, the function of the LiF layer closely resembles that of thin oxide layers like $Al_2O_3$ and $TiO_2$. Consequently, the existing body of literature on memory devices utilizing thin oxide layers becomes highly pertinent in comprehending the objectives and research areas addressed in this thesis.

This chapter begins with a historical overview of the utilization of metal nanoparticles in technological applications, accompanied by an exploration of the initial physical models employed to elucidate the peculiar electrical and optical characteristics exhibited by these nanoparticles. Furthermore, it furnishes a context for understanding the significance of oxide-based memories, briefly delineating the breakthroughs in this field.

This work on the LiF based diodes for memory applications was inspired by previous studies carried out by the research group and reported in the references [1]–[7].

## 1.2. Motivations and research objectives.

At present time, the processes occurring in nanocomposite films are the subject of intensive research in connection with fundamental scientific problems and the exceptional performance properties of film materials. Although the beginning of the boom in research and the use of nanomaterials occurred within the 80s-90s years of the last century, the first mention of the physics of nanoscale systems can be found in the scientific literature much earlier. So, back in the first half of the 19th century, a message appeared on the method of preparation of metal-polymer nanocomposites. This was due to research on colloidal solutions. A polymer matrix was needed as a convenient way to fix nanoscale metal particles.

Following this pioneering research in nanocomposites outlined above, other metal-polymer nanocomposites emerged, and a characteristic feature of these novel materials was the

different colour of the prepared compounds. Many attempts were made to explain this colour of colloidal systems, and it was only in 1908 that an adequate solution of Maxwell's equations was found by Gustav Mie [8], which made it possible to relate the colour of colloidal particles to their size and to observe wave scattering by particles.

The polymer host matrix is typically providing a unique physico-mechanical characteristics of nanocompositions, such as processing properties and high flexibility. Meanwhile the structure has a high sensitivity and effective photoluminescence properties. It is possible to control the structure of the material by changing the synthesis conditions and composition, and its chemical, catalytic, and sensory properties [9]. There are two methods for producing nanocomposites. The first strategy is to inject pre-synthesized nanoparticles into the polymer matrix, and the second is to make them in situ, i.e., nanoparticles are generated in the polymerized matrix at the time of composite production, allowing for a uniform distribution of nanoparticles. To obtain in situ nanocomposites of various compositions based on cadmium sulphide nanoparticles in a polymer matrix, characterise their structure, determine the relationship between the initial concentrations of precursors and the size of the nanoparticles formed, and examine their spectral and luminescence properties, the second method was used in the current study.

Due to their unique characteristics, materials containing nanoparticles dispersed in a matrix are widely used in a variety of applications. Among the practically important properties of metal-containing nanocomposites, are the conductive, magnetic, photoelectric, sensor, dielectric, and catalytic properties. It is interesting that the same composites can demonstrate different physical and chemical properties, for example, they can turn out to be good sensors and at the same time exhibit exceptional catalytic properties. Of course, such a variety of properties opens up practically unlimited possibilities of using these nanomaterials and at the same time causes certain difficulties in their study and interpretation of the results.

The issue is that there is no developed regular mathematical apparatus for describing the properties of nanoparticles that make up these materials. On the one hand, nanoparticles are too small to fully use standard statistical methods, furthermore a sufficiently large numberof atoms and molecules of which they are composed excludes the possibility of directly usingthe methods of quantum mechanics. Therefore, each time it is necessary to make sure that the approximations used are reasonable, and sometimes to develop a special mathematical method.

If for the spectral characteristics of nanoparticles, it is possible to trace a smooth transition with a change in size from the atomic level to the macroscopic level, then several other properties of nanosystems are qualitatively different, and sometimes have nothing to do with the properties of macroscopic systems. These include catalytic, thermodynamic, kinetic and sensory properties. Moreover, this is significant, even when changes in the size of the particles that make up the nanosystem occur only within the nanoscale. We also note that, for small particles, an important role is played by a significantly larger surface fraction compared to an ordinary solid and large nanoparticle.

If the size and distance between nanoparticles are in the nanometer range, a number of possibilities arise. Thus, changing the size of nanoparticles can be controlled by the width of the energy band gap. When the concentration of the inorganic filler is close to percolation threshold, the electrical and optical the properties of hybrid semiconductor-polymer systems can change significantly with not big change in the distance between particles or with a change in their surface characteristics.

A number of examples can be cited when, depending on the size of nanoobjects, their physicochemical properties change. Thus, with a change in the size of nanoclusters, not only the radiative lifetime corresponding to the optical transition from the excited state to the ground state changes, but also their melting temperature in a very wide range.

The sensory properties of nanosystems are also highly dependent on the size of nano-objects. Moreover, the most noticeable changes occur in small particle sizes. Similar phenomena are observed when studying the properties of nano-catalysts.

Interestingly, the properties depend not only on the size of nanoobjects, but also on their shape [10]. Thus, it was possible to detect extremely high sensitivity of sensors based on porous nanotubes and nanofibers.

In addition to specially synthesized nanosystems, there are also natural nanoobjects; the size of these objects can reach hundreds of nanometers. These primarily include biological systems [11], for example, cells, in which various processes take place, and the size of nano-systems has a significant effect on the patterns of these processes.

Memory devices, particularly resistive random-access memories (RRAM), have emerged as a front-runner in numerous technological domains in recent years [12]. This is made possible by its high-speed operation, structural simplicity, low power consumption,

adaptability potential, and memory storage properties with high density. To create an efficient and miniaturised memory device based on the resistive switching effect, researchers must investigate a variety of materials and production approaches.

Along with the solution of purely scientific problems, much attention is currently paid to the development and use of nanotechnology. Thus, the magnetic properties of nanocomposites play a key role in the development of information technologies in connection with the possibilities of increasing the density of magnetic recording of information and the effect of giant magnetoresistance, which is used in read heads and non-volatile memory elements. There are exists a number of examples of the effective use of nanotechnology - creation and industrial production:

a) laser diodes designed for the visible and near infrared spectral region;

b) ultrafast field-effect transistors;

c) avalanche photodiodes for fiber-optic communication lines, etc.

Due to the use of nanotechnology in the formation of ultrathin layers that made it possible to realize in these devices parameters that were fundamentally unattainable by traditional methods. Currently, the main methods for growing films of semiconductor compounds with a thickness of several nanometers are colloidal chemistry molecular beam epitaxy, and vapor deposition of organometallic compounds [13]–[16].

Although the processes and phenomena discussed above belong to different areas of physics, chemistry and biology, they have something in common; the size of the objects in which these processes take place. This dissertation is devoted to the discussion of the regularities of various phenomena in nanoscale systems.

The main goal of this thesis work is to develop and characterize different resistive switching devices, to perform techniques for fabrication nanoparticle-based electronic devices and find out universal experimental methods to investigate electrical and physicochemical behaviour of obtained samples. Also, along with studying of semiconductor colloidal nanocrystals of cadmium sulfide, we are going to compare their electrical behaviour with LiF diodes and reveal the unique electroforming and resistive switching characteristics.

### 1.2.1. Review on semiconductor nanocrystals and their practical use.

Semiconductor nanocrystals are particles with sizes ranging from units to tens of nanometers. Researchers claim that the main difference between nanocrystals and macroscopic crystalline semiconductors is the unique appearance of the size quantization effect, which makes it possible to set the effective band gap of nanoparticles by using nanoparticles of a particular size [17]–[19]. Such objects possess narrow-band luminescence, the spectral position of which is determined by the size of nanoparticles and does not require changing the material from which they are made.

Due to their unique electronic and optical properties, nanocrystals have great potential for creating new optical devices - light sources with specified characteristics, in particular, lasers, organic light-emitting diodes, as well as photodetectors, solar cells, luminescent biomarkers, etc.

The production of nanocrystals by epitaxial methods requires expensive equipment and high qualifications of service personnel [20]–[22]. Therefore, devices made by this method are expensive. In addition, the production process is associated with the use of exclusively poisonous gas carriers and requires additional measures to ensure the safety of work on the equipment used.

Relatively recently appeared colloidal synthesis method of the semiconductor nanoparticles, wherein the nanocrystal growth occurs in solution. This method is extremely cheap, since no expensive equipment is required for the synthesis of nanoparticles, and the precursors used are available and much less hazardous. This production method turns out to be scalable and allows one to obtain nanoparticles with specified characteristics on an industrial scale. Modern methods of synthesis make it possible to obtain a solution of nanocrystals with a size spread of no more than 7%. Great progress has been made in the synthesis of cadmium chalcogenides (CdSe, CdS, CdTe). Colloidal solutions of nanocrystals can be deposited on the substrate using spin-coating techniques, inkjet printing, and techniques continuous applying material (roll-to-roll casting). These technologies can significantly reduce the cost and expand the production of devices based on the use of such nanomaterials and have a significant competitive advantage in relation to vacuum technologies currently used for the production of semiconductor partitions.

Application of the colloidal synthetic methods require the use of the special measures to prevent aggregation of several nanocrystals and providing colloidal stability of solutions -

surface coating with organic ligands. Usually, nanocrystals of cadmium chalcogenides are coated with oleic acid molecules, which provide colloidal solubility in most non-polar organic solvents.

Since the ratio of the number of surface atoms to the number of atoms in the bulk of nanoparticles increases with decreasing size, surface states have a significant effect on the optical characteristics of nanocrystals [23]. Their main manifestation is the formation of nonradiative relaxation channels due to dangling bonds. Coating (passivating) the surface with organic ligands allows saturating the dangling bonds at some surface atoms and increasing the luminescence quantum yield. Topics not less, even in the passivated nanoparticles quantum yield is significantly limited. This is due to the impossibility of saturating the dangling bonds of all surface atoms. Therefore, in devices where nanocrystals are embedded in functional matrices, surface states can have a significant effect on the interaction of nanocrystals and the matrix. The local environment of nanocrystals can be molecules of liquids and gases sobbed on the surface. In this case, the specific interaction of such molecules with surface states can lead to the appearance of new optical properties that arise selectively for certain types of compounds. This opens up possibilities for creating detectors of gases, vapours of liquids with low concentrations, and various sensors.

Surface states can also lead to the appearance of emitting centers and to a significant change in the structure of the luminescence spectra of nanoparticles. This feature may be in demand when creating new light sources with specified spectral characteristics. For this essential information about the nature of the surface states, as well as on ways to control their properties, we were investigating the optical properties of CdS nanoparticles.

Despite the large number of works devoted to the study of semiconductor nanocrystals, information on their surface states turns out to be very limited. In this case, surface states have unique properties, which are determined not only by the material, but also by the size and shape of nanoparticles, as well as a passivator. In view of the complex structure of the surface of nanocrystals, it is difficult to predict theoretically the properties of such states. The lack of proven techniques for characterizing surface states in nanocrystals does not allow one to reliably establish their properties, find ways to control them, and designate their application areas. Therefore, the development of methods for studying surface states is an urgent task.

When used as matrices to create CdS nanoparticles and CdS/polymer nanocomposites, polymers have a number of benefits [24]. Contrarily, nanoparticles in solution with

homogeneous confinement and a narrow size distribution can be created using polymers with a certain spatial morphology as precursors. In addition, polymers, which are well known for their ability in effectively regulating particle size and size distribution, are able to perform surface passivation, avoid nanoparticles from agglomerating, as well as regulate the degree of dispersion of NPs.

The size of particles and their properties are greatly influenced not only by the method of synthesis, but also by the conditions of its flow. Therefore, it is necessary to carefully select and control the synthesis conditions, such as starting reagents, reagent concentrations, temperature, etc.

### 1.2.2. State of the art about electroforming process

Oxide based memories require an electroforming process to become programmable memories. Electroforming is a dielectric soft-breakdown mechanism leading to non–volatile memory behaviour [4]. Typically, electron trapping occurs at the early stages of electroforming. An electric field is created across the oxide by the trapped charges. Soft breakdown takes place when the internal field approaches a critical value, leading to an active memory diode. By applying a voltage between the electrodes, the conductivity of the oxide is altered, enabling data to be stored in a non-volatile manner [25]. The process can then be reversed, and the data erased by applying a voltage of the opposite polarity to the memory cell.

The mechanism of electroforming is common to all oxide-based memories, but it has not yet been fully elucidated. It is commonly accepted that the electroforming process determines the main properties of the switching properties, namely the on-off ratio, the retention time, and endurance. Despite this important role, electroforming has not been proper addressed in the literature. The main reason for this lack of understanding relies on the experimental difficulties in detecting the charges that become trapped at the oxide/polymer interface. This charge build-up and their temporal dynamics is not trivial to observe.

The definition of word “forming”, or the now more commonly utilize as “electroforming”, became used to describe the process by which the insulating material’s conductivity is altered when a voltage above a certain threshold voltage is applied [25]. Initially, the insulating materials investigated were inorganic insulators such as $Al_3O_2$ (Hickmott 1962, 1965; Barriac 1969), SiO (Simmons & Verderber 1967), ZnS (Sutherland

1971) and TiO (Ansari & Qadeer 1985) [26]–[29]; however, organic and polymeric insulators were soon investigated and also found to exhibit similar electroforming behaviour (Hogarth & Zor 1975; Hogarth & Iqbal 1979) [30].

However, there was still a lot of uncertainty over the mechanisms that were responsible, with theories such as:

a) metal ion injection from the electrodes, leading to impurity bands in the insulator;

b) conducting filamentary pathways forming owing to electrolytic processes;

c) formation of filaments from the metallic electrodes, carbonaceous material from the insulator itself or from sources introduced during manufacture of the devices;

d) tunnelling between metal islands produced during the electroforming process.

Most papers published that attempt to explain the phenomena observed inelectroformed metal–insulator–metal (MIM) claim that filamentary formation occurs in the insulating material, forming a low conductance pathway between the electrodes (Dearnaley etal. 1970; Sutherland 1971; Hogarth & Iqbal 1979; Ray & Hogarth 1984, 1990; Biederman et al. 1989; Pagnia 1990). Significant efforts have been done to image filaments using various microscopy techniques such as scanning electron microscopy, transmission electron microscopy (Pagnia et al. 1987) and scanning tunnelling microscopy (Pagnia 1990; Brauer et al. 1994), there are several evidence for their existence. Recently Hickmott published a work about electron emission and ultraviolet electroluminescence from valence-band states and defect conduction bands of electroformed Al-$Al_2O_3$-Ag diodes [31] and about millimeter distance effects of surface plasmon polaritons in electroformed Al-$Al_2O_3$-Ag diodes [32]. Also, the important discoveries were described in his work about electroforming and Ohmic contacts in such type of diodes [33].

For the high conductivity semiconductor materials, sometimes it is not possible to distinguish between the onset of these two processes (switching and electroforming), and it is highly probable that the two processes are initiated simultaneously. Electroforming is normally observed in insulating materials (following Ray and Hogarth 1984), where there is a very rapid increase in the current drawn at a particular moment. Afterwards samples showed the typical electroforming characteristic of voltage-controlled differential negative resistance (VCNR) for increasing and decreasing voltages. The basic characteristics observed for both these phenomena are discussed in the paper from reference [34].

Dearnaley [35] presented a theory of the oxide-coated cathode, which model is presented in order to explain a variety of previous observations on the oxide-coated thermionic

cathode, as well as the behaviour of a number of other oxide layer structures. For the filament growth and switching in amorphous oxide films was shown a model at ref. [36]. Following the theory, the conducting filaments with molecular dimensions form through the oxide covering during the activation process. Such a mechanism is responsible for the electrical conductivity ofthe oxide and its high thermionic emission efficiency.

Such conducting filaments may have a structure that resembles a chain of metal atoms divided by oxygen vacancies, most likely clustered along oxide grain boundaries. The relationship between the old and current ideas of oxide-coated cathode behaviour has been investigated. Several experimental techniques were done on electroforming of Metal-Oxide-Metal thin film sandwiches. Samples have been electroformed and they exhibit negative resistance by controlling the voltage.

The evidence in favor of localized or filamentary conduction is given at work of D. Oxley [37]. In 1971, R. R Sutherland presented a theory for negative resistance and memory effects in thin insulating films and its application to Au-ZnS-Au devices [29]. The main point of his model was based on the bias induced formation and thermal rupture of conducting filaments. Professor C. A. Hogarth and T.Iqbal (at Brunel University) reported the electroforming of thin films of polypropylene. It was shown that on exceeding a threshold applied voltage, thin films of evaporated polypropylene in the form of a sandwich between metal electrodes (aluminium or copper) undergo an electroforming process. The results are consistent with a theory based on the generation of conducting filaments during the forming process.

A. J. Kenyon, M. Singh, M. Buckwell, et.al [38] carried out a study of the relationship between oxide microstructure at the scale of tens of nanometers and resistance switching behaviour in silicon oxide. By offering an initial structured distribution of defects that can serve as precursors for the formation of chains of conductive oxygen vacancies when the proper electrical bias is applied, columnar structure in the case of sputtered amorphous oxides enables effective resistance switching. Increasing the roughness of the electrode interface reduces electroforming voltages and the distribution of switching voltages [39]. Field enhancement at rough interfaces contributes to these phenomena owing to alterations in oxide microstructure templated by interface structure.

Different characteristic electroforming behaviour in $Pt/TiO_2/Pt$ resistive switching cells depending on atmosphere were investigated in reference [40]. Authors performed

electroforming effects on the composition, electrical resistance of switching cells and their structure. Also have been discussed the correlation between the electroforming procedure and the resulting bipolar switching behaviour. Electroforming behaviour depends on atmosphere, it is possible to define symmetric or asymmetric electroforming, and a resulting bipolar switching characteristic. From the experimental results authors suggest a possible mechanism for electroforming in $Pt/TiO_2/Pt$ in terms of the formation of oxygen gas and vacancies in the vicinity of the anode.

The main aim of our investigation is to find out the physical mechanism that led to electroforming and resistive switching in LiF diodes and CdS-based structures. To achieve this goal, we used small-signal impedance methods. In the next chapters we will show the most relevant measurements, described the electrical behaviour of electronic devices based on CdS NPs in different host matrices and Al/LiF/polymer/Ba-Al diodes during their pristine, on- and off-states, as well as frequency dependence of the capacitance and resistance, and electrical noise measurements. Also, will be discussed electroforming process and analysed the negative differential resistance (NDR) of the memory device.

More detailed information and current understanding about electroforming of resistive switching devices will be presented in the Chapter 2 and in Chapter 4.

## 1.3. Structure of dissertation

In Chapter 2 is given a detailed review and analysis of the literature on the topic of the thesis. Understanding the early stage of electroforming may allow us to optimize the electroforming procedure and fabricate resistive switching devices with better characteristics. Furthermore, the role of the polymer layer in controlling the electronic mechanism is explained.

Chapter 3 provides experimental details of the sample fabrication and characterization techniques that were used in the thesis. The optical techniques to characterize nanoparticles and nanocrystals, their concepts, and methods are presented. Morphological and optical characterization techniques, based on spectroscopic analysis (UV-Visible Spectroscopy), Photoluminescence (PL), Scanning electron microscopy (SEM), X-ray diffraction and Raman spectroscopy are also discussed. The detailed process of fabrication and encapsulation of resistive switching diodes based on LiF and CdS nanoparticles were also presented in this chapter. Finally, the electrical characterization techniques and the schematic diagrams of the device's structure based on CdS NPs and LiF resistive switching device are presented.

In Chapter 4 is the electroforming and resistive switching on LiF diodes is presented and discussed. The diode devices of an Al/LiF/polymer/Ba-Al diodes were turned into programmable resistive switching memories by applying a voltage above a critical value. Here we study in detail the electronic process occurring prior to electroforming of the memory device. Accumulated charge at the interface LiF/polymer creates an internal electric field that eventually causes the rupture of the dielectric properties. Understanding the early stage of electroforming may allow us to optimize the electroforming procedure and fabricate resistive switching diodes with better memory characteristics. Furthermore, the role of the polymer layer in controlling the soft breakdown mechanism may be better understood. A model to explain the resistive switching behaviour and relevant effects are proposed in this chapter.

Chapter 5 performs the synthesis details of CdS nanocrystals that are placed in a dielectric matrix of photographic gelatin. The use of such particles is very promising in various fields, from biology and medicine to photoelectronic devices, optical switches, sensors, electroluminescent devices, lasers, etc. For all these applications, it is important to know the specifics of the interaction of nanoparticles with a radius in placed host matrix. CdS nanocrystals in the gelatin matrix with different pH values and their optical properties were investigated and discussed the influence of this value on the optical absorption and luminescence, and its direct influence on the size of nanoparticles.

Chapter 6 is devoted to the influence of the structure of nanoparticles on their physicochemical properties. It presents the results of an experimental study by modern analytical methods of CdS nanoparticles in various polymer host matrices. The structure and optical properties of these nanoparticles and the composition of their surfaces were determined. This chapter also provides a comparison between the physical and chemical properties of the nanoparticles, deposited by various methods on the substrate of different nature. Parameters such as the radius and the optical band gap were obtained.

Chapter 7 is devoted to research on hybrid nanomaterials based on polymers and semiconductor nanoparticles. It is taken into account that the electrical, optical, and structural properties of the nanocomposite substantially depend on the particle size. To preserve these unique properties of the nanocomposite, it is necessary to provide a controlled distribution of nanoparticles in the polymer matrix, which is a nontrivial task due to the strong tendency of nanoparticles to aggregate. One of the promising methods for the formation of thin-film hybrid nanocomposites with a high degree of filling is the surface polymerization process and a sol-gel technology. The influence of formation and conditions of drying on the crystal structure

and morphology of thin film nanocomposite, as well as their relationship to the structure of the optical properties were discussed.

Investigation of optical and morphological properties of the CdS nanoparticles in different host matrices and electroforming of nanodielectrics based on NPs are presented in Chapter 7. There is an analysis of the results of a comprehensive structural study (data obtained by XRD, SEM and Raman measures were used) with different average nanoparticles sizes in the range of 2-11 nm. The optical and electrical properties of these materials and possible reasons for the revealed size effects are also discussed. Electroforming of nanodielectrics based on CdS nanoparticles in different host matrices is presented by the end of current chapter. Particularly, sandwich structures (Au/CdS (PVP)/Au) fabricated using CdS free standing films, planar structures (Au/CdS (PVP)/Au cast in glass substrates and planar structures using gelatin (Au/CdS (gelatin)/Au) were electrically characterized. Also, electrical properties of $n^{++}$Si/CdS-PVP/Ag heterojunction structures sandwich structures and planar devices using polystyrene sulfonate sodium salt/CdS ($PSS_{Na}$)/Au were investigated. Finally, in Chapter 8 the overall conclusions concerning the electrical characterization of resistive switching devices are presented and critically analysed together with the suggestions to the future work.

# Chapter 2

## *Foundations of Resistive Switching and Devices Based on CdS Nanoparticles*

This chapter reviews the current developments in resistive switching devices. It presents the major unsolved challenges and leads to the motivation of this thesis. The description of the resistive switching phenomena, their classification, the physical models to explain the physics of the switching mechanism, the materials used, including bulk materials and composites with nanoparticles; the limitation that prevented until now the commercialization of resistive switching memories is also explained here. The chapter also conducts a thorough review of materials properties pertaining to CdS nanoparticles, with a specific focus on their optical and electrical characteristics that are shaped by their nano-scale dimensions.

## 2.1 Introduction

The rapid advancement of micro- and nanoelectronics has been a driving force behind the exponential growth of modern information technologies. These technologies necessitate the creation of memory solutions with substantial capacity and rapid data read-write capabilities. The demand for non-volatile memories with extensive storage capacity has surged, alongside the need for smaller devices capable of storing ever-increasing volumes of data to support our information-rich society. Portable hard disks, Solid State Drives (SSD), and flash memory devices are representative examples of commercial memory devices. These memory devices allow data to be retained without continuous application of power, meaning that they are “non-volatile”. The market of non-volatile memory is a business worth billions of dollars, and it is expected to keep growing in the future [41], [42]. In this regard, the largest companies producing electronic component bases (IBM, Samsung, Intel, Sharp, Hewlett Packard, SONY, Panasonic, etc.) are actively developing fundamentally new elements of non-volatile memory with high working characteristics and scalability.

This thesis centers around the investigation of resistive switching phenomena as a foundation for developing memory devices. Resistive switching involves an alteration in the electrical resistance induced by applying a voltage. It is important to note that resistive switching is a non-volatile process, meaning that the changes in resistance persist even without an applied voltage, and it is entirely reversible.

A fundamental distinction exists between memory systems based on resistive switching and most contemporary semiconductor memory technologies. Unlike conventional methods that store information in the form of an electric charge, resistive switching operates by alteringthe electrical resistance of a material. This unique characteristic eliminates the concern of charge leakage. In simple terms, data can be retained within a resistive switching device for aslong as the constituent materials endure. To put this into perspective, flash memory begins to lose recorded information within a year of storage without access to an electrical current. A computer with resistive switching type of memories will consume ten times less electricity, but also can operate without reboots - when turning off /on, always remembering and returningits last working state.

This chapter reviews the basic concepts behind resistive switching phenomena necessary to understand the experimental work carried out in this thesis.

In spite of the advantages of the resistive switching phenomena to make non-volatile memories, a number of technological difficulties has prevented until now the commercialization of memories based on resistive switching. Because of this, the research in resistive switching has evolved and focused in exploiting the resistive phenomena in neuromorphic devices.

In contrast to conventional memory devices, neuromorphic devices are engineered to have a multitude of conducting states. These electrical states are so finely graded that the shift in resistance appears more akin to a continuous spectrum rather than distinct, well-separated conduction states. When a series of consecutive voltage pulses is applied, corresponding changes in electrical resistance occur, emulating the behaviour of neural synapses. Consequently, neuromorphic devices have the capacity to replicate the functionalities of synapses and neurons. This chapter also provides an overview of the latest advancements in this field.

Finally, this thesis also explores thin films of CdS nanoparticles for memory applications, the fundamental concepts about nanoparticles are also briefly review in this chapter.

## 2.2 Resistive switching

The resistive switching (RS) phenomenon consists of the change of resistance when a voltage pulse is applied. It was first reported by Hickmott in 1962 [26]. Within resistive switching memory cells, such as those in Resistive Random-Access Memory (RRAM), a common configuration comprises a capacitor-like MIM structure, composed of an insulating or resistive material 'I' sandwiched between two (possibly different) metals 'M'. In the context of this review, the material 'I' are oxides, halides, or higher chalcogenides which typically show some ion conductivity [43].

Resistive switching can be classified into two distinct categories based on their control mechanism: unipolar or bipolar [44], [45]. In unipolar switching, both $V_{\mathrm{Set}}$ and $V_{reset}$ voltages share the same polarity. The memory changes from a high resistance state (HRS) to a low resistance state (LRS) at a particular voltage, $V_{\mathrm{Set}}$, and returns to the HRS at $V_{Reset}$. Figure 1 shows a schematic diagram depicting a resistive switching of a unipolar type. The *I-V* curves of both LRS and HRS are symmetric, and the type of electrode is relatively unimportant. Some

authors [46] claim that the direction of the switch is dictated by the magnitude of the applied bias rather than its polarity. Memory devices studied in this thesis are of unipolar type, however unlike the behaviour depicted in Fig. 2.1, $V_{Set}$ occurs at lower voltage than $V_{Reset}$.

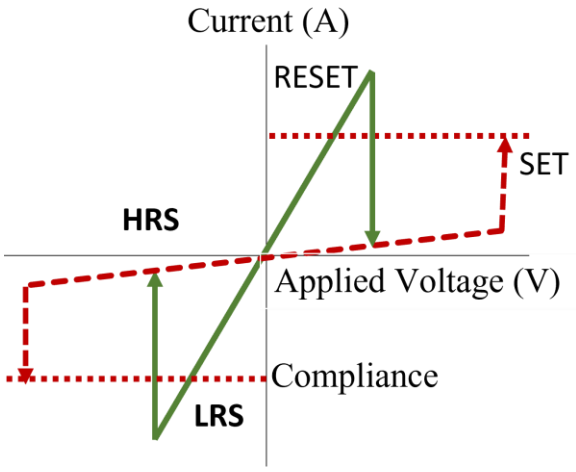


**Figure 2.1**. Typical *I-V* characteristics of unipolar resistive switching type.

According to some studies, the type of electrode used does not affect the switching in unipolar switching [47]. Unipolar resistive switching, is mostly observed in transition metal oxide [48]–[50], $TiO_2$ [51], $Al_2O_3$ [52], NiO [53], SiO, $Nb_2O_5$ [54], $YCrO_3$ [55], LMO [56], CoOx [57].

Unipolar resistive switching requires a "forming process". The forming process is a procedure in which a high voltage bias is applied to the sample, during which the resistance suddenly decreases. The process is similar to the soft-breakdown of dielectric materials [58]. The electroforming will be discussed later on this chapter.

Resistive switching is categorized as bipolar or antisymmetric when the $V_{Set}$ occurs at one voltage polarity, while the $V_{Reset}$ occurs at the reversed polarity. The *I-V* curves are asymmetric and depend on the type of electrode [46]. A typical *I-V* characteristic of the bipolar resistive switching effect is shown in Figure 2.2. A good example of bipolar type of switching was reported for $La_{0.7}Zn_{0.3}MnO_3$ prepared by the sol-gel method [59], and for amorphous Sr-doped $LaMnO_3$ thin films [60]. Resistive memories based on this material exhibit a high $R_{HRS}/R_{LRS}$ ratio ($>10^4$), stable write/erase endurance ($>10^2$), and long retention ($>10^4$ s at room temperature).

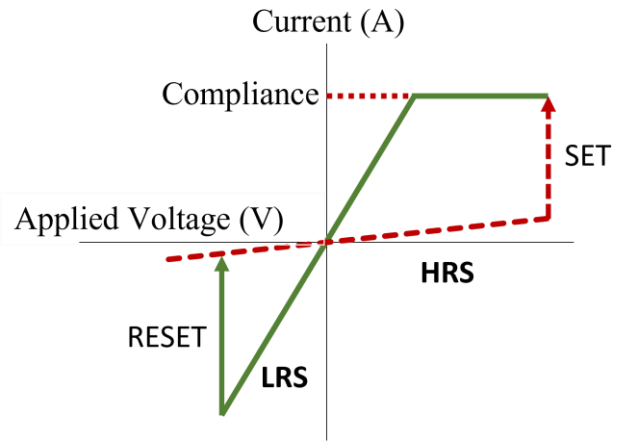


**Figure 2.2**. Typical *I-V* characteristic of bipolar type of switching

The coexistence of both bipolar and unipolar resistive switching behaviour is possible, as it has been was reported for Ag/$ZnMn_2O_4$/$p^+$-Si device [61].

Taking in account of its single polarity operation, an unipolar memory is more promising since it enables enormous scale bridge logic-in-memory circuits with the greatest integration density and easier external control circuits [62], [63]. However, due to the random activation of conducting filaments, unipolar memory typically exhibits poor switching uniformity and hence cannot meet the rigorous uniformity requirement for logic-in-memory applications [64].

## 2.3 Limitations of Resistive Random Access Memory (RRAM) devices

Although resistive switching devices based on a MIM structure can exhibit excellent performance their commercialization has been prevented by a major limitation known as crosstalk. This limitation is because all RRAM have symmetrical *I-V* curves. This symmetry is a major handicap because memory cells are organized in a matrix [65]. Individual memory elements are organized into square arrays with several cells divided into rows (words) and columns (bits) as shown in Fig. 2.3. A reading voltage is simultaneously applied to all the device in the reading line. Therefore, this voltage can read the information in memory cell but, simultaneously can also program (or erase) the nearby cell. For this reason, each cell must have a second element that controls how the cell is addressed by the bias. The component can be a

transistor or a rectifying diode or other non-linear element. The introduction of a diode or a transistor element in the cell significantly reduces crosstalk.

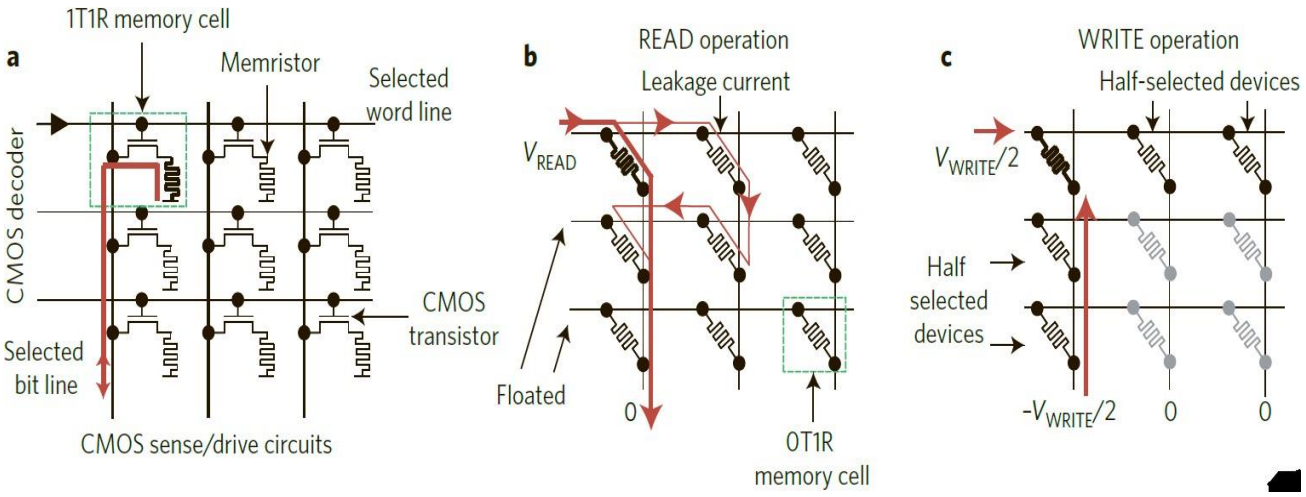


**Figure 2.3.** Organization of resistive switching memories (memristor) in cross bar arrays. A transistor is required to sect each individual memory on the array.

## 2.4. Terminology and requirements of memory-based devices

The scientific community in the memory field uses a complex terminology. These terms are used to classify the type of memory but also the benchmark their basic performance against competing technologies. Below, we summarize the basic terminology used in the field as well as some of the requirements to fulfil if the technology intends to replace commercially available technology.

**Operating voltage**. Operating voltage is voltage used to program or to erase the memory. The common rule state that a high operating voltage is a fatal flaw in practical application. That happens because a high operating voltage means high power consumption. Also, reliability can be a problem with a high operating voltage. If RRAM devices are to be competitive with commercially available Flash memories, programming and erasing voltages should be reduced to a few volts. [66]

**Write operation.** In order to be compatible with CMOS technology, write voltage ($V_{wr}$) should be below 1 V. To compete with DRAM specifications and to outperform current available Flash memories, which have a programming speed below 10 ms, the RRAM must have a write

voltage pulses duration ($t_{wr}$) below 100 ns which has a programming speed of some 10 ms, or even <10 ns to approach high-performance SRAM.[65] The length of the write voltage pulses ($t_{wr}$) should be <100 ns.

**Read voltage**. Read voltages ($V_{rd}$) need to be significantly smaller than write voltages ($V_{wr}$) in order to prevent a change of the resistance during the read operation. Because of constraints by circuit design, $V_{rd}$ cannot be less than approximately one tenth of $V_{wr}$. An additional requirement originates from the minimum read current ($I_{rd}$). In the ON-state, $I_{rd}$ should not be less than approximately 1mA to allow for a fast detection of the state by reasonably small sense amplifiers. The read time ($t_{rd}$) must be in the order of $t_{wr}$ or preferably shorter.

**On-off ratio.** The on-off ratio, the ratio between the high resistance state (HRS) and the low resistance state (LRS). The on-off ratio plays an important role in RRAM applications because it directly influences the accuracy of programming and erasing. Although an $R_{HRS}/R_{LRS}$ ratio of only 1.2 to 1.3 can be utilized by dedicated circuit design as often used in magnetoresistive Random-Access Memory (MRAM), $R_{HRS}/R_{LRS}$ ratios >10 is required to allow for small and highly efficient sense amplifiers and, hence, RRAM devices are cost competitive with Flash.

**Endurance**. Endurance is the number of programming cycles that a memory can undergo without failure. Contemporary Flash memory shows a maximum number of write cycles between $10^3$ and $10^7$. RRAM should provide at least similar endurance, preferably a better one.

**Retention time.** Retention time, the length of time a memory cell will stay in one state after programming, indicates the intrinsic ability of a memory cell to retain its content. A data retention time ($t_{ret}$) higher than10 years is required for universal non-volatile memory. This retention time must be kept at thermal stress up to 85 ºC and small electrical stress such as a constant stream of *Vrd* pulses. The combination of requirements on the write operation, the read operation, and the behaviour sets a voltage-time dilemma which is not addressed in most of the papers published on resistive switching so far. A ratio $V_{wr}/V_{rd}$ of ten at most needs to lead to an acceleration of the switching kinetics of $t_{ret}/t_{wr}$, i.e., approx. $10^{16}$!

## 2.5. Electroforming

Electroforming is a process that causes an irreversible or a long-lasting changes in the electrical properties of the materials. In this thesis two distinct types of electroforming are studied. The first type of electroforming is responsible for memory behaviour on LiF based

diodes (see Chapter 4) it is a phenomenon commonly observed in memories based on transition metal oxides as well. The second type of electroforming is observed in thin films of CdS nanoparticles embedded into a polymer matrix as detailed in Chapter 7. It is important to note that the nature of these two electroforming processes differs significantly between the two device structures. In LiF diodes, electroforming manifests as a soft-breakdown dielectric mechanism, ultimately giving rise to non-volatile memory[4]. Before electroforming occurs, the device behaves as an insulating material without memory characteristics. During electroforming electrical bistable defects are created. The occupancy of these defects modifies the carrier injection across the device leading to memory behaviour.

Chapter 4 of this thesis is entirely dedicated to unravelling the electronic processes taking place at the polymer/LiF interface before electroforming occurs. Gaining a comprehensive understanding of this process is of paramount importance as it serves as the foundation for optimizing and ensuring the reliability and reproducibility of the electroforming process.

It is worth noting that electroforming has posed a significant challenge in the context of resistive switching memories. This is because electroforming plays a crucial role in determining the final memory properties of these devices. However, electroforming is not yet a fully reproducible process, and the associated variability does not align with the stringent requirements of the industry.

Similar to the electroforming phenomenon observed in oxide-based memories, electroforming in CdS-based thin films also exhibits a significant initial trapping current. However, as detailed in Chapter 7, it is noteworthy that the electroforming in CdS-based thin films diverges from the conventional bistable and electrically programmable defect creation process. Instead, this electroforming process transforms the samples into insulators with robust dielectric strength. This electroforming may be exploited in write one read many times (WORM) type of memory. To our knowledge, the electroforming of a dielectric material induced by trapping current has not been documented in the existing literature.

## 2.6. Memristors

Resistance switching memory cells can be considered "memristors" (resistance with a memory effect) which have been predicted in 1971 by Leon Chua as the fourth basic circuit element because of the conceptional symmetry with the resistor, inductor, and capacitor, later extended

to memristive devices [67]. Leon Chua notice that there is no passive element that connects the magnetic flux and charge. Like passive resistance, this element (memristor) links current and voltage, however, the resistance value of this element after power off depends on the total time dependence of the signal (current) that has passed through it. In other words, the state of the element after the power is turned off depends on the evolution of its previous states, i.e. element has a memory effect.

These three passive elements - a resistor, a capacitor and an inductor - are considered basic in electrical engineering, since an electrical circuit of any complexity can theoretically be reduced to an equivalent circuit built solely from resistances, capacitances and inductances. At the same time, one position - correlating charge and magnetic flux - remained in a beautiful symmetrical picture unoccupied by anything (Figure 2.4). Therefore, Chua in 1971, based on considerations of mathematical aesthetics, offered his “memristor” to the vacant position. A memristor is a passive element in microelectronics that can change its resistance depending on the charge flowing through it (current integral during operation).

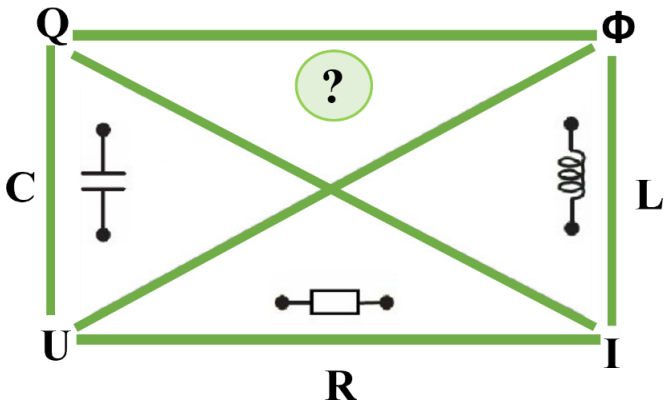


**Figure 2.4.** Illustrative image of Chua's theoretical assumption about the passive elements of an electrical circuit.

Chua's original idea in the 1970s did not find any practical application and was perceived as a mathematical fantasy, nothing more. But in the late 1990s, the Quantum Information Systems Laboratory was created at the HP Labs research center to not only keep up with the industry, which is steadily reducing microchip elements, but also to have an idea in advance how all this will work when, in 15-20 years, the basic components of electronic circuits will be

reduced to sizes on the order of a few molecules. Scientists intelligently began to create an innovative memory device based on the phenomenon - as a specific type of resistive RAM memory. More precisely, such a memory that works faster than ordinary RAM, but at the same time, when the power is turned off, it remembers its state.

## 2.7. Resistive switching phenomena for artificial synapses and neuromorphic computing

Classical resistive switching devices often exhibit a multitude of switching levels, although this may be appealing for multilevel memories, in practical terms this was not considered a desirable characteristic for two-level (on/off) or a digital type memory. However, in recent years, number of devices has been engineered and optimized to take advantage of this multitude of conductive states. The reason for that is that neuronal synapses have a similar behaviour. The more they are excited, more conductive become, a phenomenon is termed “potentiation”. In Neuroscience, long term potentiation is a persistent strengthening of synapses based on frequent patterns of activity. Due to the ability to continuously change the conductivity depending on the applied electrical signal, the novel engineered resistive switching devices are now being considered as the element base of a new generation non-von Neumann computers with multilevel logic [68], as well as electronic synaptic devices and neuromorphic computers [69]. Alongside with this experimental work also theoretical works have been devoted to designing systems of programmable logic elements based on memristors [70]. Memristor devices inspired by biosynapses, have received a lot of interest as a crucial step towards high-performance artificial neuromorphic computation [71]. The use of memristors as synapses of neuromorphic systems [72] promises to increase the computational efficiency of non-von Neumann computers [73], [74], [75].

## 2.8. Physical models to explain the resistive switching phenomena

The physics behind the resistive switching (RS) phenomena is diverse, as discussed in various studies [3], [24], [76], [77]. In essence, two distinct models have been advanced to explain the resistive switching phenomena. One model is based on the field assisted migration of atoms across the entire device. The other model is based on the creation defects that locally change the barrier for carrier injection. This modification of the carrier injection creates a high

conducting path a across the device behaving like a filament. These defects are often attributed to the presence of oxygen vacancies. Although, this local path for the electrical conduction behaves as a filament it fundamentally differs from a metallic filament that results from the migration of metallic species across the entire sample.

Resistive switching in transition metal oxide has been explained in terms of the diffusion oxygen vacancies as extensively discussed in previous research [78]. In resistive switching memory devices, the formation of conductive filaments is a key element. A filamentary (thermochemical) model has been proposed as the underlying mechanism for this switching phenomenon, with the primary cause being attributed to the electromigration of oxygen vacancies [55]. A compelling illustration of this model is the design of multistate memristors as synaptic connections for brain-inspired computing by changing the oxygen vacancy profile of tin oxide switching elements [79].

The mechanisms governing the formation and disruption of conductive filaments can be categorized into two primary divisions: the thermochemical effect and the electrochemical effect, as detailed in reference [66]. According to the thermochemical effect, Joule heating is responsible for both the production and rupture of conductive filaments [51].

Filamentary resistive switching is accompanied by the formation of conductive channels referred to as filaments, within the dielectric layer. Typically, these filaments consistof defects in the crystal lattice of the dielectric, which may include metal ions or oxygen vacancies. The formation of filaments is characterized by an abrupt decrease in resistance and, accordingly, an increase in the strength of the current flowing through the dielectric layer. Remarkably, these filaments can be so thin that they consist of only a few atoms atom in their narrowest cross-sectional dimension. Such ultra-thin filaments can exhibit quantum behavior.

Our research group has also proposed a model to explain the electrical bistability observed in oxide/polymer interface [80]. This model relies on the phase coexistence of two thermodynamically stable phases. The two phases occur in the two-dimensional double layer consisting of trapped electrons in the organic semiconductor and holes trapped at defects in the metal oxide. A schematic representation of this model is depicted in Fig. 2.5. One phase contains mostly ionised defects has a low work function, whereas the second phase, which contains mostly neutral defects, has a high work function [80]. Current filaments are created by the phase domains with a low work function. These charged domains basically behave as electrical double-layers near metal electrode [81].

It is worth highlighting the occurrence of phase coexistence in many physical systems, a notable example are ferromagnets. The phase coexistence depends on temperature. At criticallyhigh temperatures, the phenomenon of phase coexistence dissipates, causing the domains to cease to exist. Interestingly, this delicate balance between phases can be actively manipulated by external physical factors, such as the application of a magnetic field in the case of ferromagnets.

In our model, image charges in the metal should be taken into consideration when investigating the electrostatic potential energy of arrangements of trapped charges. Charge configurations forming quartets of charges have the lowest energy. These extended defects are schematically represented in Figure 2.5. The quasi-particle consists of a trapped electron in the organic semiconductor, an ionized defect in the metal oxide, and their two image charges in the metal. This assembly of condensed charges effectively forms a bilayer, comprising positive defects within the oxide and negatively charged trapped electrons within the organic semiconductor. In electroformed metal oxide organic semiconductor interfaces, charges accumulate around the oxide/organic semiconductor interface. The off-state is made up of arrays of mostly neutral defects with a high work function. The on-state is made up of arrays of mostly ionised defects with a low work function.

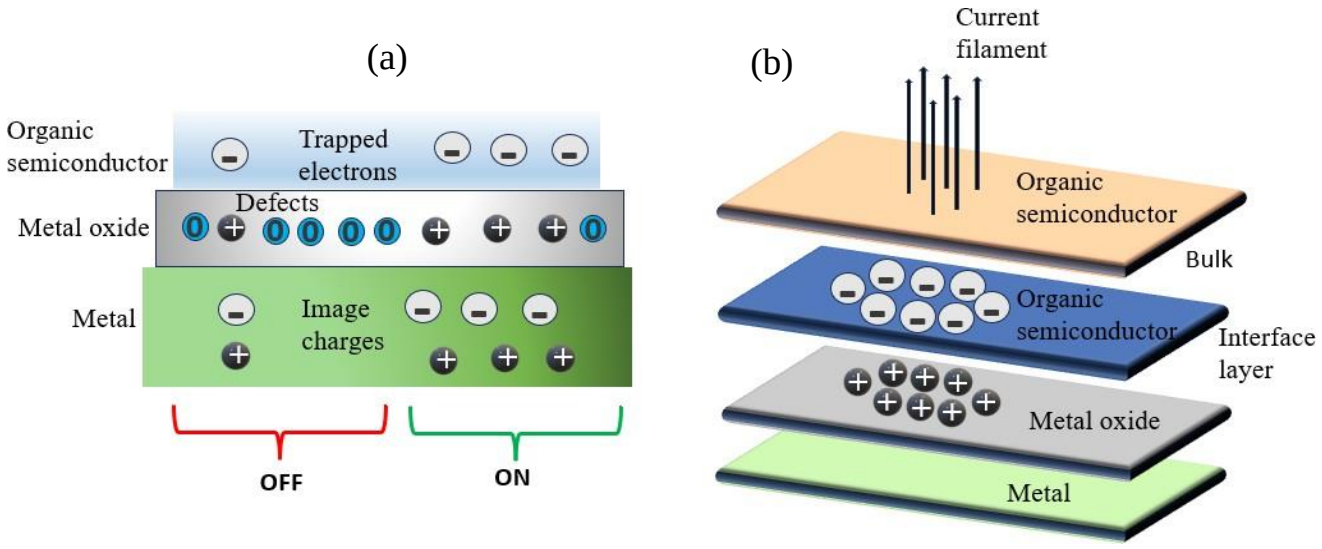


**Figure 2.5**. (a) Illustration depicting charge distribution near the interface between oxide and organic semiconductor materials in electroformed metal oxide-organic semiconductor diodes. (b) Schematic representation illustrating the formation of a current filament.

In some resistive switching devices the operation relies on the migration of anions. Example of materials where this type of switching occur are TiOx, NiOx. The migration of anions is usually described by the migration of their positively charged analogues, i.e. oxygen vacanciesin oxides and nitrogen vacancies in nitrides. During resistive switching, the migration of thesepositively charged vacancies, can lead to change in the valence of cations, thereby providing conditions for flow of electric current. In the literature, memristor structures based on anion migration are commonly referred to as valency change memory (VCM) [82]. Figure 2.6 schematically shows the processes leading to change in resistance in cells based on n- and p- type semiconductor materials. In this case, one main channel is formed, which ensures the flowof electrical current.

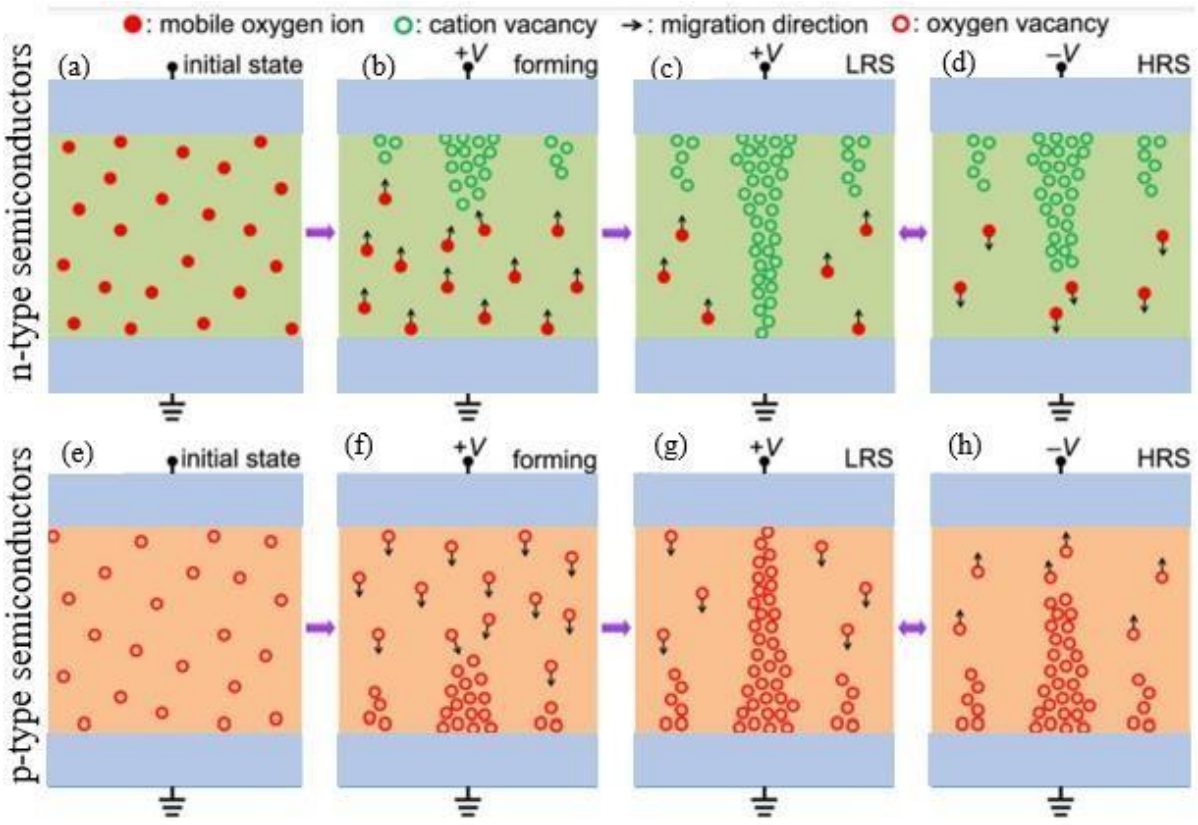


**Figure 2.6**. Schematic representation of the kinetics of anion-dominated switching in p-type semiconductors (a-d) and n-type semiconductors (e-h)

Figure 2.6 (a) represents the initial state with randomly distributed mobile oxygen ions;

(b) Nucleation and subsequent growth from the anode to the cathode of conducting p-type channels consisting of cationic vacancies during formation;

(c) Low-resistance state of a memory cell with a fully formed channel, the thinnest region of which is located near the cathode;

(d) The high-resistance state of the cell, after a partial rupture of the conductive channel in the thinnest region;

(e) Initial state with randomly distributed oxygen vacancies.

(f) The nucleation and subsequent growth from the cathode to the anode of n-type conducting channels, consisting of oxygen vacancies, during the molding process;

(g) Low resistance state of a structure with a fully formed channel for current flow, the thinnest region of which is located near the anode;

(h) High-resistance state after a partial channel break in the thinnest region.

## 2.9 CdS nanoparticles embedded into polymer matrices: A review

Cadmium sulfide (CdS) is a semiconductor material with a direct band gap, width remarkable luminescent properties. CdS nanocrystals exhibit a broad range of potential applications in in diverse fields such optical switches, sensors, electroluminescent devices, lasers and biomedical tags as extensively reviewed in references [83]–[87]. Semiconductor nanoparticles display size-dependent luminescence, optical characteristics, and electrical behaviors, leading to their utilization in various applications across numerous domains [88], [89].CdS nanoparticle belongs to the group of Chalcogenides, it is an II-IV group semiconductor. The CdS nanoparticles exhibits size dependent properties due to its very high surface to volume ratio and quantum confinement at the nanoscale. Among the interesting properties, it has been reported that CdS energy band gap increases as the particle size decreases [90], [91]. Furthermore, CdS nanoparticles also have very high photosensitivity rendering them promising candidate for harvesting visible light. Specifically, they have the potential to enhance the efficiency of solar cells as detailed in [92]. Additionally, CdS nanoparticles have found utility in various biological applications as discussed in [93].

In recent years, there has been a growing interest within the scientific community in polymer–nanoparticle composite materials. These nanocomposite materials exhibit distinctive and highly desirable characteristics, encompassing mechanical strength [94], electrical

conductivity [95], optical and thermal properties [96]. The interesting material properties arise from the interaction between the polymer matrix and the nanoparticles, heavily influenced by the dispersion state of these nanoparticles [97].

## 2.10. Basic optical properties of nanoparticles and nanocrystals

Semiconductor nanocrystals, characterized by their small crystalline structure, have optical and electrical properties that are intricately linked to their size. These nanocrystals, typically measuring between 1 and 100 nm, fill the gap between small molecules and large crystals. They exhibit discrete electronic transitions that are similar to those of isolated atoms and molecules and by allowing the use of crystalline materials' advantageous properties [98].

It is important to discuss the electrochemical properties of CdS quantum dots. The most visible result of the size effect for semiconductor nanoparticles is that the band gap (*Eg*) can be changed by modifying the particle size. Absorption of a photon with energy equal to or greater than the band gap in a semiconductor leads in the excitation of one electron from the valence to the conduction band, leaving a hole in the valence band. Due to the electrostatic interaction between the opposing charges, such an electron-hole pair, or exciton, is held together. The average distance between the photogenerated electron and hole is known as the Bohr radius, which measures the extension of the exciton wavefunction over the crystal lattice. Due to quantum confinement, the optical and electrical properties of a material become dependent on its physical dimension when the particle's size approaches the Bohr radius. Under these conditions, the semiconductor's band structure transforms into discrete levels, and the energy difference between the highest occupied and lowest unoccupied levels widens as particle size decreases, resembling the behaviour of an electron trapped inside a three-dimensional box. The Bohr exciton diameter ($a_B$), which can range from 1 nm to more than 100 nm depending on the material, defines the exciton's limited size within the crystal.

As a result of the nature of quantum dots (QDs) as systems that sit between bulk materials and molecular species, there are some situations in which a description in the context of molecular orbitals is preferable over that in band theory. Additional information about the fundamental aspects can be found in the references [99]–[101].

The optical band gap ($\Delta E_{op}$), can be measured from spectroscopic data and is related to the electrochemical band gap $\Delta E_{el}$, by the equation:

$$\Delta E_{op} = \Delta E_{el} - J_{e,h} \qquad (3.1)$$

where $J_{e,h}$ is the total Coulomb interaction energy of the electron–hole pair. Hence, for any given quantum dot, the electrochemical energy gap is expected to be larger than the optical energy gap [102].

In assessing the impact of quantum effects resulting from nanoparticle size on the broader optical and electrical characteristics, a range of methodologies has been employed, including cyclic and differential pulse voltammetry [103]. Electrochemical studies have demonstrated several distinct oxidation and reduction peaks in the voltammograms with the peak positions being nanocrystal size dependent. In general terms, electrochemical methods are very sensitive to the nanocrystal surface states, providing valuable complementary information for understanding the optical properties of nanoparticles [104]. A recent communication [105], reported about novel electrochemistry of cadmium sulfide quantum dots (Q-CdS) in N,N′-dimethylformamide (DMF). This reference establishes a clear correlation between the electrochemical band gap and the electronic spectra of CdS nanoparticles in DMF. For a comprehensive exploration of the structure and photophysics of semiconductor nanocrystals, an excellent review [19] is readily accessible. This review described the fundamental aspects related with optical properties of nanoparticles. The theoretical background is complemented with very interesting examples of optical spectra for absorption and emission, fluorescence spectra, X-Ray data for different types of semiconductor nanoparticles. CdS quantum dots and their size-dependent optical properties of thiol capping are also described in reference [106]. The QDs have been characterized by UV–Vis, photoluminescence, Fourier-transform infrared spectroscopy, X-ray diffraction, and fluorescence lifetime measurements. From the XRD analysis, it is found that the crystal structure of all samples was cubic. The findings reported in reference [106] are in close agreement with the results presented and discussed in this thesis.

## 2.11. Nanoparticle-based devices for resistive switching

Nanoparticles have found applications in resistive switching devices, and in thiscontext, we review the foundational aspects associated with the use of nanoparticles inmemory-type devices.

Nanoparticles are generally categorized as the class of materials that fall between the molecular and bulk solid limits, with an average size between 1 – 100 nm. Semiconductor

nanoparticles, referred to as quantum dots, with dimensions in the order of nanometres have been the subject of intense research, due to their unique optical, electronic, physical and chemical properties [90], [107], [108].

The uniform dispersion of nanoparticles within nanocomposites is frequently used, such as when they are embedded within a polymer matrix, to attain specific electrical or dielectric characteristics [109]. Nevertheless, achieving a uniform dispersion of ultrafine particles within a polymer matrix can be challenging when integrating pre-made nano-sized particles, primarily due to the propensity for nanoparticle for agglomeration. The most promising strategy for mitigating these challenges and enhancing the dielectric properties of nanocomposites involves the in-situ or direct formation of nanoparticles within the polymer matrix [110].

The general classification of nanoparticles based on their dimensionality, morphology, composition, uniformity, and agglomeration was reviewed in reference[111]. Important nanoparticle morphological characteristics are flatness, sphericity, and aspect ratio. A general classification exists between high- and low-aspect-ratio particles. High-aspect-ratio particles, exemplified by nanotubes and nanowires exhibit diverse morphologies, ranging, helices, zigzags, belts, or nanowires with varying diameters with length. In contrast, low-aspect-ratio morphologies encompass shapes such spherical, oval, cubic, prism, helical, and pillar morphologies. Powders, suspensions, and colloids are all examples of particle collections.

Nanoparticles with interesting optical, dielectric, electric, magnetic, biological and catalytic properties have been explored in a number of applications [58], [90], [99], [112]–[114]. Nanoparticles have also played a pivotal role in the development of various devices [24], [42], [115]–[117], [118], [119]. These nanoparticles, depending on their chemistry and electromagnetic characteristics, can exist in different forms: as dispersed aerosols, in suspensions/colloids, or in agglomerated states. In this thesis, our primary focus revolved around the utilization of CdS nanoparticles embedded within the structure of polymer thin films, a configuration characterized by a low aspect ratio.

Polymer nanocomposites with high dielectric constant have also been under intense research [120]. Polymer nanocomposites hold considerable interest for two reasons. Firstly, they offer large interfacial exchange coupling due a dipolar interface layer, resulting in an enhancement in polarization and polarizability in polymer matrix, particularly in near the interface [121]. As a result, enhanced dielectric constant can be expected in the polymer matrix

near the interfaces. Secondly, the presence of nanoscale particles enables to reduce thethickness of polymer matrix film to nano-scales, and thus increase its high breakdown strength.

Nanoparticles base on binary metal sulphide semiconductors such as ZnS [122], $Ag_2S$ [123], SnS [124], CdSe [125] and others, have attracted the attention of many investigators due to their advantageous structures and nanostructures and their high chemical and thermal stability [126]–[128]. Most of these semiconductor sulphides exhibit a narrow band-gap, which makes them potential candidates for applications in the field of solar cells and as thin film electrodes[129]. Recently, these binary sulphides have been used in other application areas, such as gas sensors and opto-electronic devices [130], [131].

Nanoparticles have been also explored in resistive switching memory devices. Two examples of the memory devices based on nanoparticles are represented on Figure 2.7. A memory device based on indium-oxide nanoparticles is shown in Figure 2.7 (a) [132] and a thin-film planar structures using AgCl nanocrystals embedded in a polymer blend is shown in Figure 2.7 (b) [133].

The observation of switching and memory phenomena in planar structures with non-reactive electrodes shows that this device configuration is an interesting tool to get insight into the resistive switching mechanism. Such planar structures exclude that resistive switching in these systems is related with migration of metal ions into the bulk layer.

The resistive switching mechanism of nanoparticles embed into polymer composites has not been well determined. Some mechanisms have been suggested, such as charge trapping and detrapping [134], and charge transfer between NPs and polymers in an electric field [135].

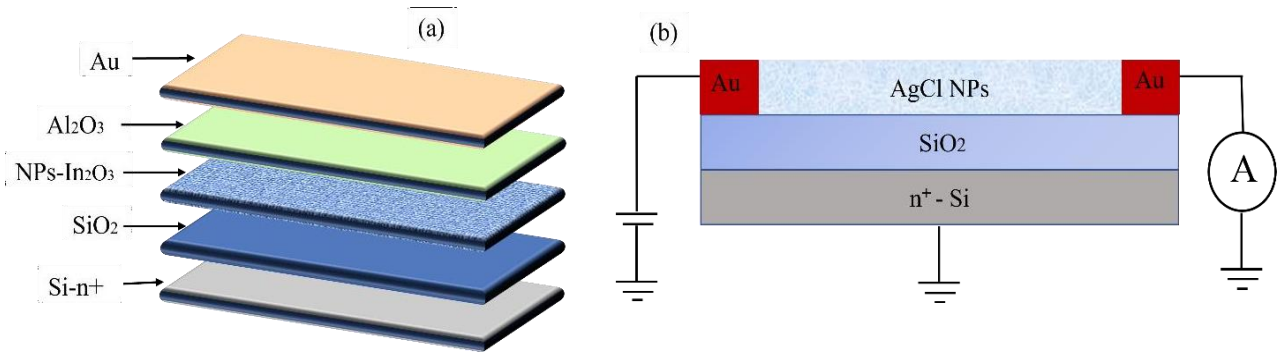


**Figure 2.7.** a) CMOS-full-compatible fabrication techniques were used to insert indium oxide ($In_2O_3$) nanoparticles in a dielectric matrix; b) AgCl nanocrystals embedded in a polymer blend with interdigitated gold microelectrode arrays. Adapted from reference [133].

## 2.12. Summary

A diverse array of resistive switching devices, constructed from various bulk materials or composites employing nanoparticles, has emerged. These memory devices often meet the necessary performance criteria for commercial viability, with interesting attributes such as a high on-off ratio, rapid switching speed, and remarkable endurance. Nevertheless, their path to commercialization has encountered impediments due to a critical challenge: the majority of these switching devices exhibit symmetrical current-voltage characteristics. This symmetrical behavior requires the inclusion of a non-linear element to govern how each cell in a memory array is addressed. To overcome this limitation non-linear elements or selectors such as transistors have been rooted in Complementary Metal-Oxide-Semiconductor (CMOS) technology. However, a significant hurdle arises from the incompatibility of the driving voltages of CMOS devices with the unique materials employed in resistive switching components. Additionally, some of the fabrication processes for these novel materials do not align with the established practices of CMOS technology. Until now the resistive switching phenomena has not led to commercially available memories. The recent trend in research suggests that the resistive switching should be explored to make neuromorphic devices.

# Chapter 3

## *Sample fabrication and characterization techniques*

This chapter describes the sample fabrication procedures and the characterization techniques. Characterization methods include optical, electrical, morphological, and structural characterization. Two types of electrical techniques were used, current-voltage characteristics and small-signal impedance measurements. Impedance measurements were complemented with equivalent circuit modelling in addition, standard material characterization methods to evaluate the morphology and the structure of the materials are also described here.

## 3.1. Introduction

This chapter provides a succinct overview of the methodologies employed in both sample fabrication and characterization. We explore the strategies utilized to control nanoparticle concentration and size, recognizing their critical influence on the material's properties.

Width the objective to understand the effect of nanoparticle size on the electrical and optical properties, we employed various analytical techniques, including structural analysis methods such as scanning electron microscopy, and optical methods like UV-VIS spectroscopy. UV-VIS spectroscopy offers an indirect means of assessing nanoparticle size through its impact on the material's band gap.

To comprehensively characterize these materials, we used two fundamental device

structures: two-terminal devices, which integrate an active layer within a sandwich-like configuration, and three-terminal devices, exemplified by the field-effect transistor. Each of these device architectures is briefly explained within this chapter.

.

## 3.2. Morphological and optical characterization techniques

The conventional methods employed for particle size determination can be found in the listed references [98], [114], [136]–[140]. While there is a variety of tools accessible for nanoparticle size determination, a concern arises from the fact that many of the high-throughput methods available do not meet the rigorous accuracy criteria outlined by the National Institute of Standards and Technology for defining particle size distribution. In this section, we briefly outline the methods employed to determine nanoparticle sizes and their associated properties.

**(a) Spectroscopic Analysis (UV-Visible Spectroscopy)**

UV-VIS spectroscopy is a technique used to quantify the light that is absorbed and scattered by a sample (a quantity known as extinction coefficient, which is defined as the sum of absorbed and scattered light). In its simplest form, a sample is placed between a light source and a photodetector, and the intensity of the light beam is measured before and after passing through the sample. These measurements are compared at each wavelength to quantify the sample's wavelength-dependent extinction spectrum. The data is typically plotted as extinction coefficient as a function of wavelength. To ensure the accuracy of the measurements, each

spectrum is corrected for the background using a “buffer blank” to guarantee that spectral features arising from the buffer are excluded the sample extinction spectrum.

UV-VIS absorption is a very first characterization method for the nanoparticles because the absorption features give information about the nanoparticle formation, the band gap and the size distribution of the nanoparticles. However, it is an indirect method for determining the particle size. The band gap of the particles can be calculated from the excitonic peak position, which is used to determine the particle size with the help of curves of energy gap versus size obtained from theoretical models such as effective mass approximation or semi-empirical tight-binding approximation.

The average radii *r* of cadmium sulfide nanocrystals were determined from the optical absorption spectra, by using expressions for the threshold energy of interband absorption. These optical absorption spectra were measured on an SF-26 spectrophotometer spanning a wavelength range from 320 nm to 600 nm. To reduce the errors associated with the influence of light scattering in the short-wavelength range (320-360 nm) a filter USF-2 was used for cutting the visible area of the spectrum. Our measurements maintained an accuracy, with an error margin not exceeding ±1%. The steady-state absorption and transmittance UV- Vis spectra were obtained using a Shimadzu UV3101PC spectrophotometer scanned between 350 nm and 600 nm.

**(b) Photoluminescence (PL)**

CdS nanoparticles were embedded into different polymeric matrices. It is worth noting that polymeric matrices themselves could show PL, which can, in turn, influence the spectral characteristics of nanostructure. In connection to this, to determine the individual irradiative characteristics of CdS nanocrystals. In light of this, conducted a comparative analysis of the spectral characteristics of CdS nanocrystals within different host matrices, all under identical experimental conditions. This approach allowed us to discern the distinct radiative properties of CdS nanocrystals.

Luminescence properties of CdS have been well described in several excellent monographies and reviews [141]–[145] It is well-established that monocrystals of CdS have luminescence in blue, green, red and infrared regions of spectra.

Several studies into the properties of nanocrystals (NCs) suggest that due to the small size, is anticipated to have a significant impact on the recombination processes involving surface defects [14].This effect is particularly evident in the luminescent characteristics of

nanocrystals. Our objective is to investigate how the luminescent properties of cadmium sulfide nanocrystals depend on the type of matrix in which they are embedded. To achieve this, we conducted photoluminescence emission and excitation measurements on both liquid samples and films of CdS. These measurements were carried out on a SPEX Fluorolog fluorimeter at room temperature measured in the range 350 nm to 750 nm. For the excitation luminescence was excited by a pulse laser LCS-DTL-374QT with a wavelength 355 nm excitation of light (maximum average power - 35 mW, pulse duration at 1 kHz ~ 1 ns, radiation pulse energy at 1 kHz ~ 20 μJ).

**(c) Scanning electron microscopy (SEM)**

SEM is now well established as a method for the study of the structure of nanocrystals. This technique employs a focused beam of high-energy electrons, which interacts with the surface of solid specimens to produce a diverse range of signals. SEM is capable of achieving resolutions better than 1 nm and clear images can be obtained of surface using steps 0.1 to 0.2 nm high. The image intensities are influenced only by the top few layers of atoms, and surface layers consisting of a fraction of a monolayer of foreign atoms can give high contrast [146]. The images made by scanning electron microscopy may be correlated with experimental data from diffraction patterns on the surface and with microanalysis of the surface performed by use of electron energy loss spectroscopy. Usually, when the images are obtained in the scanning mode, with an electron beam of small diameter focused on the specimen, the diffraction and microanalysis data may be obtained from very small regions of the surface.

Surface morphology of the nanoparticles possess various shapes and surface structures that plays a key role in exploiting its properties. Some of the shapes include spherical, flat, cylindrical, tubular, conical and irregular shapes with surface like crystalline or amorphous with uniform or irregularities on the surface. The surface is generally determined by electron microscopy imaging techniques [147].

For the nanoparticle characterization process, we used a state-of-the-art scanning electron microscope: the Zeiss Supra 25 field emission SEM (FESEM) microscope. This instrument has a high resolution, currently at approximately 2 nanometers. Additionally, it is equipped with an advanced EDX Detector X-Flash 3001, featuring Quantax technology by Bruker AXS, Berlin, Germany. This EDX detector operates efficiently without the need for liquid nitrogen, as it is Peltier cooled with a cooling time of less than 30 seconds.

**(d) X-ray diffraction (XRD)**

XRD method is often used to measure the sizes of particles and crystallites in polycrystals in nanoscale. XRD has a good potential for the analysis of nano-structures, because the width and shape of reflections yield information about the substructure of the materials (sizes of crystallites, microstrain of a lattice, dislocation structures, etc.) [140]. English physicists Sir W.H. Bragg and his son Sir W.L. Bragg in 1913 developed a model to explain why the cleavage faces of crystals appear to reflect X-ray beams at certain angles of incidence (theta,Θ)[148]. Bragg's Law describes by the following equation:

$$n\lambda = 2d \sin \Theta \qquad (3.1)$$

Where the variable *d* is the distance between atomic layers in a crystal, and the variable lambda λ is the wavelength of the incident X-ray beam; *n* is an integer. This observation is an example of X-ray wave interference, commonly known as X-ray diffraction (XRD), and was direct evidence for the periodic atomic structure of crystals postulated for several centuries. The Braggs were awarded the Nobel Prize in physics in 1915 for their work in determining crystal structures beginning with NaCl, ZnS and diamond. Although Bragg's law was used to explain the interference pattern of X-rays scattered by crystals, diffraction has been developed to study the structure of all states of matter with any beam, e.g., ions, electrons, neutrons, and protons, with a wavelength similar to the distance between the atomic or molecular structures of interest.

The chemical or elemental composition should determine the purity and performance of the nanoparticle. Presence of higher secondary or undesired elements in the nanoparticle may lower its efficiency and lead to secondary reaction and contamination in the process. The composition measurement is usually carried out by X-ray photoelectron spectroscopy [149]. The crystallography of nanoparticles is carried out by a powder X-ray determine the structural arrangement.

In this dissertation, the structural characterization of the CdS nanoparticles was carried out using X-ray diffraction (XRD) at room temperature in a Philips PW 1710 diffractometer using Cu K-α radiation (λ=1.54184 A), in a Bragg-Brentano geometry, offering high-resolution and high beam-intensity. For a typical XRD diffractogram, the 2Θ angle was scanned in the range $15^{o}<2\Theta<70^{o}$. XRD analysis made using the dried powders obtained by precipitation by means of ionic strength adjustment.

**(e) Raman spectroscopy (RS)**

Raman spectroscopy is a versatile method for analysis of a wide range of samples. It resolves most of limitations of other spectroscopic techniques. It can be used for both qualitative as well as quantitative purpose. Qualitative analysis can be performed by measuring the frequency of scattered radiations while quantitative analysis can be performed by measuring the intensity of scattered radiations [150]. Raman spectroscopy technique is capable of analysing solid and liquid samples quite rapidly. The simplification of spectra caused by resonance allows the easy identification of species contained in complex mixtures.

In this thesis, room temperature micro-Raman spectra were measured on a Jobin–Yvon T64000 spectrometer equipped with liquid nitrogen cooled CCD detector using the 514.5 nm excitation line of an $Ar^+$ laser, with an incident power of 0.2 mW on the sample surface in a 1 m spot and backscattering geometry.

## 3.3. Sample fabrication and characterization

### 3.3.1. Fabrication and encapsulation of resistive switching diodes based on LiF

Samples of LiF diodes were fabricated at Philips High Tech Campus (Eindhoven) as a result of a collaborative project in resistive switching. The methods of preparation are described in references [5], [7], [151]–[153]. Indium-tin-oxide(ITO)/alkali halide/poly(spirofluorene)/Ba/Al diodes were fabricated by thermal sublimation of alkali halide under $10^{-6}$ millibar onto glass substrates with patterned ITO. ITO substrates were cleaned, using in order, acetone, soap scrubbing, and isopropanol. The poly(spirofluorene) (Merck, SPB-02T) was dissolved in toluene at a concentration of 10mg/ml and spin coated at a speed of 3500 rpm. Subsequently, Ba and Al were deposited by sublimation under vacuum. Diodes on ITO substrates were kept under inert atmosphere ($N_2$, $O_2$, $H_2O$<1 ppm) at all times during fabrication and characterization. The Al bottom electrode was deposited by vacuum sublimation using a patterned mask. The LiF was deposited by thermal sublimation under high vacuum onto the entire substrate area. The layer of poly(spirofluorene) semiconducting polymer (CB01, Covion) was spin cast in air from toluene at a concentration of 10mg/ml and spin coated at a speed of 3500 rpm. The top Ba/Al top electrode was thermally sublimated under vacuum through a shadow mask. All the diodes were encapsulated with stainless steel caps glued onto the substrate. At the site where the glue is applied, the semiconducting polymer

was removed by laser ablation to avoid the diffusion of water through the polymer. A getter was placed into the stainless-steel cap to exclude water. The encapsulated diodes have active areas of 1 or 9 $mm^2$. Due to the encapsulation, the devices are stable for years.

Throughout the electrical characterization studies, positive bias is defined as the ITO bottom electrode being charged positive.

### 3.3.2 Fabrication of CdS nanoparticles and nanocrystals

The synthesis of nanoparticles with specific size and controlled size distribution is a crucial aspect of nanoscience. Achieving these characteristics necessitates meticulous control over various conditions, including the choice of solvent, structural parameters, temperature, and more. In our quest to obtain CdS nanocrystals embedded within polymer matrices, we harnessed several methods. One approach involved the chemical precipitation of cadmium sulfide nanoparticles [114]. Additionally, we explored the creation of nanocomposites, wherein conducting polyaniline was integrated with CdS nanoparticles through an in-situ process, achieved by oxidizing the complex formed between aniline and cadmium sulfate [154], [155].

In this thesis the CdS nanoparticles were prepared in different host matrices. Polyvinylpyrrolidone (PVP), Sodium polystyrene sulfonate (PSSNa), Dimethylformamide (DMF) and Photographic gelatin were used as host matrices. Polyvinylpyrrolidone (PVP) is suitable for polymer matrix because it is readily soluble in water and many other organic solvents like Ethanol. PVP has a high dielectric strength, it has a good charge storage capacity and dopant-dependent optical properties [156]. Poly (sodium 4-styrenesulfonate) (PSS) is a well-known polyelectrolyte [157]. PSS may be used to produce mechanically stable and very reproducible coatings. DMF (Dimethylformamide) is common solvent for chemical reactions [158]. Dimethylformamide is an organic compound with the formula $(CH_3)_2NC(O)H$. Preferred IUPAC name is N,N-Dimethylformamide. It is used as an industrial solvent and in the production of fibers, films, and surface coatings.

The choice of the nanoparticle stabilizer is determined by many factors. The major factor is the ability to hinder coagulation of the particles, preventing their further growth. This property of the stabilizer is determined by the mechanism by which it interacts with the surface of the particles. Owing to adsorption of molecular groups on the surface of the nanocrystal formed, passivation of the surface occurs, changing its surface potential and the concentration of nonradiative recombination centers [159]. Moreover, the utilization of non-toxic materials

is of paramount importance in the development of synthesis methods. In this regard, gelatin emerges as a natural polymer often used in the preparation of photographic materials, rendering it a suitable candidate as a stabilizer.

Gelatin is a high molecular weight compound, the elementary unit of which in the isoelectronic state is represented in the form $H_2N–R_1–COOH$, consisting of amino ($H_2N$), carboxyl (COOH), polar, and nonpolar basic and acidic groups ($R_1$). Gelatin is a good dispersion medium for nanoparticles and microparticles. Solutions containing metal and chalcogen ions rapidly penetrate the gelatin. Gelatin solution can form gels from which, when polymerized, rather strong and transparent films are obtained. However, the distinguishing features of gelatin are not limited to only colloid protective functions. Owing to its acid-base properties, gelatin can take on a positive or a negative charge. Thus, for example, as the pH of the medium increases, dissociation of the COOH groups occurs to form $H^+$ and $COO^-$, and the gelatin molecule takes on a negative charge, which can substantially affect the adsorption interaction with the surface of particles dispersed in it. Furthermore, the presence of chemically active impurities in the gelatin can affect the emission characteristics of the nanoparticles. Based on the above, there is interest in obtaining and studying nanocrystals of cadmium sulfide by sol-gel technology using a gelatin solution as the stabilizing agent. The process of synthesis of cadmium sulfide nanocrystals was monitored using optical absorption and luminescence spectroscopy.

To synthesize CdS nanocrystals we employed the sol-gel technology (patented by V. A. Smyntyna et al. in Ukraine) [160]. The synthesis process of these CdS nanocrystals follows a specific procedure. Aqueous solutions containing cadmium and sulfur salts (specifically $Cd(NO_3)_2$ and $Na_2S$) were introduced simultaneously, at a consistent rate, into a 5% gelatin solution, all while maintaining continuous stirring at 40°C. This approach employed an equimolar ratio of cadmium and sulfur salts. The formation of cadmium sulfide was achieved through an exchange chemical reaction facilitated in the presence of the gelatin solution:

$$Cd(NO_3)_2+Na_2S \Longrightarrow CdS+2NaNO_3$$

The solution was stirred and turned to yellow color immediately due to the formation of CdS nanoparticles. The colloidal solution formed was sprinkled onto glass substrates specially treated for better adhesion of the films, which after sprinkling were dried in air at room temperature during at least 24 hours. Polymerization of the gelatin occurred during drying. The finished samples were films of thickness 5–10 μm, containing cadmium sulfide nanocrystals dispersed in a gelatin matrix. Depending on the technological factors (concentration of

reactants, synthesis temperature, concentration of gelatin), the color of the films varied from pale yellow to bright orange.

The pH of the solutions were adjusted throughout the synthesis procedure. We increased the pH by introducing an alkaline sodium hydroxide (NaOH) solution, while for pH reduction, we utilized hydrochloric acid (HCl) or acetic acid ($CH_3COOH$). pH measurements were carried out using an ionomer-based pH meter. The resulting solutions exhibited a spectrum of colors, ranging from light yellow (at pH 4) to a deeper, darker yellow (at pH 10).

Upon completion of the synthesis process, the solution containing suspended CdS nanoparticles within the gelatin matrix was carefully drop-cast onto glass substrates. Subsequently, it was allowed to dry, leading to the solidification of the gelatin gel.

Using the previously outlined preparation technique, we successfully embedded cadmium sulfide nanoparticles into various polymer matrices. These matrices included photographic gelatin; N, N-dimethylformamide (DMF) from AnalaR NORMAPUR®, polyvinylpyrrolidone (PVP) with a molecular weight of 40 kD, and polystyrene sulfonate sodium salt (PSSNa) with a molecular weight of 30 kD. All purchased from Sigma Aldrich®.

Electrical and optical measurements were carried out both in liquid solutions as well as in solid thin films deposited on different types of substrates. Once the synthesis is completed, a drop of solution containing suspended nanoparticles of CdS, was dropped on the substrates and left dried during 24 hours at room temperature. Solutions with high concentration of CdS nanoparticles were produced by centrifugation. When dried in the oven at 65 °C overnight, the thin films naturally peel-off from the glass substrates leading to a free-standing film with thickness in the range 2-5 µm.

Different kind of substrates were used; (i) transparent glass slide coated with a gold contact, (ii) thermally oxidized silicon wafers and highly doped *n*-type silicon wafers. Schematic diagrams of the device structures using CdS NPs thin films are shown in Chapter 7.

## 3.4. Devices and electrical characterization techniques

Several electrical characterization techniques were used, these include current-voltage characteristics (*I-V*), electrical impedance as function of the frequency and electrical noise measurements. For electrical measurements, samples were deposited on different types of substrates. Namely, highly doped *n*-type silicon wafers, glass slides coated with a thin layer of gold (thermal evaporated), and transistor like architectures where the dielectric layer is $SiO_2$

(600 nm thick) or a ATO layer (200 nm thick). The transistor was a metal-insulator-semiconductor field-effect transistors (MISFETs) type. MISFETs with different type of dielectric layers were fabricated. Some MISFETs were based on thermal oxidized silicon wafers (see Fig. 3.1 (a)) Other MISFETs use for dielectric layer, a thin film known as ATO (see Fig. 3.1 (b)). ATO is a dielectric of successive intercalated layers of $Al_2O_3$ and $TiO_2$ deposited by atomic layer deposition. ATO is deposited on top of ITO coated glass substrates. MISFET based on ATO are transparent. ATOs substrates were purchased from *Planar Systems*, Finland.

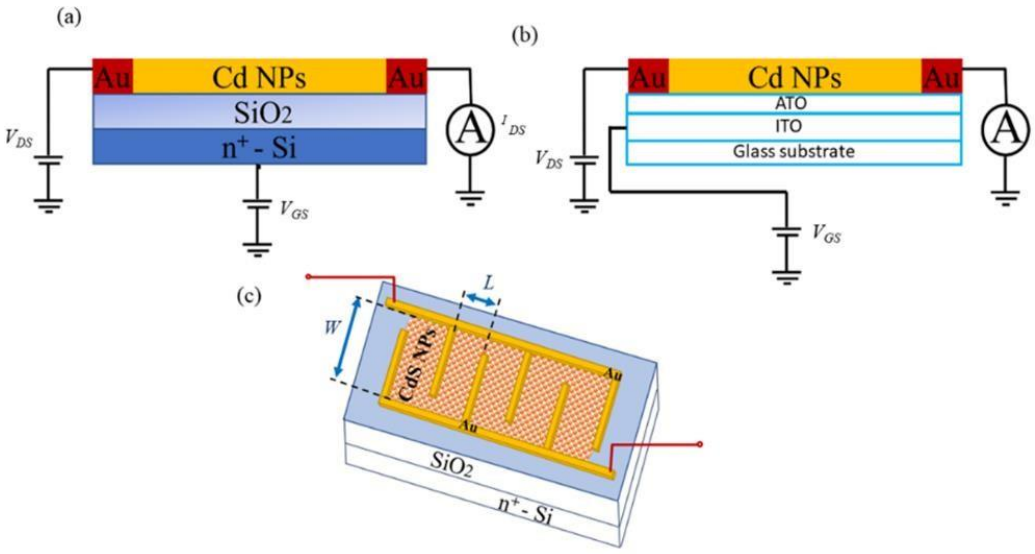


**Figure 3.1**. Schematic diagrams of the MISFET structures used as electrical characterization tool. (a) MISFET based on a silicon substrate, (b) MISFET based on ATO substrate from *Planar Systems* and (c) the schematics of the top electrode interdigitated geometry. Interdigitated electrode dimensions are $L$=10 μm and $W$=1000 μm. There are 11 interdigitated fingers which make the total width of the device equal to 10.000 μm.

CdS free standing films were also obtained by peeling-off the deposited thin-films from the substrate. These films are typically 2- 3μm thick. Electrical connections were made by gold wires connected using conductive silver paint to both surfaces of the free-standing film.

Current–voltage ($I$–$V$) curves were obtained using a Keithley 487 picoammeter. Current sweeps and constant current stress were carried out by a semiconductor parameter analyser, Agilent 4156C. A blue LED ($350 \leq \lambda \leq 650$ nm, $\lambda_{max}$=440 nm) was used as optical excitation source.

MISFET devices were often only used as a two terminal device. In the two terminal configuration, the MISFET structure was basically operating as planar junction with two symmetric gold electrodes. During this characterization, the silicon substrate (or the ITO Layer) is kept grounded to avoid charging of the dielectric layer by free charges passing through the CdS thin film. Prior to measurements, the quality of the dielectric was also evaluated by applying a strong electric field across it.

Measurements were also carried out using a MISFET channel only the polymer (PVP) matrix (without the nanoparticles). The goal was to inspect for the effects of the polymer matrix alone on the electrical properties.

Nonvolatile resistive switching memories studied in this thesis were based on a LiF layer and an organic semiconductor, the spirofluorene. Figure 3.2 shows the schematic diagram of the LiF based device. Figure 3.2 (a) is a photograph of an encapsulated device. Figure 3.2(b) is the top view where 5 devices with three different active areas are highlighted. The internal structure of the memory device is a sandwich structure containing a few layers schematically shown in Figure 3.2 (c). It consists of an Al top electrode, a layer of LiF with thickness of 20 nm, a polymer - spirofluorene (80 nm), and a Ba/Al (5 nm/100 nm) bottom electrode that forms an ohmic contact with the polymer. Positive bias voltage refers to the top Al electrode being positive with respect to the bottom Ba electrode.

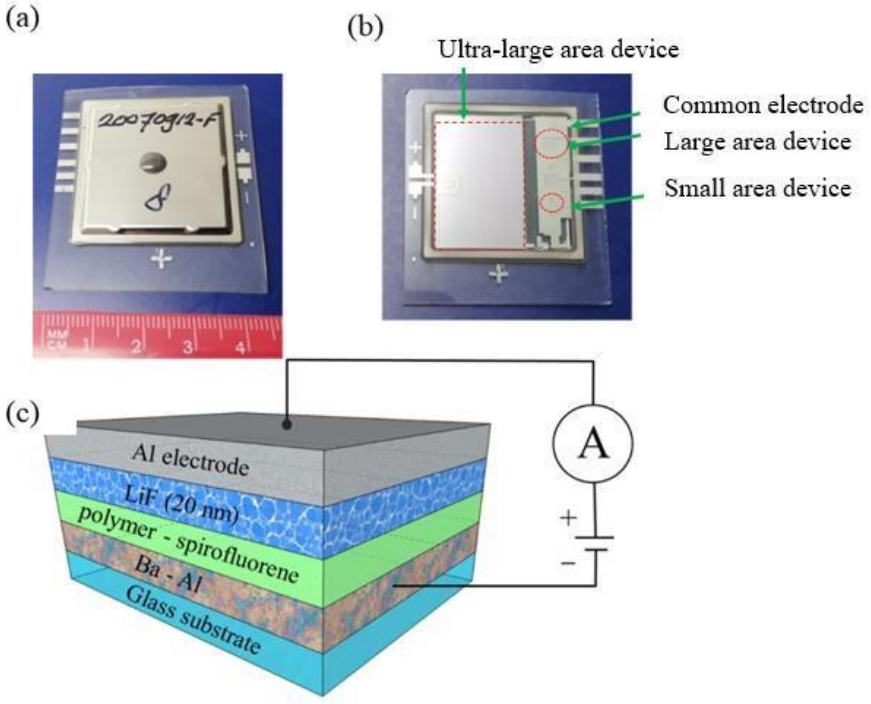


**Figure 3.2.** (a) Photograph of an encapsulated LiF device, (b) Top view showing two devices with two different areas, active areas of 1 and 9 $mm^2$ were used in this study. (c) Schematic diagram showing the device structure and the electrical connections.

# Chapter 4

## *Electroforming and resistive switching on LiF diodes*

This chapter describes electroforming and resistive switching mechanism in Al/LiF /poly(spirofluorene)/Ba/Al diodes. Pristine devices were turned into programmable resistive switching memories by applying a voltage value called the forming voltage. When the amplitude of the applied voltage reaches the forming voltage, a sharp and irreversible increase in the conductivity is observed. After this electroforming process, the devices exhibit bistable *I-V* characteristics symmetrical with respect to the polarity of the applied voltage, and a negative differential resistance (NDR) region in the ON state. Once electroformed, the diode behaves as a memory and can be programmed between a high conductive and a low conductive state using voltage pulses below and above the NDR region, respectively.

Small-signal impedance measurements reveal that an internal field due to trapped electrons at the LiF/polymer electroforms the device. This study looks into detail at the trapping/departing kinetics and their influence on the hysteresis loops of resistance and capacitance *vs* voltages curves. The detrapping current causes two anomalous effects; (i) a negative differential resistance region on the resistance *vs* voltage curve and, (ii) an excess small-signal capacitance in capacitance-voltage curves. Both anomalous behaviors are only observed on the return path of a voltage-sweeping scan.

Frequency and bias dependence of the impedance confirms that LiF/polymer interfacial traps are still playing a role when the device is electroformed.

## 4.1 Introduction

Resistive switching memories based on binary transition metal oxides, perovskite-type complex and in large-band-gap oxides, and metal halides are Metal-Insulator-Metal (MIM) structures that after an application of a voltage or a current are turn into programmable memory devices. As fabricated, MIM devices have very high resistances and need to be activated in order to function as a memory device. The activation process entails subjecting the MIM structure to a biased voltage stress bringing it close to the threshold for the insulator dielectric breakdown. During this soft-dielectric breakdown, defects are induced into the insulator. This initializing effect, driven by the intense electric field strength, is commonly known as electroforming. Electroforming gives rise to a network of percolating paths that facilitate charge transport, often referred to as conducting filaments. The number of filaments created during electroforming determines the number of resistance levels that can be programmed within the device. This network of programmable filaments holds particular significance for neuromorphic-like devices characterized by a wide distribution of resistance levels.

The electroforming and the subsequent defect creation are proceeded by a trap filling process. While the research has extensively explored the defects generated during electroforming, studies addressing the early stages of electroforming where interfacial traps are filled by the applied voltage are scarce. This gap in the research is somewhat surprising, given that oxides cannot undergo electroforming without this trap-filling process. It is important to underscore that trap-free oxides submitted to an electric stress solely experience hard dielectric breakdown leading to a permanent damage of the insulator. The attainment of reversible or programmable resistive states are only possible to achieve if the insulator has surface impurities (traps). Remarkably, historical research conducted between the 1960s and 1970s revealed that an unidentified layer of carbon significantly enhances the reproducibility of memories [153]. Diodes fabricated in high vacuum did not exhibit switching behavior. Achieving reliable memories necessitated the introduction of oil vapour contamination from a rotary pump [161]. The accumulation of charge within these impurities generates an internal electrical field across the oxide, triggering a soft dielectric breakdown and yielding bistable defects within the oxide layer. Basic memory properties, such as, on-off ratio, charge retention time and number of programmable conductance levels should be largely influenced by the density and spatial distribution of surface traps. Furthermore, it is widely recognized that resistive switching processes are inherently filamentary in nature, with only a fraction of the sample undergoing switching behavior.

The spatial arrangement of switching regions across the entire device area is inherently linked to the distribution of traps on the surface of the insulator. Hence, identifying the chemical origin of these traps is crucial towards creating high-performance resistive switching memories. For instance, mastering the art of uniformly distributing traps across the device surface holds the potential to render the entire device area programmable, ultimately yielding a memory device with an exceptionally high on-off ratio.

Despite the crucial role that traps play, influencing both electroforming and memory performance, critical trap properties, including their energetic depth, density, and chemical origin, have remained largely unexplored in existing literature. This knowledge gap stems from the formidable experimental challenges associated with detecting charges trapped at the insulator surface.

In resistive switching devices traps exhibit rapid filling kinetics, typically occurring within seconds, while their emptying process is considerably slower, spanning hours, days, or even months. These long-time constants make unpractical the observation of the trap filling and emptying kinetics using classical approaches. These methods were originally tailored for silicon-based devices, where even a trap with an energy depth of 0.1 eV is already considered a deep trap and empties in a time scale of seconds.

In this study, we gather information about the traps by employing small-signal impedance measurements. However, we deviate from the conventional approach used in silicon-based metal-oxide-semiconductor (MOS) devices, where the focus lies on examining the frequency response of trap filling and emptying kinetics. Instead, our approach centers on measuring how trap occupancy modulates the quasi-static impedance of the device. To enhance our understanding of trap locations within the device's geometry, we complement the impedance measurements with equivalent circuit models.

The organization of this chapter is as follows: following an overview of the experimental details, we embark on a review the current understanding about electroforming of memory devices. Subsequently, we consolidate insights from various studies reporting the observation of traps at the onset of the electroforming alongside a diverse array of electro-optic techniques employed to investigate these trap states. We then present and discuss the results. It is shown that a trap filling process cause abnormal hysteresis on the impedance versus voltage curves. Specifically, the neutralization of traps manifests as a negative differential resistance (NDR) region on the resistance-voltage curve and an abnormal excess capacitance

in the capacitance-voltage plot. The changes caused in the impedance after electroforming are also discussed. Finally, the implications of this knowledge in the development and optimization of resistive switching memory devices are discussed.

## 4.2 Experimental section

Figure 4.1 shows a schematic diagram of LiF diode structure. The photograph of the diode is presented on the Figure 4.1 (a). The structure of the diode is schematically depicted in Figure 4.1 (b). It consists of an Al top electrode, a layer of LiF with thickness of 20 nm, a polymer - spirofluorene (80 nm), and a Ba/Al (5 nm/100 nm) bottom electrode that forms an Ohmic contact with the polymer. Positive bias voltage refers to the top Al electrode being positive with respect to the bottom Ba electrode. Current – voltage (*I-V*) characteristics were measured using an Agilent semiconductor parameter analyser 4155C. *I-V* measurements were carried out with scanning speed from 10 mV/s up to 100 mV/s for Capacitance-Voltage (*C-V*) plots. Impedance *vs.* voltage characteristics were measured by impedance analyser Fluke 6406.

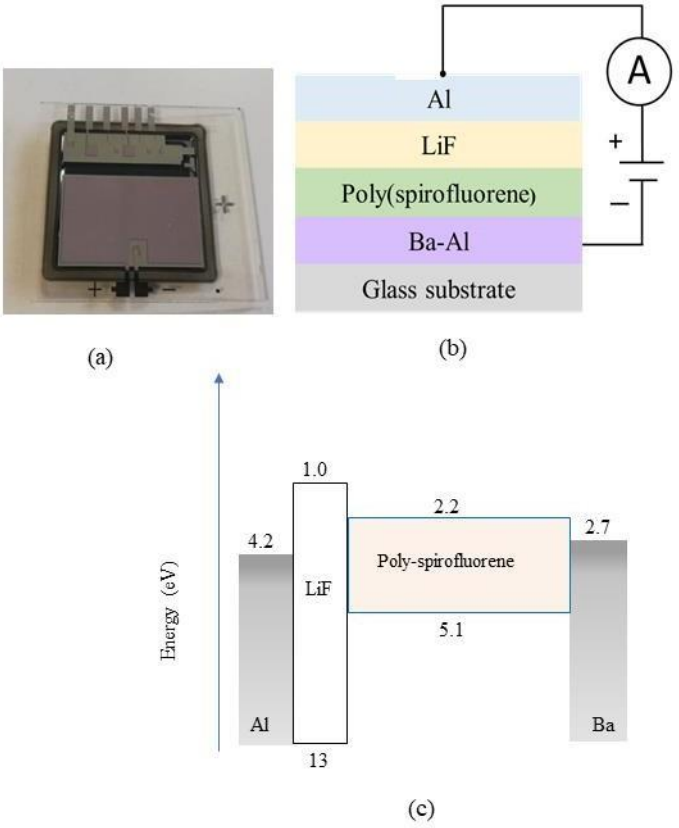


**Figure 4.1.** (a) Photograph of several encapsulated LiF based devices. (b) Schematic diagram showing the device structure and electrical connections. (c) Flat band diagram illustrating the valence and the conduction bands of poly(spirofluorene) and LiF and the work functions of Al and Ba with respect to the vacuum level.

## 4.3. Trapping of electrons in the initial stages of electroforming: a review.

Existing reviews about electroforming are essentially focused on two aspects of electroforming, (i) on the electrical procedures to achieve electroforming [162]–[165] and, (ii) on the nature of the defects created during electroforming [166]. In contrast, this review is focused on the trapping phenomena occurring in the early stages of electroforming.

The basic methods of electroforming rely on applying a voltage or a current sweep. When using a voltage sweep, it is typically necessary to incorporate a compliance current to mitigate the effects of Joule heating and imped hard dielectric breakdown. In contrast, electroforming driven by a current-sweep ensures that the current passing through the device remains under control, eliminating the need for compliance. The precise nature of the defects created during electroforming is still a matter of debate. The models proposed in the literature vary according to the material used. For instance, electroforming of $Al_2O_3$ has been attributed to formation and ionization of defects [33], [167], [45]. Electroforming of $TiO_2$ based memory devices has been shown to induce a phase transition to the Magnéli phases ($Ti_nO_{2n-1}$) at localized spots and is associated with formation of oxygen vacancies [167], [168]. Similarly, electroforming of niobium oxide ($Nb_2O_5$) results in formation of suboxide phases [167]. Also for hafnium oxide ($HfO_2$), electroforming has been related to oxygen vacancies [166]. In Cr doped $SrTiO_3$, oxygen vacancies have been imaged after electroforming and seem to determine the path for electrical conductivity [33]. In general terms, we may summarize the current view of the electroforming as follows: The application of a forming voltage introduces oxygen vacancies by oxidation-reduction reactions with the metal contacts. A continuous sequence of oxygen vacancies forms a filamentary conduction path across the oxide and leads to a low resistance state. Applying a reverse voltage changes the number or distribution of oxygen vacancies and causes the rupture of the conducting filament. Many review articles presented diagrams illustrating this mechanism [33], [167], [169]. However, electroforming and switching have also been reported in many non-oxide based MIM systems, including nitrides, halides, and pnictides [30], [151], [169], [170]. Electroforming and switching in these non-oxide systems does not involve oxygen vacancies. In order to explain electroforming in these systems Hickmott [167], argued that the formation of defect conduction bands in non-oxide systems can occur when the defect concentration is large enough, $\gtrsim 10^{19}$ $cm^{-3}$, as it is likely to be in amorphous or evaporated films. The existence of defect conduction bands in MIM diodes that depends on the details of formation of the insulator also explains why such a wide range

of metals, both reactive and unreactive, can be used for the counter electrodes. Supporting this electronic view is the observation of electroluminescence [32], [171].

For the LiF diodes under study in this chapter, the nature of the defects created during electroforming has been previously studied and reported by the Eindhoven group [151]. For the LiF it is proposed that a self-trapped exciton dissociates into a Frenkel defect pair consisting of an anion vacancy filled with an electron (F-center) and a halide interstitial (H-center). Under prolonged bias stress, defects will accumulate, and F-center aggregates are formed. The electroformed alkali halide layer is considered as a highly doped semiconductor with metallic transport characteristics.

Electronic models are very appealing because if electroformed MIM diodes are to be used for memristors or for non-volatile memories they require high switching speeds. Electronic process is significant faster than electrochemical based process that depend not only on electron motion but also on chemical reactions between insulator and metal.

In the context of the present work, interesting models are the ones that rely in a pure electronic mechanism as the one proposed in the early days of the history of resistive switching memories by Hickmott [36], [172], [161], [162]. According to Hickmott's model, electroforming induces the creation of an impurity energy band in the oxide band gap, which serves as a low-energy electronic pathway [26], [27]. This impurity band is strategically positioned in the vicinity of the Fermi level of the cathode, facilitating the injection of electrons into the impurity band. Hickmott proposed that this impurity band has origin on the impact ionization of immobile impurities. Simmons and Verderber proposed a similar model, differing only in the origin of the impurity band [45]. In their model, metal ion injection from the electrode was regarded as the origin of the impurity that forms the impurity band in the forbidden gap. Alternatively, Dearnaley et al. [28] introduced the filament mechanism where conducting filaments (CFs) are introduced in the insulating matrix during forming. This, in turn, results in non-uniform conductivity within the switching material [27]. In the filament model, it is assumed that CFs originate from multiple points at the insulator/anode interface, where the local electric fields are concentrated [46].

Studies reporting trapping phenomena prior to electroforming are not abundant in the literature. Most of the work in this topic has been carried out by groups led by Dago de Leeuw at Philips (Eindhoven), Stephen Meskers at TU/e (Eindhoven) and by Gomes H.L. at the University of the Algarve (Portugal). Together, these groups have collectively published a number of studies, which provide direct evidences of a trapping phenomena occurring in the

early stages of electroforming. These studies were conducted in resistive switching memories integrating polymer layers. It is worth noting that while these devices contain a polymer layer, they are often colloquially referred to as "polymer-based resistive switching memories." In reality, the switching layer in these devices remains an oxide, such as $Al_2O_3$ or a halide for instance LiF. Therefore, their basic switching mechanism is indistinguishable from an oxide-based memory. Importantly, unlikely, most of the MIM type of devices documented in the literature, polymer based resistive memories are not MIM but instead, metal-insulator-semiconductor (MIS) structures. In a MIM structure the charge carrier communicates directly with the metal bands, and this makes both the charge carrier injection and extraction a relative fast process but also difficult to measure.

The semiconducting polymer layer in series with the insulator has the interesting effect of slowing down the carrier injection as well as the carrier extraction into the trapping sites.

This slowing down of the trap filling kinetics is due to the relatively low mobility of the π–conjugated polymer. The poor carrier extraction and injection has a detrimental effect inthe switching speed of a memory. For this reason, memories integrating π–conjugated polymershave not attracted the attention of the scientific community. However, MIS type of memories using a polymer as a semiconductor layer are a powerful characterization tool to provide insightinto the fundamental physics occurring in the early stages of electroforming of oxides, halidesand other resistive switching materials. This aspect has not been fully appreciated by the scientific community, as most of the characterization studies are still carried out in MIM structures optimized to operate as resistive switching memories.

Evidence for trapping at the onset of electroforming can be provided by a number of methods and techniques. These include; (a) quasi-static capacitance-voltage (QSCV) methods, in which a voltage ramp or a voltage step is applied to change the trap occupancy and the corresponding quasi-static changes in capacitance as well as in resistance are monitored; (b) photo-induced current transient spectroscopy methods where traps are filled with a voltage and neutralized by exposure to polymer band-gap light; (c) quenching on the semiconductor polymer photoluminescence or, (d) changes in the optical reflectivity caused by the presence of free carriers, and finally (e) by low frequency noise measurements. Figure 4.2 shows a schematic diagram where the methods to detect traps in polymer based resistive memory devices are briefly outlined. In the following paragraphs, a short description of each method is provided.

**(a) Capacitor displacement current method**

The capacitor displacement method makes use of MIS capacitor. Before the displacement current method is explained and their use justified it is useful to recall the behaviour of the small-signal capacitance when the MIS diode is driven by a bias sweep voltage. Under forward bias, free charge carriers accumulate at the insulator/semiconductor interface and the measured capacitance is the insulator capacitor ($C_I$). Under reverse bias, the semiconductor is depleted of free charge carriers and the measured capacitance is the series sum of the semiconductor capacitance ($C_s$) and insulator capacitance ($C_I$). Therefore, a *C-V* plot evolves from a low capacitance plateau under reverse bias to a high capacitance plateau under forward bias. This is the typical behaviour of trap free MIS capacitor. Under the presence of deep traps this behaviour is different. Under forward bias, the current that flows through the device is a transient current that only lasts a few milliseconds, which is the typical time required to fill the traps. Once the traps are filled, the current stops and the semiconductor becomes depleted of free carriers. Small-signal impedance methods of measuring the capacitance have difficulties in capturing this transient change in capacitance (in a time scale of milliseconds). In a small-signal *C-V* plot the depletion and accumulation plateaus on the *C-V* curve will not be observed and the *C-V* is flat. This is because at a particular test signal frequency and under steady state, the traps become filled very fast and the impedance analyser only perceives the steady state capacitance which is the series sum of $C_s$ and $C_I$.

In order to measure the changes in trap occupancy, the capacitance cannot be measured by a small ac signal method but instead by the displacement current method. This method relies on driving MIS capacitor by a well-defined voltage ramp speed ($dV/dt$). The measured current is is a displacement current ($I$), which is related with the capacitance according to equation (4.1).

$$I(t) = C\frac{dV(t)}{dt} \qquad (4.1)$$

Where $C$ is the device capacitance and $dV/dt$ is the voltage ramp speed.

Figure 4.2 (a) illustrates the experimental procedure. When a MIS capacitor with all the traps emptied is submitted to a voltage ramp, a current flow through the semiconductor layer and fills the traps at the insulator/semiconductor interface. This trap filling current effectively bypass or “shorts” the capacitance of the semiconductor layer. The measured displacement current corresponds only to the insulator layer capacitance ($C_I$). Once the traps are filled, the

current trough the semiconductor stops. The semiconductor becomes depleted of free carries and behaves as an insulator. The semiconductor capacitance ($C_S$) appears now in series with the insulator capacitance ($C_I$). The device behaves as a two-capacitance layers in series and the displacement current measures the series sum of $C_I$ and $C_S$. In summary, upon the application of a forward bias-sweep voltage to a trap empty MIS capacitor, the measured capacitance is high and equal to $C_I$. If the voltage ramp is stopped the capacitance rapidly decays to the series sum of $C_I$ and $C_S$. In the return path of the bias-sweep voltage the traps remain filled and measure capacitance also corresponds to the series sum of $C_I$ and $C_S$. This change between the two capacitance values is schematically represented in Fig. 4.2 (a). The high hysteresis *I-V* loop can only be repeated if the sample is left resting for a few days under short-circuited conditions. The use of the current displacement method to study electroforming in $Al_2O_3$ and LiF based devices has been reported in the references [36], [172].

Alternatively, traps may also be filled with a voltage step. The corresponding decay in current is monitored as function of time. This method is known as current transient spectroscopy (CTS) method. However, in our LiF capacitors, the filling time is not controlled by the traps but, as it will be shown later, the trap filling kinetics is controlled by the time of flight of the charge carrier trough the semiconducting polymer layer. Therefore, current transients do not provide information about the traps, but instead, they reflect the charge transport mechanisms across the low mobility conjugate polymer.

**(b) Photoinduced detrapping measurements**

A convenient way to neutralize traps is to expose the MIS capacitor to polymer band-gap light. Photogenerated holes will recombine with the trapped electrons leading to a trap neutralization process. This trap neutralization can be monitored by recording the associated current transient during illumination. Under illumination, discharging currents are observed on the time scale of hundreds of seconds as is schematically shown in Fig. 4.2 (b). The density of trapped charge can be calculated from the area under the optically induced current transient. Detrapping transients are faster for higher optical power, in agreement with first order kinetics. Once the traps have been emptied optically, the filling of the traps can be repeated. Charging of traps by an applied voltage and discharging them by exposure to light is a fully reversible process. The basic steps of this method are depicted in Fig. 4.2 (b). This method was reported in a study by Qian Chen et al.[172]

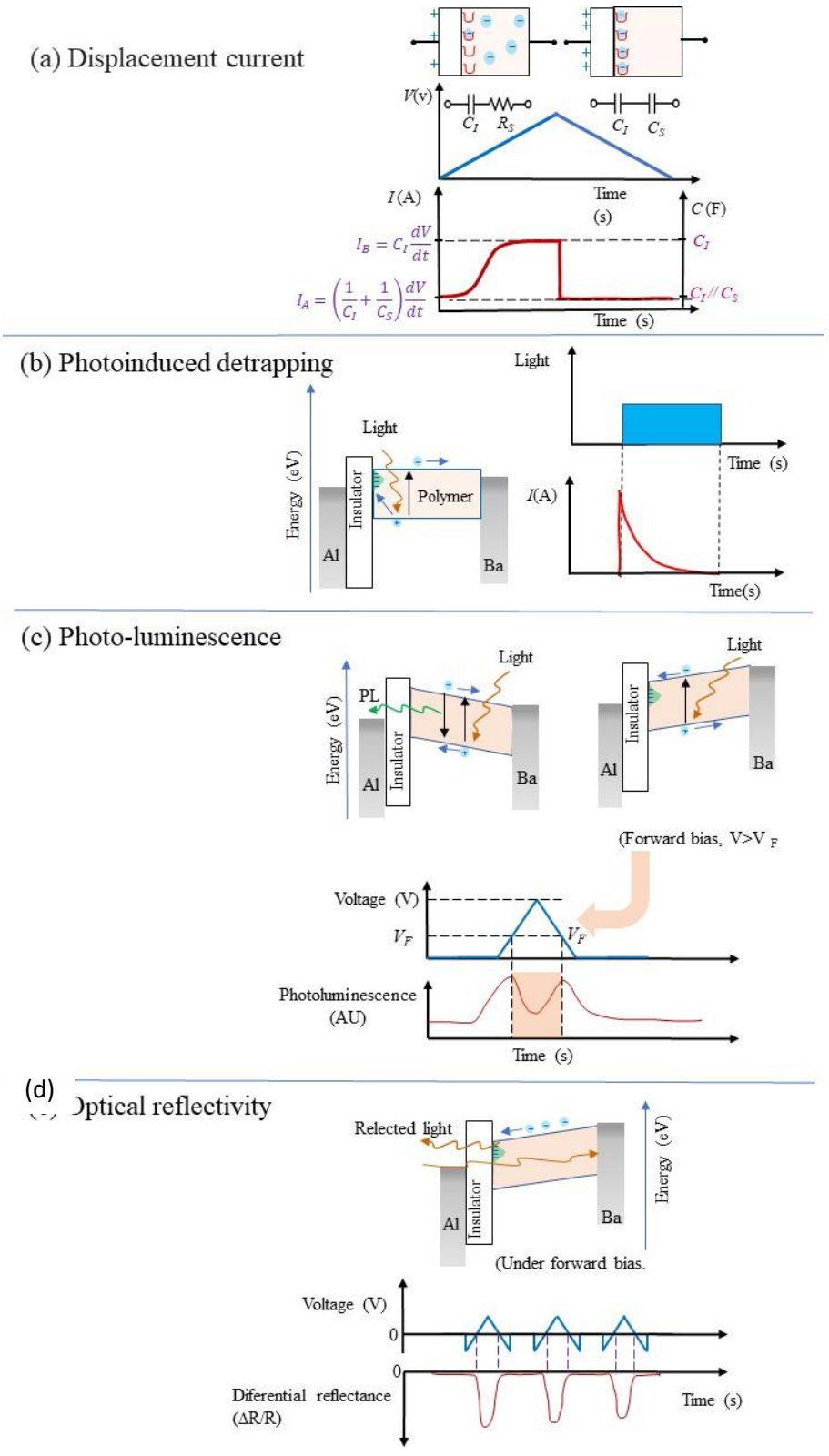


**Figure 4.2.** Schematic diagram representing several methods which have been used in the literature to gain information about interfacial traps at the insulator/semiconductor interface. (a) displacement current method, (b) optical induced detrapping, (c) Quenching of the photoluminescence and (d) change in the optical reflectivity caused by the presence of charge carriers.

**(c) Photoluminescence**

Free charge carriers flowing in and out of the trapping sites, may also be detected by the changes caused in the photoluminescence of the polymer. In photoluminescence experiments electrons are excited from the valence to the conductance band of the semiconducting polymer by a light source with energy larger than the bandgap. As a consequence, the photo-excited carriers relax and then spontaneously recombine with holes in the conduction band. In the case of direct semiconductors, the excess energy is emitted in the form of light (spontaneous emission). In π-conjugated polymer the presence of charge carriers interferes and causes a quenching on the photoluminescence. For the LiF/polymer interface, Bory B. et al. [1] have shown that upon the application of a voltage ramp above a certain voltage, the photoluminescence intensity drops (see the schematic diagram on Fig.
4.2 (c). This change in the photoluminescence was attributed to injection and consequent accumulation of electrons near the LiF/polymer interface, which then are captured at interfacial trapping sites.

**(d) Optical reflectivity measurements**

When the memory device has a transparent bottom ITO contact, illumination trough the contact provides direct access of the light to the sample. In addition, the Ba/Al top contact is highly reflective, allowing for reflectivity measurements. Upon application of a stepped bias voltage, the intensity of the reflectivity band increases slowly over time. Importantly, upon removing the applied bias, the reflectivity reverts spontaneously and slowly approaches its original level before application of bias stress. The recovery can be accelerated by application of reverse bias. The experimental procedure is illustrated in Fig. 4.2 (d). By measuring the current density through the diode simultaneously with the change in reflectivity at the wavelength of 800 nm during the bias stress and the subsequent recovery, Bory B. et al. [151] established a correlation between the changes in optical properties and the charging on trap occupancy. During recovery from the bias voltage stress under short circuit conditions, a spontaneous discharging current with sign opposite to that of the current density during bias voltage stress was observed. The decay of the short-circuit discharging current takes place on the same timescale as the decay of the differential reflectivity. The correlation between optical and electrical signal indicates that coloration and its recovery are related to charging and discharging of traps at the LiF/polymer interface.

**(e) Electrical noise measurements**

Evidences for traps can also be found from low frequency electrical noise. Prior to electroforming (pristine samples) show a low frequency noise that follows a $1/f$ frequency dependence. After the electroforming the noise changes to a frequency dependence of the type $1/f^{3/2}$ [7], [46]. Hence, upon electroforming a new physical mechanism becomes active. This mechanism is a switching-on and switching-off of conducting filaments. Authors affirm in reference [47] that while the statistically significant capture/emission of electrons at electron trap sites controls the charge transport, discrete variations in current-voltage or current-time properties are being develop.

## 4.4 Results and discussion.

Figure 4.3 compares three *I-V* curves corresponding to the different electrical states of LiF memory device. The lowest (a) *I-V* curve corresponds to the pristine state. The middle (b) curve corresponds to the off-state (after electroforming) and the top curve (c) corresponds to the on-state. The pristine state is irreversible. The on-state was recorded to sufficiently high voltages to observe the differential negative resistance curve. During the NDR region, the device partially switches-off, as a consequence the return path of the *I-V* curve occurs at a lower current than the forward path. This leads to an *I-V* curve with hysteresis.

To program the memory in the off-state (middle curve in Figure 4.3 we applied a voltage above the NDR region for a few seconds (2 s). To restore the on-state we apply for several seconds a voltage below the NDR region. The on/off ratio is roughly 100.

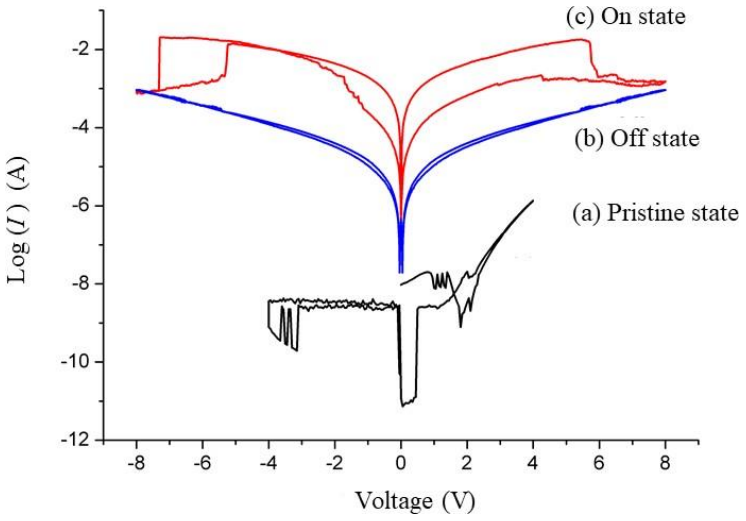


**Figure 4.3**. Current-voltage (*I-V*) characteristics of the device in the different sates: (a) pristine, (b) off-state and (c) on-state.

To inspect for difference on the impedance on the different device states. The small-signal impedance properties of the LiF diode on the different states were also recorded. Figure 4.4 shows the frequency dependence of the capacitance for the on- and for the off-state. As described in a previous Chapter (fundaments of electrical techniques) the system behaves as a two-layer system. The transition from the low frequency capacitance plateau to the capacitance plateau located at high frequencies, defines the Maxwell-Wagner relaxation which is located at around 10 kHz for a typical LiF diode. At low frequencies we see essentially the capacitanceof the interface, and at high frequencies (above the Maxwell-Wagner relaxation) we see the series sum of the bulk and interfacial capacitance. When programmed in the one-state the bulkpolymer layer is expected to be more conductive because the Al electrode is now injecting electrons into the polymer. This carrier injection causes that the polymer layer is more conductive. The resistance curve on Figure 4.4 (b) agrees with the *I-V* curves discussed above.

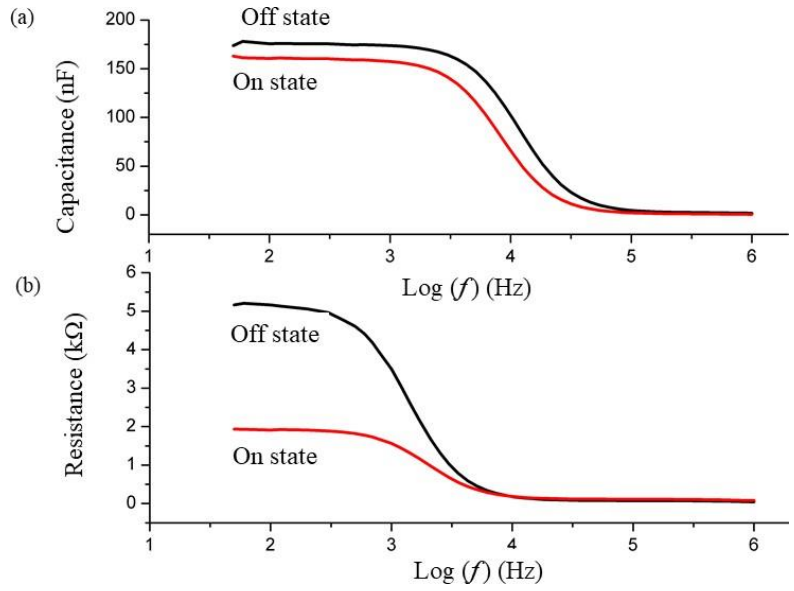


**Figure 4.4** Frequency dependence of the capacitance and resistance for both on- and off-states.

### 4.4.1 Early stages of the electroforming of the LiF/polymer interface.

In previous sections we present the behavior of different device states and how they are programmed, we now proceed to discuss each resistance state individually. We begin by presenting the behavior of the pristine state and how the pristine state is modified (or electroformed) to turn the device into a programmable memory. The early stages of the

electroforming process were monitored using both quasi-static current-voltage characteristics and small-signal impedance techniques.

**(a) Quasi-static current-voltage characteristics**

Figure 4.5 shows an early forming loop while the sample is in the pristine state. The LiF diode behaves initially as a leaky capacitor. This capacitor-like behaviour is clearly seen for negative applied voltages when the current is exclusively the displacement current.

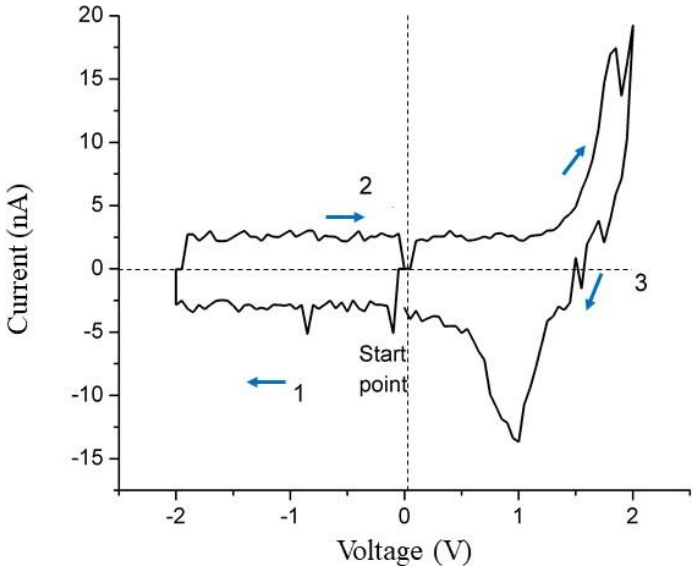


**Figure 4.5**. Current-voltage characteristics (*I*-*V*) of a LiF diode in a pristine state.

Under reverse bias, the *I*-*V* loop in Fig. 4.5 has a symmetric hysteresis behaviour caused by the displacement current ($I=CdV/dt$) where $C$ is the diode capacitance and $dV/dt$ the ramp speed. For positive applied voltages above 1.5 V, the current rises rapidly. The *I*-*V* curve has a non-symmetric behaviour, and the returning path has a discharging negative peak. This behaviour can only be explained if the free charge carriers are injected into the polymer layer and temporally stored into shallow traps. When the electric field begins to be removed (in the return path) the stored charge is released and gives rise to a negative peak on the *I*-*V* characteristic. Since positive applied bias to the Al electrode corresponds to the injection of electrons into the polymer, this means that there is an electron charge density that is injected and temporally stored in the device.

**(b) Hysteresis effects in the *R-V* and *C-V* curves**

Small-signal capacitance (*C*) and resistance (*R*) are usually sensitive to trap filling process and can in principle, reveal the trapping dynamics occurring at the interface. Here we explore the changes on the capacitance-voltage (*C-V*) loops and resistance-voltage loops (*R-V*) caused by a trap filling process. Both *C-V* and *R-V* plots revealed a marked hysteresis behaviour depending on the bias sweep direction and signal test frequency.

Fig. 4.6 shows several *R-V* curves recorded at the test frequency of 200 Hz for increasing voltage range. The first voltage scan is from 0 V until 2 V and the last voltage scan until 4 V. As expected, in the forward voltage scan, the resistance decreases with the applied voltage. However, in the return path an abnormal behaviour is observed. There are three aspects to note. First, in the return path, the resistance is higher than the forward path causing a hysteresis loop. Second, the resistance reaches a maximum and then increases while the voltage decreases, leading to a voltage region with negative differential resistance (NDR). This NDR region can extend over a range as large as 1 V. After passing the NDR region, the *R-V* curve returns to the normal voltage dependence. Third, the end point of the *R*-V curve depends on the maximum voltage reached in forward path. For a constant scanning speed, the higher the applied voltage, the lowest it is the resistance maximum. This observation strongly suggests at the end of the *R-V* hysteresis loop the charge carries have not yet reached equilibrium.

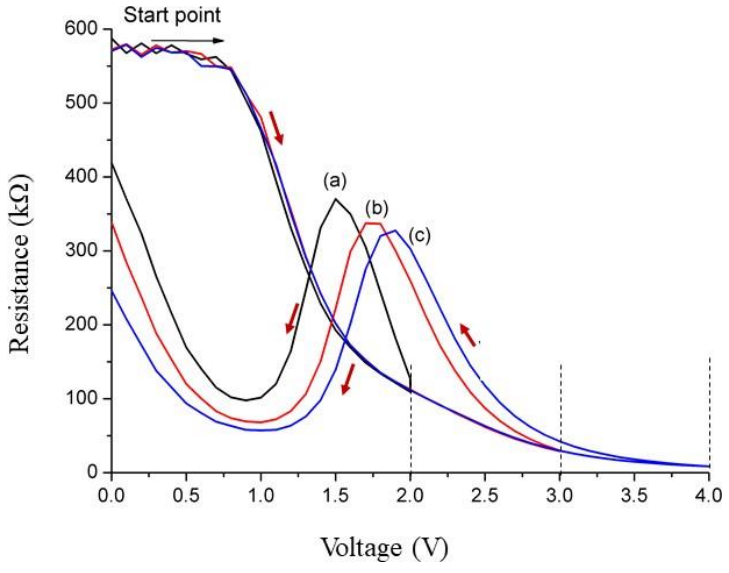


**Figure 4.6.** Small-signal resistance-voltage curves recorded at increasing voltage ranges. The resistance was measured at the frequency of 200 Hz.

To understand why the return path has initially a higher resistance than the forward path, we have to note the small-signal resistance is sensitive to the free carrier concentration on the polymer layer. During the forward scan, we inject free charge carriers which travel across the

polymer layer and get trapped at sites located at the LiF/polymer interface. This transient flow of carriers across the polymer causes a decrease in the polymer resistance. The trapped charge creates an internal field that opposes the external applied voltage. During the forward voltage ramp all the injected electrons get trapped and the corresponding internal field is equal to the external applied field. Therefore, in order to inject more electrons into the polymer, we have to keep increasing the external voltage. During the voltage return path, the trapped charges are not immediately neutralized. This delay between charge filling and charge neutralization causes a difference between the internal and the external voltages. The effective voltage acrossthe device is now a complex an interplay between filling and the trap emptying kinetics. This interplay between the two processes, causes two unusual features on return path of the *R-V* curve; first, in the initial return path the resistance is temporally much higher that under the forward path (the external bias does not inject carriers, and the number of charges released from the traps is low. Second, a NDR region appears. The NDR region is caused by the releaseof trapped charge. This released charge will flow back into the polymer layer increasing the free carrier concentration. Alternatively, trapped electrons are neutralized by a hole current. Onthe grounds of the present experimental evidence the two processes are indistinguishable. Botha hole and an electron current will temporary increase the bulk conductance giving rise to a NDR region. Once the trapped electrons are neutralized, the hole current fades away and the *R-V* curve returns to the normal voltage dependence. Finally, the maximum voltage reached ina *R-V* loop affects the position of the maximum in resistance as well as the value of the resistance in the end point of the hysteresis loop. We propose this behaviour is because the higher the applied voltage, the higher will be the density of trapped electrons.

Capacitance-voltage (*C-V*) curves were also recorded together with their corresponding *R-V* characteristics. The *C-V* curves recorded for increasing voltage ranges are shown in Fig. 4.7.

The hysteresis behaviour observed at low bias in the *C-V* characteristics was recorded by increasing the maximum voltage range. The strategy behind this procedure is to control the density of stored electrons in the film and see the corresponding effects on the capacitance. Figure 4.7 shows three *C-V* plots for three different voltage ranges, loops labelled (a), (b) and (c). The capacitance is flat until 1.3 V. Above 1.3 V the capacitance increases linearly with the voltage (part of the curve labelled (i) on Figure 4.7). If the voltage scan is stopped at 2 V (loop (a)), then in the return path the capacitance stays high and even increases while the voltage is decreasing. This unusual voltage dependence stops at around 1 V. For voltages below 1 V the capacitance returns to the normal voltage dependence. For the subsequent *C-V* loop (b) recorded for higher applied voltage a similar behaviour was recorded. However, the

capacitance shows a plateau for voltages above 2 V. The loop (c) follows a similar behaviour as the previous ones, but for voltages above 3.5 V the capacitance increases dramatically. This sharp increase in capacitance without hysteresis will be discussed later.

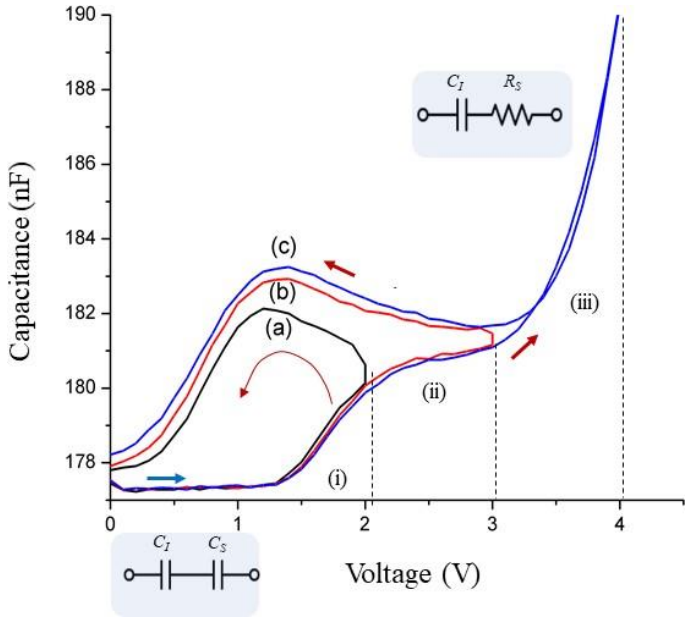


**Figure 4.7.** Small-signal Capacitance-Voltage curves recorded at increasing voltage ranges. The capacitance was measured at the frequency of 200 Hz. The labels (a), (b) and (c) refer to hysteresis loops recording to increasing voltage ranges.

The observation of an anti-clockwise hysteresis both on the *R-V* as well as on the *C-V* curves suggest that the two behaviours must be related. In other words, the NDR region in the *R-V* curve must be related with the abnormal increase in capacitance on the return path of the *C-V* curve. As discussed above, we propose this abnormal hysteresis behaviour is caused by trapping of electrons near the LiF/polymer interface.

We now proceed to explain the abnormal increase in capacitance in the return path of a *C-V* loop. The proposed explanation is supported by the equivalent circuit show as inset on Fig. 4.7. At low applied bias the capacitance is flat, basically the impedance analyser is probing the series sum of the polymer layer capacitance ($C_S$), and LiF layer capacitance ($C_I$). As the external voltage increases electrons are injected into the polymer and they get trapped at the LiF/polymer interface. The corresponding electron current increases the polymer bulk conductance. This increasing in bulk conductance effectively short-circuited the capacitance of the bulk polymer layer. Therefore, the capacitance becomes essentially dominated by the LiF insulating layer. For voltages above 1.2 V the device behaves a Metal-Insulator-Semiconductor

(MIS) diode driven into accumulation. The capacitance plateau corresponds to the LiF layer capacitance. In the voltage return path, the capacitances do not follow the original forward bias path, but over a small voltage range, the capacitance is higher than the one measure in the forward path. In addition, the capacitance keeps increasing as the voltage decreases until a maximum is reached at approximately 1.2 V. After the maximum, the capacitance follows the expected voltage dependence.

Anti-clockwise hysteresis loops in *C-V* plots are unusual. To explain this anomalous behaviour, we have to go back to the hysteresis loop on the *R-V* curve described above. The peak in capacitance occurs at the same voltage where the NDR region in the *R-V* curve occurs. Therefore, it is plausible to assume that both, the abnormal rise in capacitance and the NDR region are caused by the same physical mechanism.

Assuming that the trap neutralization, is due to electrons flowing out of the traps, them the diode current is dominated by a minority carrier current which flows through the polymer by a diffusion process. Diffusion is a rather slow process, and for relatively high frequency diffusion currents cannot follow the voltage changes instantaneously; the current starts lagging the voltage and a shift of the phase of the current relative to the voltage occurs. The increasing phase shift is interpreted by the impedance analyser as an increasing capacitance. Excess capacitance by the presence of diffusion currents have been reported by other authors, se for example the work of Werner J. et al.[173], [174]. It must be noted that this is not a true capacitance in the sense that the device can store charge, this is the definition of static capacitance! but is rather an as-measured capacitance caused by a phase shift between the ac current and the ac voltage.

In summary, we propose, that the abnormal increase in capacitance during the voltage return path is due to a diffusion current that neutralizes the traps. It is important to mention that this effect is responsible for a relatively small rise in capacitance of about 1 nF in a total change of 6 nF.

The abnormal hysteresis loops observed both on the *C-V* and *R-V* plots are a consequence of a transient diffusion current which neutralizes the trapped electrons at the LiF/polymer interface. This transient current temporarily increases the polymer conductivity causing on the *R-V* curve a NDR region and on the *C-V* characteristic an excess capacitance. Figure 4.8 summarizes both the resistance and capacitance behaviour.

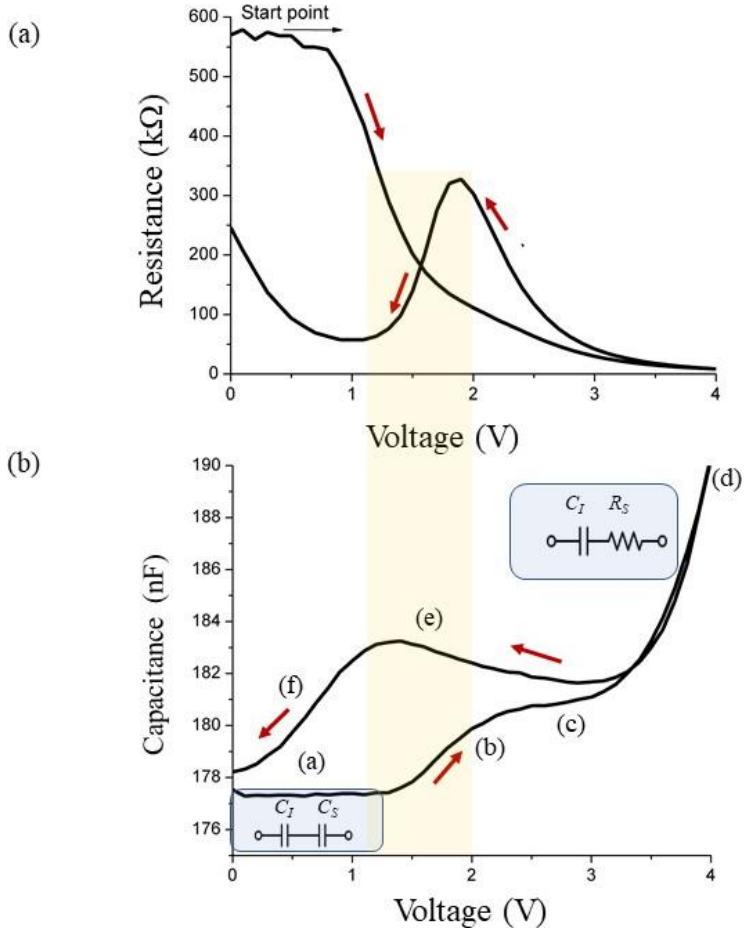


**Figure 4.8** Voltage dependence for capacitance (a) and resistance (b).

The anomalous hysteresis behavior observed both on the *R-V* and *C-V* loops described in detail above is strongly frequency dependent as depicted in Figure 4.9. For frequencies above 600 Hz the anomaly disappears. This strong frequency response of the NDR agrees with the view of a diffusion current. Slow carriers cannot follow the high frequency signal.

In summary, electrons injected into the polymer drift to the insulator-polymer interface and get trapped there. Once the external applied voltage is lowered, which happens once the voltage sweep direction is reversed, electrons start to flow out of the traps and move across the polymer layer by diffusion. The increase in the free carrier concentration temporarily increases the polymer conductance giving rise to a NDR region on the *R-V* curve. Simultaneously, the trap neutralizing diffusion current also causes an excess capacitance as measured by the impedance analyser. This excess capacitance causes an anti-clockwise hysteresis on the *C-V* loop.

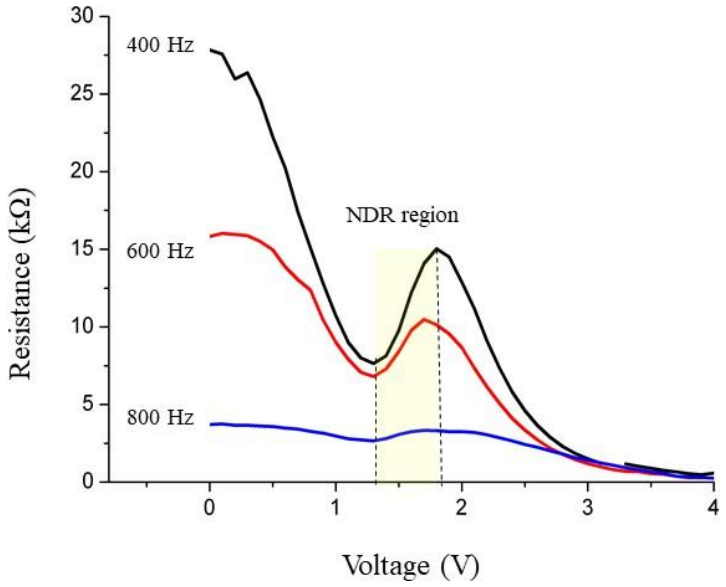


**Figure 4.9**. Resistance versus voltage curves recorded for several frequencies. For the sake of simplicity only the reverse scan is represented.

**(c) Current transients**

In order gain information about the trap filling kinetics current transients were measured as function of the applied voltage. To measure the trap filling kinetics a voltage stepof was applied and the corresponding changes in current were monitored as function of time. Figure 4.10 shows the plot of the current as function of time. The current was monitored for several applied voltages. In a log(*I*) *vs* log(*t*) plot the current follows a linear behaviour with a slope of 1.12. This means that the current follows a power law of the type $I(t)=t_0^{1.12}$ where $t_0$ isa constant.

This power law behavior is typical of a system where traps are progressively filled until the internal filled created by the trapped charges is equal to the external applied voltage.

The rate limiting process for trap filling is proposed to be the dispersive hopping process (electron transport trough the polymer) with a long tailing of hopping time distribution,

The current through the diode can be expressed as

$$I(t) = C\frac{dV(t)}{dt} = \frac{V(t)}{R_{poly}(V(t))} \qquad (4.2)$$

Where *C* is the capacitance of the LiF layer and $R_{poly}$ is the resistance of the polymer layer.

Transport of electrons through conjugated polymers is a trap limited process. This transport is phenomenologically approximate $R_{poly}$ by

$$R_{Poly}(V(t)) = \frac{r}{V(t)^n} \tag{4.3}$$

Where $r$ and $n$ are parameters that dependent on the energy distribution of the traps. For conjugated polymers $n$ usually follows in the range 3 to 7. The differential equation 4.2 for $V(t)$ can be solved by integrating by parts yielding the following expression for the current

$$I(t) = \frac{1}{r}\left(\frac{1}{\frac{n}{RC}t + \left(\frac{1}{V_0}\right)^n}\right)^{1+\frac{1}{n}} \tag{4.4}$$

When $t \gg \left(\frac{-}{nV_0^n}\right)$ we can simplify as:

$$I(t) \text{ a } t^{-(1+\frac{1}{n})} \tag{4.5}$$

Where $Vo$ is the initial voltage drop over the polymer. From the experiment, we obtain a power-law dependence of the current $I$ on time with an exponent 1.12.
From the $J$-$V$ characteristics we obtain and exponent 3. This is in reasonable agreement with the exponent $\alpha$=1.12 from time domains measurements as described by Eq. 4.5.

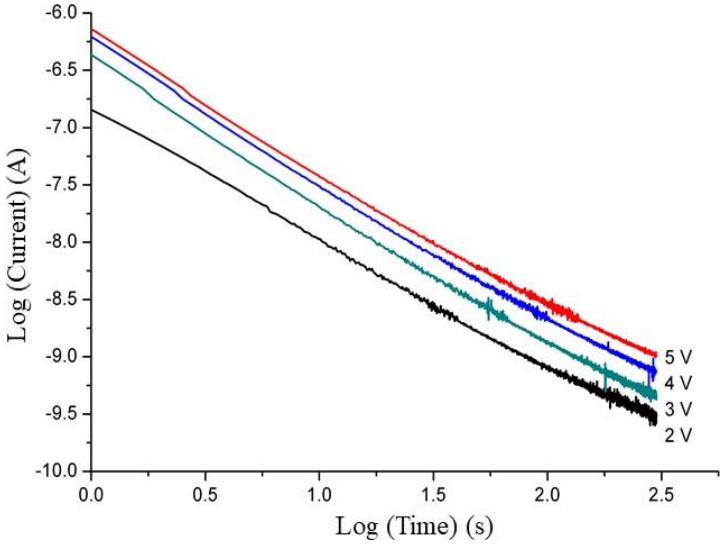


**Figure 4.10.** Transient response of the current during trap filling. The filling was done by the application of a voltage step. Measurements were done in the pristine state.

### 4.4.2 Small-signal impedance of the electroformed device

In the above sections the analysis has been focused on the pristine state. It is important now to proceed and see how the impedance changes upon electroforming. Figure 4.11 compares the *R-V* curves when the sample is electroformed. When the sample is in the pristine state the hysteresis is fully reversible (the starting point is equal to the end point). This is true if the scanning speed is low (20 mV/s). The electroforming was carried out by increasing the voltage up to 8 V (see curve (c) in Figure 4.11). As expected, when the device is electroformed, the final state has a significant lower resistance (1 MΩ) when compared with the pristine state resistance (16 MΩ).

It is interesting to note that the NDR region (in the reverse scan) is still observed even in the electroformed state, but in comparison with the pristine state, the NDR occurs for voltage below 1 V while in the pristine state the NDR was occurring below 2V. The presence of the NDR behavior confirms that the trapped electrons at the LiF/polymer interface are still present in the electroformed device.

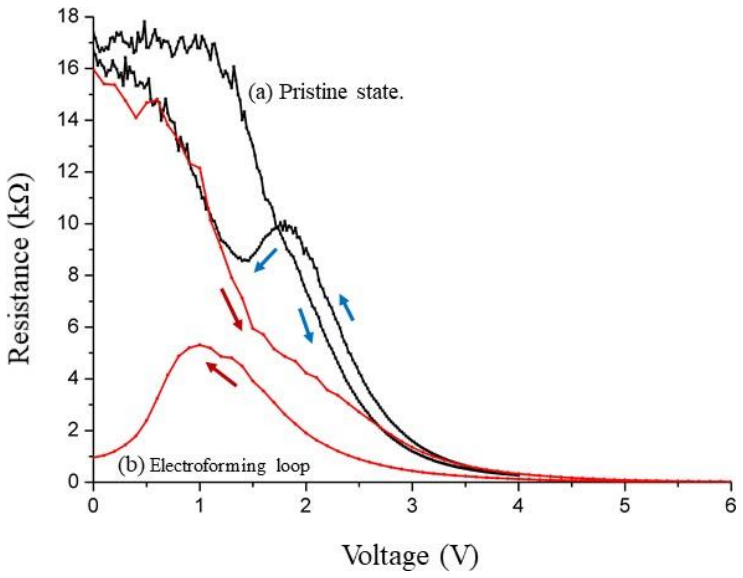


**Figure 4.11**. Voltage dependence of the resistance during the electroforming process. Curve (a) was measured in the pristine state. During the curve (b) the device was electroformed.

Figure 4.12 shows the frequency dependence of the capacitance for different applied voltages. The device still exhibits a Maxwell-Wagner relaxation which is now shifted from 10 kHz (pristine state) above 100 kHz (electroformed state). This shift to high frequencies of the Maxwell-Wagner relaxation is a consequence of a polymer bulk layer much more conductive

owing to the relative high current density now passing through the electroformed device. The electroforming modifies the carrier injection, and the Ba/Al contact becomes an ohmic contact. Apart from the frequency shift on the impedance curve, the major difference between the pristine and the electroformed device is the existence of a pronounced low frequency capacitance tail that increases dramatically with the applied voltage. This low-frequency rise in capacitance can be interpreted in terms of filling of shallow states at the LiF/polymer interface. As the forward bias increases there is a significant population of shallow trap states filled by electrons. The electrons occupying these shallow states contribute to the capacitance at low frequency. At low bias voltages the injected electrons exclusively occupy relatively deep trap states at the LiF/polymer interface and do not contribute to the capacitance at intermediate frequency.

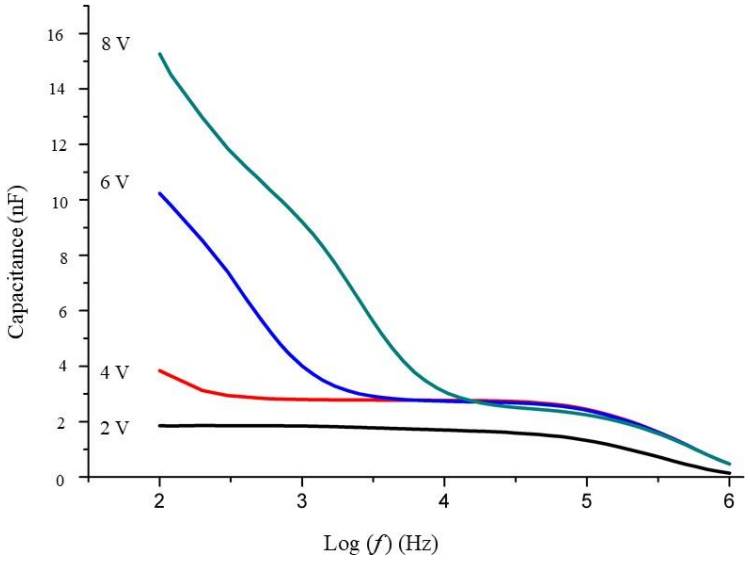


**Figure 4.12.** Frequency dependence of the capacitance for different applied voltages for the electroformed LiF sample.

The frequency dependence of the resistance for different applied bias is represented in Figure 4.13. For low applied bias the resistance is strongly frequency dependent and becomes frequency independent for high-applied bias. We propose this behavior is caused by the very high carrier injection at high bias. At low applied bias the shallow states and still filled and emptied by the ac signal. When the frequency increases less, and fewer states are able to respond to the ac signal causing a pronounced resistance drop with increasing frequency. This frequency dependence will be swapped by the very high carrier injection at high bias. The free carrier density trough the diode is now so high that it dominates the diode resistance and prevents the observation of the observation of shallow states. In other words, the filling and

empty of shallow states that is responsible for the low-frequency dependence of the resistance is now swamped by high dc current.

The electroformed sample exhibits electrical fluctuations which resemble to noise. Interestingly, the magnitude of the electrical fluctuations is higher in the high resistance state. Figure 4.14 shows the changes in the electrical noise as a function of the voltage.

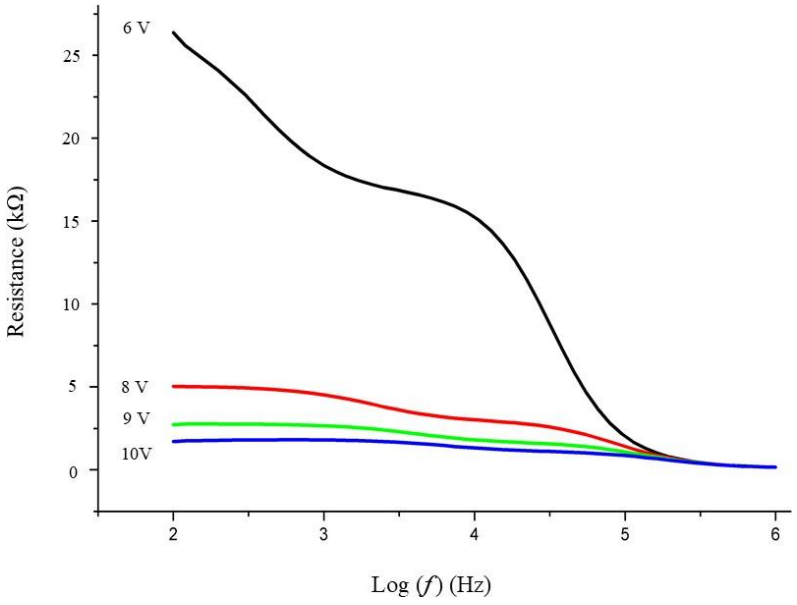


**Figure 4.13.** Frequency dependence of the resistance for different applied voltages for the electroformed LiF sample.

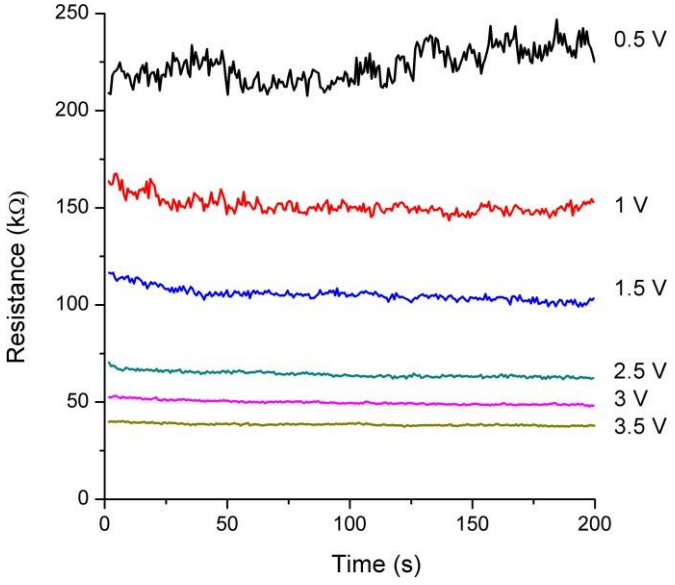


**Figure 4.14.** Transient measurements with different bias voltage. Results were recorded on electroformed device.

## 4.5. Discussion

In this chapter we analysed in detail the changes occurring at the LiF/ polymer interface upon electroforming. These use of the small signal impedance measurements in the pristine state revels that electrons are stored (trapped) at the LiF/polymer interface. The stored charges build up an internal field. Once the external voltage is removed the stored charge does not come out immediately. This delay between filling and emptying of the traps leads to a peculiar behavior of the resistance and capacitance as function of the bias sweep direction. During a forward voltage scan the external voltage injects electrons increasing the free carrier density in the polymer bulk region. The trapping current is a temporary effect, and eventually will stop when the field due to the stored electrons becomes equal to the external applied field. In the reverse voltage scan a complex dynamic occurs. The external voltage decreases, but the stored electrons do not come out immediately, therefore, the internal field will become higher than the external applied voltage. The interplay between the internal and external voltage is controlled by the rate of decrease of the external voltage and by the emptying kinetics of the electrons out of the shallow states. For a certain voltage range the detrapping current can still increase while the external voltage is lowering, this gives rise to a NDR region on the *R-V* curve.

This NDR region observed on the resistance *vs* voltage curves is clear evidence for the presence of trapped electrons. This stored charge will be responsible for the soft-dielectric breakdown and resistive switching memory properties.

Transient current measurements upon a step voltage excitation reveal that the trap filling kinetics is controlled by the slow hopping charge transport mechanism across the polymer bulk layer.

Small signal impedance measurements after electroforming show that the shallow states are still present and trapping substantial amount of charges at the LiF/polymer interface. Therefore, these interfacial traps do not only play a role in the electroforming but also have an active role in the switching behavior of the memory. Based on the frequency and bias dependence of the impedance we can conclude these traps have a broad distribution in energy.

## 4.6. Conclusions

In summary, this chapter reports a detailed investigation of the different electrical states of the memory device, namely, the pristine, the off-state and on-state. It is concluded that when the device is in the pristine state, the current flowing through the device upon the application of an external bias is a transient trapping current. Once the field is removed the trap emptying process generates a current of opposite sign which causes a NDR region on the *R-V* curves and an excess capacitance on the *C-V* curves. The excess capacitance is not a static capacitance but a small-signal capacitance. The slow diffusing out of electrons out of the device causes the phase angle between voltage and current, which is interpreted by the impedance analyser as an additional capacitance.

Trapping of electrons at the LiF is still occurring even after the diode is electroformed. Evidence for these traps is provided by the frequency and voltage dependence of the capacitance and resistance. Therefore, it is proposed that the interfacial LiF/polymer interfacial traps play an important role not only in causing the soft-dielectric breakdown of the LiF (electroforming) but also in the switching properties of the electroformed diode.

# Chapter 5

## *Synthesis of CdS nanocrystals in a gelatin matrix: The effect of the pH on the size of nanoparticles*

Cadmium sulfide nanocrystals were synthesized via a sol-gel process within a gelatin solution. This chapter outlines how pH manipulation governs the size of these CdS nanocrystals. As the pH of the solution decreases from 10 to 6, the nanocrystal radius concomitantly diminishes from 8 to 3.5 nm. To understand these synthesized CdS nanoparticles, we conducted thorough characterizations involving optical absorption and photoluminescence studies. These investigations yielded valuable insights into the optical properties of these nanocrystals.

This work has been published by V. I. Boshernitsan, V. A. Smyntyna, V. M. Skobeeva, and N. V. Malushin, "Synthesis of CdS nanocrystals in the gelatin matrix with different pH values and their optical properties," *Physics and chemistry of solid sate"*, vol. 16, no. 4, pp. 692-694.

doi: 10.15330/pcss.16.4.692-694. [175]

## 5.1. Introduction

Semiconductor nanocrystals (NCs) are used in a broad range of applications including solar cells, nanoelectronics, optics, molecular, cellular biology, and in medical diagnosis [131], [176]. One interesting feature of nanocrystals in the polymer matrix is their high chemical surface activity. This is a thorough consideration of the interfacial electronic and physicochemical processes that transpire at the boundary between the nanocrystal and the hosting matrix. These interactions impact the optical and luminescent properties under the influence of various external factors (temperature, type of stabilizer, concentration of the initial components and ratios, pH, etc.) [19].

The primary aim of this chapter is to describe the synthesis of CdS nanocrystals within a gelatin matrix. We systematically investigate the influence of solution pH on the average nanocrystal size, elucidating the underlying mechanisms behind this phenomenon.

## 5.2. Experimental

Nanocrystals of cadmium sulfide that were obtained by the sol - gel technology from solutions of salts cadmium (cadmium nitrate) and sulfur (sulphide sulfur) in the colloidal solution of gelatin [99], [159]. The formation of CdS nanoparticles is a result of the following exchange reaction:

$$Cd(NO_3)_2 + Na_2S \Longrightarrow CdS + 2NaNO_3.$$

The pH of the solutions was varied by adding an alkaline solution or hydrochloric acid to the solution. The color of the solutions ranges from light yellow (at pH = 6) to dark yellow (at pH = 10). Once completion of the synthesis of the nanocrystals is complete, the solution with suspended CdS nanocrystals, was sprayed on a glass substrate and left dried for several days to hardening the gelatin gel.

Average radius ($r$) of cadmium sulfide nanocrystals was evaluated from the optical absorption spectra and by using the relations for the threshold energy of interband absorption. According to the theory of interband absorption, in the absorption spectrum should be observed series of discrete lines. The absorption threshold, that means, the energy of the first optical transition, is called the effective band gap of the nanocrystal ($h\omega_{01}$) and it is provided by Eq. 5.1.

$$h\omega_{01} = E_g + \frac{\hbar^2 \pi^2}{2\mu r^2} \qquad (5.1)$$

Where μ is given by

$$\mu = \frac{m_e m_n}{m_e + m_n} \qquad (5.2)$$

*Eg* is the optical band gap of bulk crystal, $m_e$ and $m_n$ are electron and hole effective mass respectively, *r* average radius of the nanoparticle and ħ the Planck constant. According to Eq. 5.1, it becomes evident that the effective width of the band gap increases as the size of the particles decreases.

Optical absorption spectra were recorded using an SF-26 spectrophotometer within the wavelength range spanning from 320 nm to 600 nm. To mitigate potential errors stemming from light scattering, particularly in the shorter wavelength range (320-360 nm), we employed a USF-2 filter to selectively truncate the visible spectrum. Measurement error did not exceed ± 1%. Luminescence was excited by pulse laser (LCS-DTL-374QT) with a wavelength 355 nm excitation of light. The maximum laser power used was 35 mW.

## 5.3. Results and Discussion

CdS nanocrystals in gelatin solution with different pH values were studied using optical absorption and luminescence techniques. The effect of storage time in air on the optical properties was also explored. The absorption spectra of CdS nanocrystals in gelatin solution with increasing values of pH, from 6 to 10 are shown in Figure 5.1. A noticeable shift of the absorption edge towards higher energy compared to the band gap of single crystal of cadmium sulfide band gap ($E_g$ = 2.5 eV) is observed.

The average size of nanocrystals was determined using the energy data of the first optical transition. The values of the effective widths of the nanocrystal forbidden zones were obtained by extrapolating the straight line in the absorption curves (Fig. 5.1) to the wavelength axis and calculated using the equation for diameter of nanocrystals of the group $A_2B_6$ [177].

As the pH value decreases from 10 to 6, significant reduction in the average size (radius) of the synthesized nanocrystals, diminishing from 8 to 3.5 nm. This pH-dependent behavior in CdS nanocrystals' absorption spectra can be elucidated by considering the reactions taking place during synthesis. It is primarily based on the hydrolysis of cadmium salts and sulfur, where the distribution of hydrolysis products is pH-sensitive. Specifically, at a pH below 6, the solution becomes enriched with cadmium ions ($Cd^{2+}$) while containing fewer hydrogen sulfide ions ($HS^-$), consequently limiting the availability of hydrogen sulfide ions and leading to smaller nanocrystal sizes. In the pH range between 7 and 8, cadmium ions and hydrogen sulfide ions are roughly balanced, resulting in an increase in nanocrystal size. For a pH above 8, the concentration of cadmium ions decreases, but the presence of hydroxide cadmium ions ($CdOH^-$) and hydrogen sulfide ions ($HS^-$) increases, facilitating further nanocrystal growth. This model is confirmed by the changes in the absorption spectra depicted in Figure 5.1.

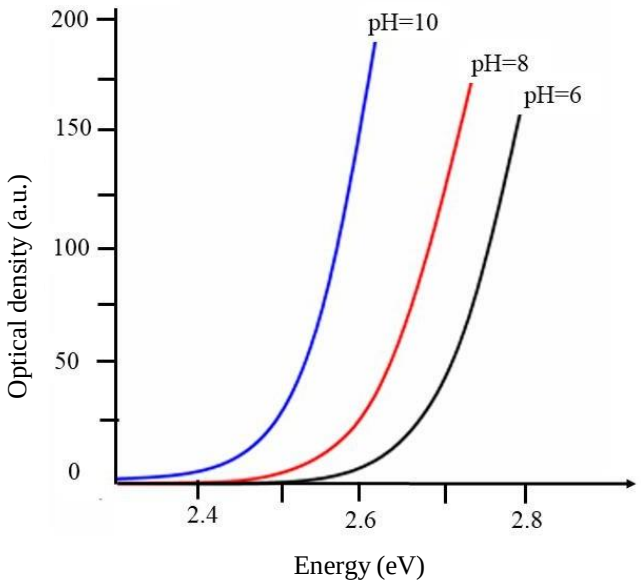


**Figure 5.1**. The optical density spectra of CdS nanocrystals as a function on the pH of the gelatin solution.

This study also investigates how the molar composition of the solution affects the emission spectrum of CdS nanocrystals, which emit light within the visible spectrum. The luminescent behavior of CdS nanocrystals is attributed to band-to-band or exciton recombination, with contributions from defects found in the bulk material and on the crystal surface. These defects primarily manifest as vacancies in the cadmium and sulfur ions. Altering

the sulfur and cadmium ion content in the solution can result in an excess of these ions, influencing the luminescent properties.

Figure 5.2 shows the luminescence spectra of colloidal solutions containing nanocrystals synthesized at varying pH values, ranging from 6 up to 10. The predominant feature in this spectrum is a broad luminescence band with its peak centered around 600 nm. Remarkably, the contour of this luminescence band undergoes significant changes in response to alterations in the solution's pH. Specifically, as the pH level increases, there is a pronounced decrease in luminescence, accompanied by a subtle shift towards longer wavelengths. This phenomenon suggests a variation in the concentration of defects responsible for radiative (emitting) recombination. This finding agrees with the results of luminescent in nanostructure CdS with ZnS shells reported in reference [159]. Authors of this paper noted that the luminescence spectrum of samples obtained at lower pH values exhibited a discernible shift towards higher wavelengths. In contrast, samples prepared at pH> 8 displayed a broader luminescence spectrum that extended into shorter wavelengths.

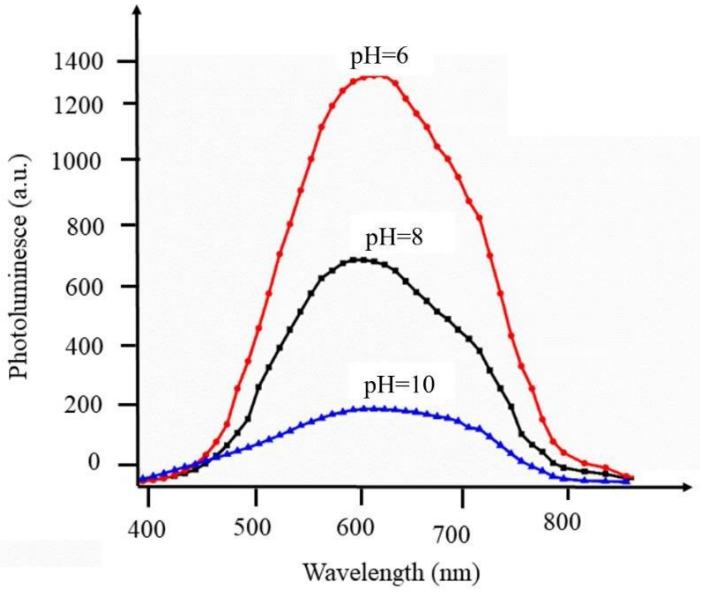


**Figure 5.2**. The photoluminescence spectra of CdS nanocrystals, obtained in solutions with different pH values.

On the basis of the data presented above, we can deduce that alterations in the acidic/alkaline balance induce the formation of nanocrystals with varying sizes and differing stoichiometries of atoms on their surfaces. In acidic environments nanocrystals with an excess of cadmium on the surface will be formed, whereas in alkali environments those with an excess of sulfur become prevalent. Furthermore, for pH> 8 hydrolysis produces cadmium hydroxide, resulting in its increased concentration with rising pH. Concurrently, an increase in pH leads to higher sulfur concentrations both in the solution and on the nanocrystal surfaces, concomitant with a reduction in luminescence intensity. This observation suggests that the presence of sulfur in the nanocrystals suppresses the luminescence of cadmium sulfide and for the long-wavelength luminescence can be responsible for the presence of sulfur vacancies [178].

To discern the constituents of the long-wavelength luminescence, we performed curve fitting on the experimental data using Gaussian curves. The maxima positions of the luminescence bands' components are presented in Table 5.1. Interestingly, at pH values of 6 and 8, we observed two luminescence bands in the colloidal solutions. However, in samples with a pH of 10, three distinct luminescence bands emerged. An additional short-wavelength band, with a wavelength of $\lambda = 470$ nm, was observed at pH of 10, positioned at the edge of the absorption spectrum.

The presence of edge luminescence in CdS nanocrystals is typically observed in samples with surface modifications. Furthermore, as indicated in the literature, this surface modification can be facilitated under specific synthesis conditions attributed to the formation of a cadmium hydroxide shell [176]. An increase in the alkalinity of the solution, particularly at pH> 8, promotes the development of this shell and the potential precipitation of the compound onto the nanocrystal surfaces. This shell effectively passivates surface states. We can corroborate this hypothesis regarding the nature of the long component by examining the intensity ratio of the component bands, denoted as $I_{\lambda 2}/I_{\lambda 3}$ (refer to Table 5.1), which decreases with increasing alkalinity.

**Table 5.1**. Dependence of the position of calculated maximum of luminescence of CdS nanocrystals on the pH values of solution

| **pH** | **$\lambda_1$ (nm)** | **$\lambda_2$ (nm)** | **$\lambda_3$ (nm)** | **I $\lambda_2$/I $\lambda_3$** |
|---|---|---|---|---|
| 6 | - | 593 | 701 | 1.7 |
| 8 | - | 590 | 700 | 1.83 |
| 10 | 470 | 608 | 711 | 2.74 |

## 5.4. Conclusions

The following conclusions can be drawn from the investigation into the impact of pH on the size of the synthesized CdS nanoparticles:

- CdS Nanocrystals were successfully produced using the method of colloidal chemistry employing gelatin as a stabilizer;
- The solution's pH has a direct influence on the nanocrystal size, namely a decrease in average size of the nanocrystals from 8 to 3.5 nm with decreasing pH from 10 to 6;
- The variations in nanocrystal size stem from alterations in the acid-base balance, brought about by the hydrolysis of the salt components during synthesis.
- . The luminescence in the long wavelength region of the spectrum can be attributed to defects present on the surface of the CdS nanocrystals, specifically sulfur vacancies.

# Chapter 6

## *Establishment of formation mechanisms for optical properties of colloidal solutions and nanofilms of CdS*

In this chapter the optical properties of CdS nanoparticles which exhibit the quantum-size effects are presented and discussed. The photoluminescence of CdS nanocrystals in different host matrices is also reported.

This work was published by V. Smyntyna, V. Boshernitsan, V. Skobeeva, “The influence of inter-phase physical and chemical processes on the optical properties of CdS nanocrystals in gelatin,” Electronics and information technologies. Issue no. 2, pp. 51–56, 2012. ISSN 2224-087X. [179]

## 6.1. The influence of inter-phase physical and chemical processes on the optical properties of CdS nanocrystals in gelatin

### 6.1.1. Experimental results and discussion

Nanocrystals of CdS were obtained by using the method described in Chapter 5. After the synthesis process, the colloidal solutions of nanocrystals were diluted with distillation water in a ratio of 1:1 and 1:3. For undiluted solutions, the concentration of gelatin was 5%, for diluted in the ratio 1:1 and 1: 3 - 2.5 and 1.7%, respectively.

The optical absorption spectra of colloidal solutions were investigated. In Figure 6.1 are shown normalized absorption spectra of CdS nanocrystals at different gelatin concentrations, 5% (curve 1), 2.5% (curve 2), 1.7 % (curve 3). As it seen, with a decrease of gelatin concentration, particle size decreases. This is evidenced by the shift of the absorption edge toward higher energies with reduced the concentration of gelatin in the colloidal solution. It was noted that the absorption edge of all the spectra is located in the interval energies greater than the band gap of the bulk single crystalline cadmium sulfide (Eg = 2.5 eV), which is one of the manifestations of quantum-dimensional effects in synthesized nanocrystals.

It was revealed the effect of reducing the average size of nanocrystals with a decrease in the concentration of gelatin in colloidal solution, which is the result of dissolution of nanocrystals due to the decrease in the stabilizing properties of gelatin (see Table 6.1).

The average radius of nanocrystals of cadmium sulfide, *r,* were estimated from optical absorption spectra using expressions of threshold energy interband absorption that has meaning of "effective" energy gap of nanocrystal *Eg* and energy of size quantization electrons and holes in the valence band and the conduction band.

It has also been found that the physicochemical properties of colloidal solutions of CdS nanocrystals change over time. Absorption spectra showed an increase in the absorption capacity of nanocrystals when stored for one month in ambient air.

When colloidal solutions of CdS nanocrystals are stored in ambient air over long periods of time (several weeks) a phenomenon named "focusing of their sizes" occurs. This phenomenon means that the particle size distribution gets narrow. The narrowing of the particle size distribution upon storage time, is observed for all colloidal solutions of CdS nanoparticles obtained in gelatin matrix. These findings correlate with the luminescent studies data. The luminescence spectra of CdS nanocrystals obtained at different gelatin concentrations are shown in Figure 6.2. The concentration of gelatin in colloidal solutions was 5% (curve 1), 2.5% (curve 2) and 1.7% (curve 3).

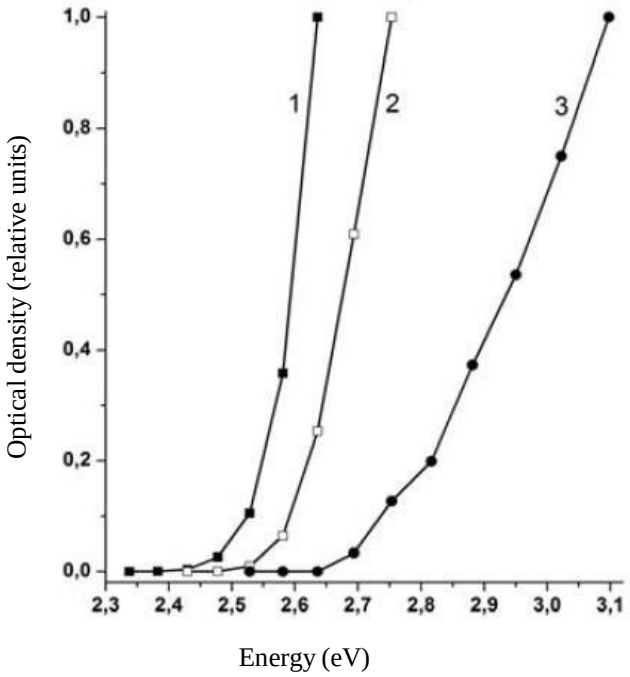


**Figure 6.1.** Normalized absorption spectra of CdS nanocrystals at different concentrations of gelatin concentrations, (1) 5%, (2) 2.5%, and (3) 1.7 %.

**Table 6.1**. The effect of the concentration of aqueous gelatin solution on the size of CdS nanoparticles.

| **Gelatin concentration (%)** | ***Eg*** **(eV)** | ***r*** **(nm)** |
|---|---|---|
| **5.0** | 2.52 | 11.0 |
| **2.5** | 2.58 | 5.5 |
| **1.7** | 2.71 | 3.4 |

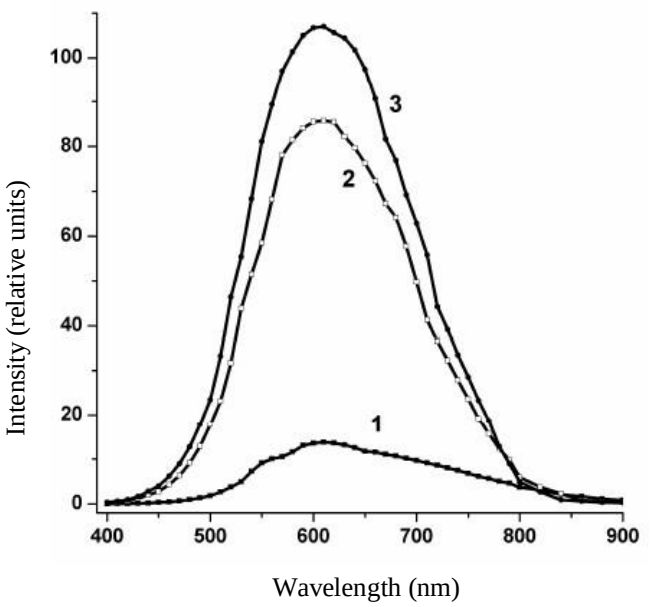


**Figure 6.2.** Photoluminescence spectra of CdS nanocrystals
at different gelatin concentrations, %: 5% curve 1, 2.5% curve 2, 1.7% curve 3.

In all samples, prevails a luminescence band centered approximately at a wavelength $\lambda_{max}$ = 610 nm. The width of the luminescence band decreases with increasing gelatin concentration. This behaviour indicates that the particle size distribution gets narrow, meaning that there is also a “focus on size”. The intensity of the luminescence band maximum increases with the increase in the bulk density of the nanoparticles in the samples, indicating an increase in the number of particles in solution, in particular medium sized particles (their contribution to luminescence is the highest).

In summary, quantum-size effects were observed in CdS nanocrystals obtained by the method of colloidal chemistry in aqueous gelatine solution. Nanoparticle size formation depends on the properties of the stabilizer (gelatin matrix). When the concentration of the stabilizer decreases, the particle size decreases. In the case of long-term storage of colloidal solutions of CdS nanocrystals occurs a phenomena called "Size focusing". An increase in the absorption capacity of nanocrystals is observed and the luminescence intensity increases.

## 6.2. Luminescent properties of CdS nanocrystals in different host matrices

Additional experimental data about CdS nanoparticles embedded in different polymer host matrices is provided here. Furthermore, measurements of photoluminescence, excitation and emission spectra are also presented and discussed.

### 6.2.1. Experimental details

Several insulating polymers were used as host matrices for the CdS nanocrystals, namely, photographic gelatin, polyvinylpyrrolidone (PVP), polystyrene sulfonate (PSSNa) and a solvent dimethylformamide (DMF). The pH value of the solutions varied between 4 and 5. Measurements were carried out, both in liquid solutions as well as in thin films of nanoparticles deposited on glass substrates. After completion of the synthesis process, the solution which contained suspended in polymer nanoparticles of CdS was sprayed on glass substrates and left dried during for 24 hours at room temperature. From the absorption spectra were determined the size of nanoparticles. In the matrix of photographic gelatin nanoparticles had dimensions (average radius) from 5 to 10 nm, depending on pH (such dependence was explained earlier in Chapter 5). In polyvinylpyrrolidone (PVP) matrix nanoparticles of CdS had a diameter $D$=8.2 nm ($r$=4.1 nm), and in polystyrene sulfonate (PSSNa) D=7,5 nm.

Photoluminescence (PL) spectra were recorded using a LCSDTL-374QT pulsed laser (excitation at 370 nm, pulsing at 700 kHz). Luminescence was excited by the solid-state samples pulsed laser with the following specifications: maximum average power of 5 mW, pulse duration at 1 kHz ~ 1 ns, pulse energy at 1 kHz ~ 20 μJ, the emission wavelength of 355 nm. The luminescence was registered with the detector PMT-106, which has a maximum spectral sensitivity in the range of 400-440 nm. Emission was recorded with the FEU-100 photoelectron multiplier. The IR PL signal was studied with the MDR-6 monochromator and recorded with the IR photoresist. The luminescence signal was excited using light-emitting diodes (Edison Opto Corporation), with maxima of emission at 375, 400, 460, 550, and 640 nm, and an ILGI-503 pulsed nitrogen laser emitting at a wavelength of 331.7 nm.

The PL decay profiles of CdS nanoparticles have been investigated, it was used LED laser (excitation - 370 nm), pulsing laser (700 kHz) and femtolaser. Figure 6.3 illustrates the sample of CdS nanoparticles imbedded in gelatin matrix. During the measurements, the liquid solution was inside of the glass cuvette as shown on the figure 6.3 (a). Figure 6.3 (b) shows the PL of thin film of nanoparticles deposited on the glass substrate.

For the absorption spectra a solution of pure gelatin was used as a reference (see Figure 6.4). This sample has no color, it is transparent. Figure 6.5 illustrates the samples of thin films of CdS nanoparticles in gelatin matrix with different pH values. It is visible the difference in colors of the films depending on the pH of initial solution that was deposited on the glass substrates. All samples were transparent.

a) b)

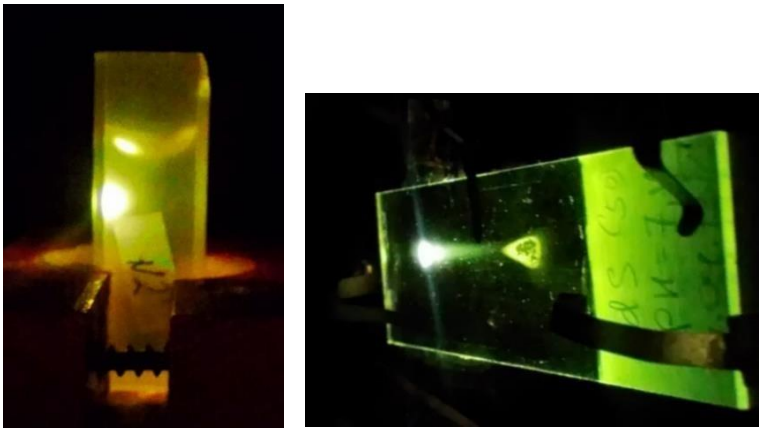

**Figure 6.3**. Samples of CdS nanoparticles in gelatin matrix during PL measurements. Liquid solution in the cuvette (a) and thin film on the glass substrate (b).

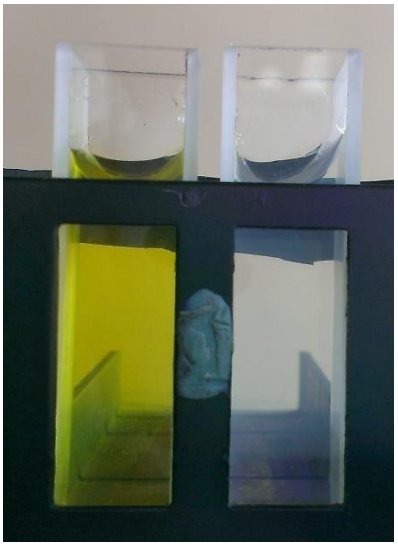

**Figure 6.4**. Samples in cuvettes with solutions contained CdS nanoparticles in gelatin matrix (yellow) and pure gelatin (transparent).

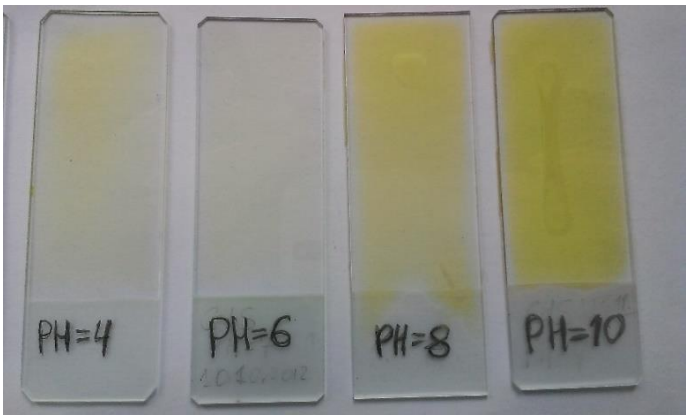


**Figure 6.5.** Samples of thin films of CdS nanoparticles in gelatin matrix with different pH values.

In the following Chapter 6.2.2, experimental results about photoluminescence spectra will be discussed (Figure 6.6) both in liquid samples and in films of CdS were measured using fluorimeter. In the table 6.2 showed excitation and emission wavelength values for each sample of solutions of CdS in different matrices. Also, in table are performed PL and PLE of films CdS in gelatin matrix with different pH values.

### 6.2.2. Photoluminescence of composite structures based on CdS nanocrystals

One of the features of crystals having a nanoscale range and isolated in a polymer matrix is the essential chemical activity of its surface. Therefore, experimental studies of nanosystems with nanocrystal matrix between the phase boundaries and the study of processesoccurring on this boundary are relevant. Heterogeneous systems contain nanocomposites and nanostructures created by nano-objects with different optical characteristics. Properties of suchnanostructures are due to the presence of heterogeneities, boundaries, which lead to complex interactions of the electromagnetic field with structural elements. Particular importance is the study of complex hybrid systems, consisting of semiconductor quantum dots (QD) and biologically active molecules [180].

Several studies of the properties of nanocrystals (NCs) suggest that due to the small size of particles strong effects caused by surface defects are expected namely on the charge recombination processes that occur with the participation of surface defects [14]. This will be

especially evident in the luminescent characteristics of nanocrystals. Our goal is to determine the dependence of luminescent properties of nanocrystals of cadmium sulfide from the type of matrix they are incorporated.

The technology we used to obtain CdS nanocrystals is the method of chemical synthesis from solutions of cadmium and sulfur salts in an aqueous solution of photographic gelatin, dimethylformamide (DMF), polyvinylpyrrolidone (PVP) or polystyrene sulfonate (PSSNa). This method was described in the Chapter 3 of current thesis. Such method allows to grow nanocrystals with an average radius in the range from 1.5 up to 5–6 nm. In such crystals, the ratio of the surface area of the nanocrystal to its volume varies significantly with size, which means that the number of uncompensated valences of atoms reaching the surface of the nanocrystals differs significantly. In addition, when comparing small nanocrystals to large nanocrystals, the surface defect may also increase due to environmental influences, for example, through interaction with the surrounding polymer molecules.

The experiments showed that the luminescence of nanocrystal samples embedded into different host polymer matrices, has different optical properties. Figure 6.6 shows the PL spectra of samples prepared using different host matrices. According to the data depicted in Figure 6.6, the radiation intensity increases with increasing optical power. However, regardless of its value, nanocrystals have one wide band with a maximum at $\lambda_{max}$ = 500 nm. The nature of this band might be associated with deep centers of radiation and is found in nanocrystals with a high concentration of defects, including surface ones. Such luminescence is called "defective" - a term that is broad used in international works on luminescent studies of nanocrystals in the case of indication of the nature of the radiation bands in nanocrystals [9]. Note that the localization of the maxima of the luminescence bands at deep centers depends on the nature of the defects, ie. on the energy of their ionization. According to our observations, and other works in the literature, the long-wavelength region of the spectrum on cadmium sulfide nanocrystals reveals three luminescence bands, which are localized at $\lambda_{max}$ = 580, 670 and 750 nm and whose appearance depends on various factors (technology, experimental conditions, etc.) [143]. The contour of the integral band of the glow of the nanocrystal is formed from their total contribution.

Characteristically, in some samples do not observe zone-band, or exciton luminescent which is a sign of the dominant role of surface defective luminescence, rather than volume properties. Instead, in the spectra along with long-wavelength radiation, a short-wavelength intense narrow luminescence band with $\lambda_{max}$ = 480 nm is observed, the nature of which is

determined by band-band, or exciton, luminescence. The presence of such a band indicates a competitive advantage of the recombination channel associated with recombination in the volume of cadmium sulfide nanocrystals over the surface recombination, as it was previously confirmed in ref. [181]. The dependence of the intensity and contour of the defective luminescence on the radiation power attracts attention. First, the glow intensity of all bands initially increases with increasing luminescence excitation power. Secondly, the ratio of bands forming the total contour of defective luminescence changes with changing power. Due to this fact, it is possible to observe glow bands in the long-wavelength region of the integrated spectrum.

Experimental data of photoluminescence excitation and emission spectrum are shown in Table 6.2. Performed measurements were done for films of CdS in gelatin matrix with different pH values and solutions of CdS in different host matrices.

The nature of this luminescence can be attributed to exciton or edge luminescence. At high pH, the long- wavelength band localized at a wavelength of 700 nm dominates, the nature of which is associated with intrinsic defects in nanocrystals [142]. Samples containing a short-wavelength emission band $\lambda max$ = 470 nm until 498 nm, have an excess of cadmium and thus its nature can be associated with interstitial cadmium and the nature of the long-wavelength band (716-754 nm) should be associated with cadmium vacancies. In the photoluminescence spectra of nanocrystals obtained at values pH $\geq$ 7 the luminescence in the region of 630 nm is recorded. According to the results, this band may be due to an associative defect associated with cadmium and sulphur vacancies.

The fact of the dependence of the circuit on the power of radiation excitation is explained by various parameters of the centers of luminescence, it can be the subject of further research, as well as the nature of the individual components of the luminescence band. Some of the electrons might be captured by traps on the surface of the particle, and due to the excess of the positive charge inside the nanoparticle, an electric field arises, which causes a sharply inhomogeneous distribution of positive and negative charges. It is shown that such a consistent consideration leads to a noticeable difference between the results obtained earlier by approximate methods. Along with the case when the statistical description of conduction electrons in a nanoparticle is valid, low electron concentrations and one-electron quantum states are also considered.

**Table 6.2.** Photoluminescence of CdS nanocrystals in gelatin and in different host matrices.

| | | |
|---|---|---|
| Films of CdS in gelatin matrix | | |
| PL | pH=4 | Excitation: 330, 335, 365 nm |
| | pH=6 | 365, 380, 400, 420 nm |
| | pH=8 | 333, 365, 380, 400 nm |
| PLE | pH=4 | Emission: 425 nm |
| | pH=6 | 565nm |
| | pH=8 | 400, 425, 440, 450, 565 nm |
| Solutions of CdS in different matrices | | |
| PL | DMF | Excitation: 365, 380nm |
| | PVP | 365, 380, 400, 420 nm |
| | | |
| PLE | DMF | Emission: 435, 450, 475 nm |
| | PSS | 470, 650, 660 nm |
| | PVP | 480, 500, 530, 550 nm |

Results of the investigations showed that CdS nanocrystals, grown in different polymeric matrices have intrinsic defects, which cause their luminescence in green and red regions of the spectrum [145]. The chemical nature of defects, responsible for these bands is identical to analogous luminescence centers in monocrystals. At the same time matrix significantly influences on intensity of luminescence. This influence can have different mechanisms. Probably, the most simple can be the mechanism of reabsorption for light quanta at luminescence of matrix by semiconductor nanocrystals.

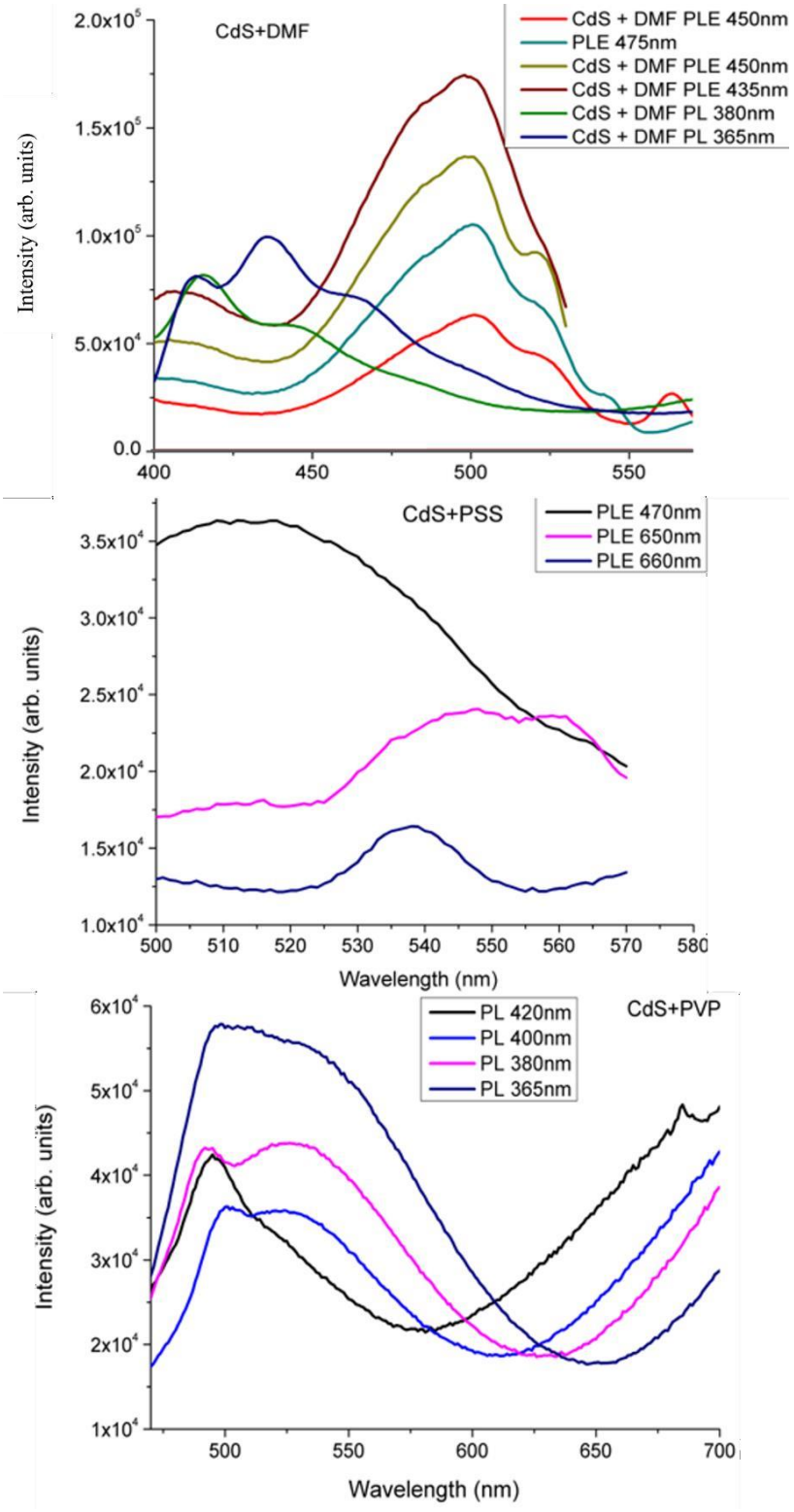


**Figure 6.6.** Examples of measurement results for PL and PLE of solutions of CdS in different host matrices.

## 6.3. Conclusions

In this chapter the physical and chemical properties of CdS nanoparticles were studied. The samples were obtained by the method of colloidal chemistry in aqueous gelatin solution. The findings show that the nanoparticle size depends on the properties of the stabilizer (gelatin host matrix). Upon decreasing concentration of the stabilizer, the particle size decreases. Long-term storage (several weeks) of colloidal solutions of CdS nanocrystals in ambient leads also to a narrowing of the particle size distribution, which we name here "size focusing". An increase in the absorption capacity of nanocrystals is observed and the luminescence intensity increases. Quantum-size effects were observed.

The experimental data presented in this chapter shows a significant effect of interphase surface processes on the absorption and luminescence. Photoluminescence studies showed that the change in the average radius of cadmium sulfide nanocrystals from 3.4 nm to 11 nm significantly affects the spectrum of their radiation, namely, due to the larger ratio of surface to volume in nanocrystals of smaller size, do not observe zone-zone, or exciton, luminescence. In larger nanocrystals, the contribution of surface recombination decreases, and the presence of a short-wavelength band indicates a competitive advantage of the recombination channel. It is associated with recombination in the volume of cadmium sulfide nanocrystals over surface recombination.

# Chapter 7

## *Characterization of the CdS nanoparticles in different host matrices: Evaluation of CdS thin films in device structures for dielectric and memory applications.*

This chapter provides a detailed morphological, and structural characterization of CdS nanoparticle in solution. The CdS nanoparticles were also incorporated into several type of host polymer matrices and the corresponding thin films were integrated in several types of device structures used as an electrical characterization tools. Device structures encompass simple sandwich structure between two symmetric electrodes, field effect transistors, and heterojunctions. The investigations reveal a transformative electroforming process occurring within the thin films of CdS nanoparticles embedded in PVP, resulting in a significant alteration of electrical conduction properties. We propose to further investigate this phenomenon as a potential application for "write once, ready many times" (WORM) type of memory It is found that the thin films of CdS nanoparticles embed into PVP undergo an electroforming process that modifies the electrical conduction. It is proposed to explore this phenomena as write once and ready many times (WORM) typo of memory. Heterojunctions, also exhibit resistive switching phenomena with an interesting rectifying behaviour, but limited by the short lifetime of the high conductive state.

## 7.1. Optical and morphological characterization of CdS nanoparticles in different host matrices.

### 7.1.1. Introduction

Since cadmium sulfide is a direct band gap material, it can be used in photoelectronic devices. The luminescent property of CdS nanocrystals has wide potential applications for different optical devices. Also, semiconductor nanoparticles show size-dependent luminescence, optical and electrical properties which find a number of applications in many areas as discussed previously. There are different techniques to obtain and characterize CdS nanocrystals embedded in polymer matrices, some of them were presented in Chapter 3 of this thesis.

The aim of this work was to investigate nanoparticles of cadmium sulfide in the colloidal solution of different polymers and host matrices. Thin-film devices based on CdS NPs were fabricated and characterized. Upon electroforming, it was found that CdS thin films behave as a nanodielectric. The optical, electrical, morphological, and structural characterisation of the CdS thin films is presented here.

### 7.1.2. Experimental

#### (a) Sample preparation

Nanoparticles of cadmium sulfide in different matrices, namely, photographic gelatin, N,N-dimethylformamide (DMF), polyvinylpyrrolidone (PVP), polystyrene sulfonate sodium salt (PSSNa), were obtained using a patented variation of the sol-gel method described in detail in Chapter 3, based on a colloidal chemistry method [159] , Patent of V. A. Smyntyna et.al.[182]. Briefly, in the case of photographic gelatin, an aqueous solution of cadmium nitrate ($Cd(NO_3)_2$) - (0.025M) was mixed with a 5% solution of photographic gelatin, and, under continuous stirring, a sulphide sulfur ($Na_2S$) solution (0.05M) was slowly added drop-by-drop. The mole ratio of solution's components were the following: 1:3:1, i.e. 1 part of $Cd(NO_3)_2$ + 3 parts of polymer + 1 part of $Na_2S$. The process was carried out at 40 $^0$C, under continuous stirring for 60 minutes. This synthesis of cadmium sulfide proceeds according with the following exchange reactions:

$Cd(NO_3)_2+Na_2S \Longrightarrow CdS+2NaNO_3.$

Gelatin isolates the nanoparticles in the volume and stabilizes their growth. Usually, the concentration of gelatin (or other polymer/solvent) was 5 %.

In the case of photographic gelatine, the synthesis process was completed by adjusting the solution's pH. This adjustment was achieved by adding either an alkaline solution (sodium hydroxide - NaOH) to raise the pH or an acid solution (hydrochloric acid - HCl or acetic acid - $CH_3COOH$) to lower it. This pH manipulation was employed to precisely control the size of the nanoparticles, as described in Chapter 3. The obtained pH values were 4, 6, 8 and 10, resulting in solutions embedded in a gelatin matrix displaying a range of colors, from light yellow (at pH = 4) to dark yellow (at pH = 10).

Colloidal solution of the product was deposited on a glass substrate by drop cast. Subsequently, it was left in air to be dried at a temperature of 35 ºC, for 24 hours. This duration allowed for the complete polymerization of the gelatin. As a result of this process, thin film comprising cadmium sulfide nanocrystals dispersed within a gelatin matrix were successfully produced with nanocrystals of cadmium sulfide dispersed in a gelatin matrix were obtained. The thickness of these films typically ranged from 5 to 10 µm, depending on the amount of liquid initially deposited on the glass substrate.

The CdS nanoparticles were separated from the liquid phase using a centrifugation process that lasted for 30 minutes. After this separation, they were carefully dried in an oven. The resulting product, which exhibited an orange color, was subsequently finely changed into powder manually using a mortar. This powder was then subjected to structural and morphological analysis.

The above-described processes were repeated for other types of polymers and solvents, in order to obtain CdS nanoparticles in different host matrices, we used N,N-dimethylformamide (DMF) (AnalaR NORMAPUR), polyvinylpyrrolidone (PVP) (Sigma Aldrich) with a molecular weight of 40 kD, and polystyrene sulfonate sodium salt (PSSNa) with a molecular weight of 30 kD.

**(b) Characterization techniques**

An optical analysis of the samples across various mediums was carried out, including liquid solutions, powders, and thin-films. Additionally, we performed electrical measurements on both free-standing films and drop-cast thin films, using a range of substrates that encompassed Metal-Insulator-Semiconductor Field-Effect Transistors (MISFETs) and heterojunctions.

Electrical measurements were carried out using a picoammeter/voltage source, (Keithley 487) in dark conditions under ambient atmosphere at room temperature. Several

types of devices based on thin films on top of substrates and free-standing films were fabricated and characterized. Electrical connections were established by gold wires connected using conductive silver paint to both surfaces of the free-standing film.

Metal-insulator-semiconductor field effect transistors (MISFET) substrates used in the present work (Planar Systems Inc, Finland) were composed of indium tin oxide (ITO)-coated glass (8Ω⁄sq)(8Ω⁄sq) onto which ~220nm~220nm of ATO ($Al_2O_3$) was deposited by ALD.

MISFET substrates were cleaned by ultrasonication in a mild detergent solution, rinsed in ultrapure water, followed by drying using a hot-air blower. Subsequently, CdS film, ~1μ thick, was drop cast onto the substrates.

Devices based on nanoparticles of CdS were divided into groups, depends on the host matrix. CdS nanoparticles mainly were incorporated into PVP polymer, polystyrene sulfonate sodium salt (PSSNa), photographic gelatin and DMF solvent. Table 7.1 summaries the samples and their basic properties.

We categorized devices utilizing CdS nanoparticles according to their host matrices. The primary hosts for CdS nanoparticles included PVP polymer, polystyrene sulfonate sodium salt (PSSNa), photographic gelatin, and DMF solvent. A summary of the sample structure along with their basic electrical properties is shown in Table 7.1.

**Table 7.1. List of devices fabricated using CdS nanoparticles embedded on different host matrices.**

| Sample | Sample structure | Electrical properties and behaviour |
|---|---|---|
| 1 | Sandwich structure (CdS+PVP on $n^+$Si substrate completed with top Ag contacts. | Rectifying diode exhibiting resistive switching |
| 2 | Sandwich structure fabricated on free standing films (Au/CdS(PVP)/Au) | Capacitor-like behaviour |
| 3 | Planar structure with interdigitated electrodes (Au/CdS(PVP)/Au) | Capacitor-like behaviour |
| 4 | CdS(PVP) on MISFET structure | Field-effect transistor |
| 5 | Sandwich structures with free standing films (Au/CdS(PVP)/Au) | Capacitor-like after charge trapping (electroforming) |

| | | |
|---|---|---|
| 6 | CdS+PSSNa on MISFET substrate | Capacitor-like behaviour |
| 7, 8 | CdS(PSSNa) poly(sodium styrene sulfonate) on MISFET substrate | Capacitor that changes to a rectifying diode behaviour |
| 9, 10,11, and 12 | Au/CdS(gelatin)/Au on ATO ($Al_2O_3$) substrates | Capacitor-like behaviour |
| 13 | Au/CdS + Gelatin /Au | Capacitor-like behaviour |
| 14 | Au/(CdS+PVP+PANI)/Au | |
| 15 | Au/(CdS + DMF)/Au | |

## 7.2. Characterization of CdS nanocrystals

### 7.2.1. Morphology and structure of NP

The structural analysis of the synthesized CdS NPs has been carried out using XRD technique. The XRD pattern consists of three diffraction peaks. Figure 7.1 presents the X-ray diffraction (XRD) pattern of the powder obtained from a concentrated solution of CdS NPs within a PVP polymer matrix. The XRD peaks exhibit significant broadening, suggesting the presence of small grain sizes. This broadening, along with the low intensity of the primary diffraction peak at $2\Theta = 26^0$, indicates the formation of CdS nanoparticles with small dimensions [118]. The X-ray diffraction (XRD) measurements confirm the formation of single-phase CdS nanoparticles in a cubic crystal structure.

The XRD pattern prominently displays three broad peaks at 2Θ values approximately 26, 44, and 52 degrees, readily assignable to scattering from the (111), (220), and (311) crystallographic planes, respectively, of cubic CdS [183], [184]. In line with this observation, a similar XRD pattern reported in reference [185], also features diffraction peaks located at 26.1, 43.8 and 51.5 degrees, correspondingly indexed as (111), (220) and (311) crystallographic planes. This consistent pattern reinforces the assertion that the synthesized CdS NPs adopt a face-centered cubic phase with the zinc blende structure [186].

The determination of the CdS particle size (*D*) was performed by calculating it from the full width at half-maximum of the (111) peak, employing the Debye-Scherrer equation as shown below

$$\mathrm{D} = \frac{K\lambda}{\beta\cos(\Theta)} \qquad (7.1)$$

Where *K* is a shape factor constant (~0.9), λ is the X-ray wavelength, β is the full width at half-maximum of the diffraction line, and $\theta$ is the angle of diffraction. The particle sizes fall within the range of 5–15 nm, specifically referencing the (111) crystal plane.

Raman spectra confirmed the presence of CdS nanoparticles in the samples, with the predominant peak occurring at a wavenumber of 302.4 $cm^{-1}$ (Figure 7.2).

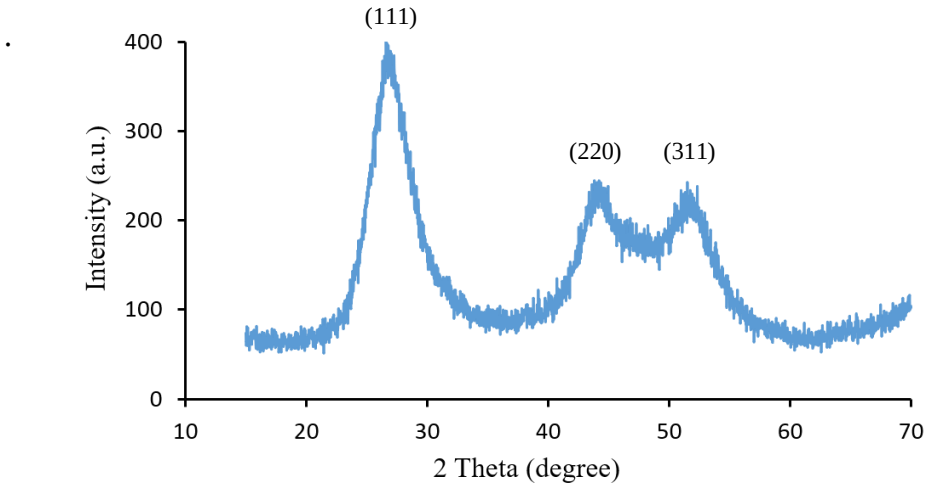


**Figure 7.1**. XRD pattern of the powder derived from a concentrated CdS solution within a PVP polymer matrix.

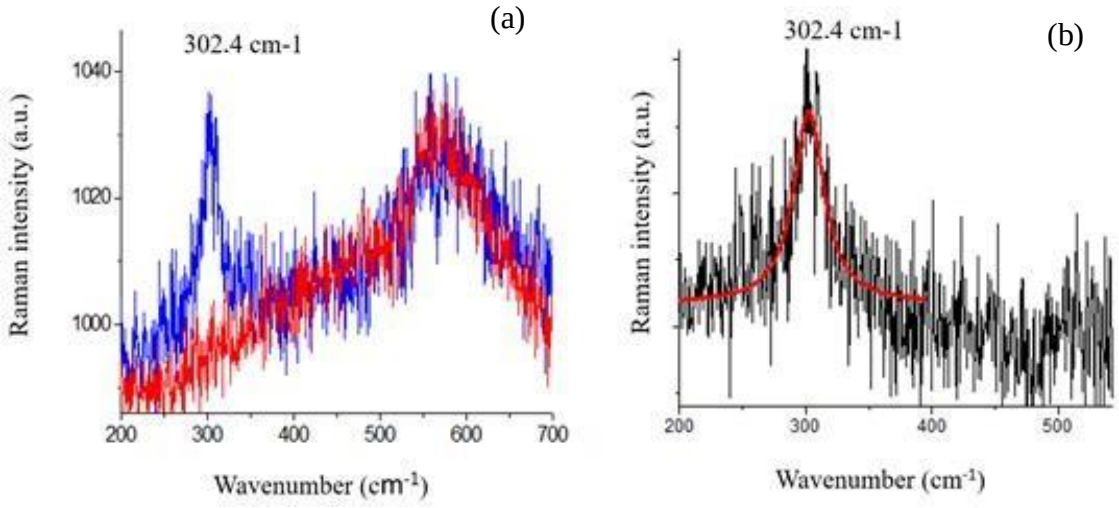


**Figure 7.2**. Two Raman spectra, denoted (a) and (b), measured for two identical samples of CdS NPs within a PVP polymer matrix. (b) - Gaussian curve fitting.

To calculate the crystallite size by using Raman spectroscopy, we used the Tuinstra Koenig relation:

Crystallite size ($La$) = $2.4\times10^{-10}$ [wavelength of laser (nm)]$^4$ / ID:IG ratio;

Ratio of the intensity of D- Raman peak and G- Raman peak (ID/IG) is often used for characterization in order to estimate number and size of the clusters and investigate how the interference effects in the film influence this ratio. The calculated size of the nanoparticles fell within the range of 2 to 5 nm.

Figure 7.3 shows scanning electron microscopy (SEM) pictures of CdS nanoparticles. The nanoparticles have spheres or rod-like shapes. Such results correlate with relevant information in the literature [187]. There is a possibility they are hollow; however, this must be confirmed. Surface effect had an influence on the nanoparticle's properties. It is important to reveal the chemical activity on the surface of nanocrystals, which are isolated in a polymer matrix. More investigation about the surface effect will be discussed in the next chapters.

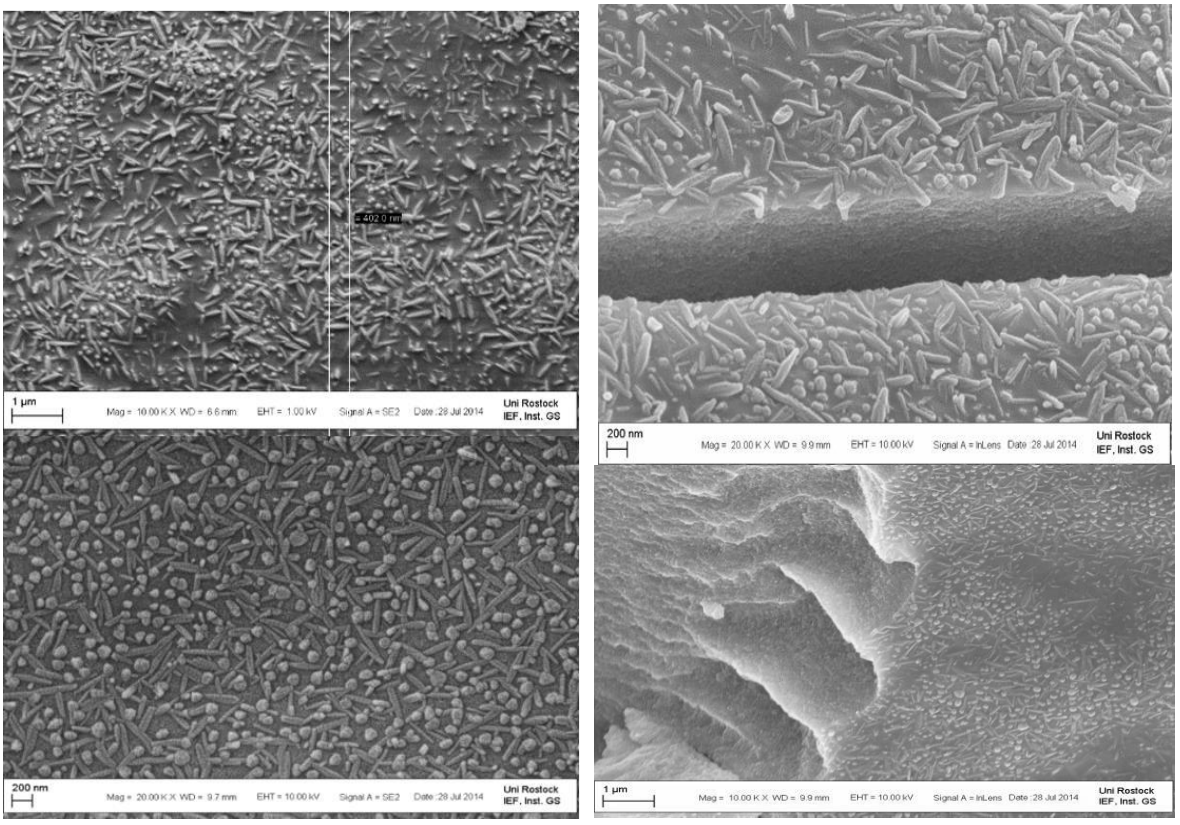


**Figure 7.3.** SEM images of CdS nanoparticles captured at varying magnifications. The upper-right picture shows a cross-section view of the CdS thin film, while the lower-right image shows an extensively damaged region that provides insight into the film thickness.

### 7.2.2. Optical Characterization

The UV-visible absorption spectra of the CdS nanoparticles in solution was investigated. Across all sample types, we observed weak, broad absorption shoulders falling within the range of 380-450 nm. In contrast, bulk CdS typically exhibits an interband absorption transition at approximately 515 nm [188].

Our analysis of the UV-Vis spectra allowed us to ascertain several key parameters, including the energies associated with the first optical transition, the half-width of the peak in the differential curves, and the size of the nanocrystals. To determine the average nanocrystal size, we leveraged the energy data from the first optical transition. Additionally, we obtained the values for the effective widths of the nanocrystal forbidden zones by extrapolating the absorption curves (as depicted in Fig. 7.4) onto the wavelength axis, and calculated using the equation for diameter of nanocrystals of the group $A_2B_6$ [177].

Based on the optical measurements, we estimated the nanoparticle sizes (diameter) as follows: 7.5 nm for CdS in a PSS host matrix, 8.5 nm for CdS in DMF, and 8.2 nm for CdS in PVP. Detailed experimental results are presented in Table 7.2, along with a comparison to samples hosted in gelatin matrices.

In this scenario, the quantum size effect isn't readily apparent, indicating that we can reasonably regard the average radius of these nanoparticles as exceeding 5 nm. Furthermore, the long-wavelength edge of the absorption band, primarily attributed to the largest nanocrystals in the mix, exhibits a noticeable shift towards higher energies when compared to the bandgap energy of bulk CdS.

Figure 7.4 depicts the absorption edge of the nanocrystals is progressively converging with the energy value of the bulk cadmium sulfide band gap (2.5 eV= 495.9 nm). In this case the quantum size effect is not observed, and we can consider the average radius of NP larger than 5 nm. The long-wavelength edge of the absorption band, determined by the contribution of the largest nanocrystals, is shifted relative to the bandgap energy of bulk CdS towards higher energies.

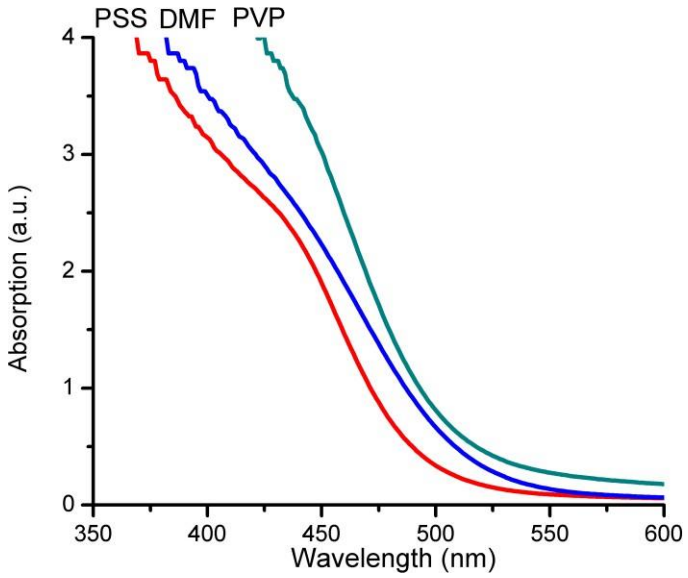


**Figure 7.4.** UV-VIS spectra of CdS nanoparticles in different host matrices.

**Table 7.2. Absorption of samples contained CdS NPs in different host matrices**

| Matrix | λ (nm) | E (eV) | Diameter (nm) |
|---|---|---|---|
| DMF | 516 | 2.40 | 8.5 |
| PVP | 510 | 2.43 | 8.2 |
| PSS | 497 | 2.49 | 7.5 |
| Gelatin | 463 | 2.68 | 5.8 |

Photoluminescence spectra (PL) of both liquid samples and CdS films were measured using fluorimeter. CdS nanocrystals have strong luminescence, characterized by a broad band in the visible region of the spectrum. The peak of this luminescence band varies depending on the pH of the solution used during the NCs synthesis. All nanostructures synthesized within polymers (PVP, PSS), exhibited luminescence bands that included contributions from both the polymer and the nanocrystals. It is worth mentioning that the polymers themselves also emitted luminescence, with their excitation spectrum predominantly situated in the short-wavelength region. Figure 7.5 shown curves corresponding to the three values of pH, where the excitation wavelengths for polymer luminescence were unlikely to interfere. The graph shows that at pH values of 4, 6, and 8, the emission peaks are located at 630-650 nm, 550-580 nm, and 525-555 nm respectively.

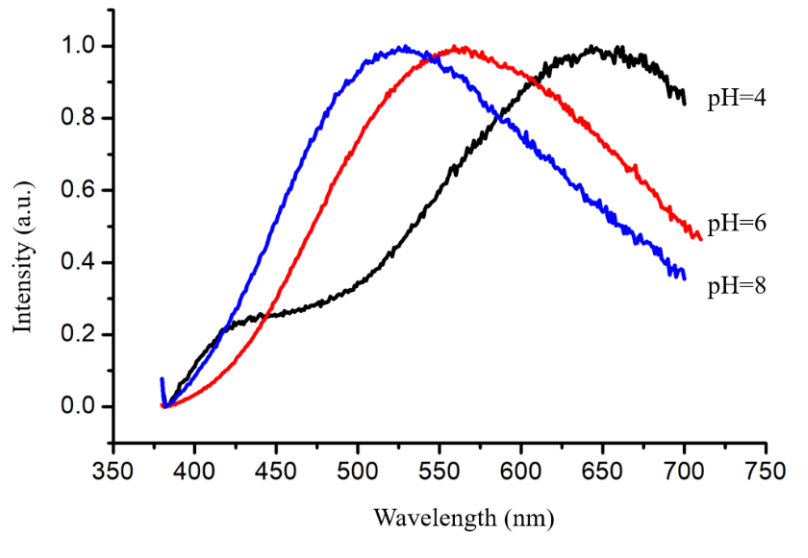


**Figure 7.5**. Photoluminescence of CdS solutions within the gelatin matrix at varying pH levels.

Typically, at low pH values (pH = 4), the maximum bandwidth is observed at longer wavelengths compared to the luminescence of the samples obtained at pH=6 and 8. This behavior can be explained by the different stoichiometry of nanocrystals. At pH=4 in the growth solution, concentration of cadmium ions prevails over the concentration of sulfur ions. As a result, the main defects in these samples will be generated by sulfur vacancies, which contribute to long-wavelength luminescence. This assertion finds support in the luminescence spectra of nanocrystals grown within a natural polymer, gelatin. Gelatin itself does not luminesce in the visible region of the spectrum and therefore, the observed luminescence in

these nanostructures can be attributed solely to the nanocrystals. In this context, a similar trend is noticeable: at lower pH values, the luminescence peak shifts towards longer wavelengths. These findings are further corroborated by the transmission spectra of CdS films within a gelatin matrix at various pH values, as illustrated in Figure 7.6.

Transmission spectra were recorded for films of CdS embedded in a gelatin matrix at varying pH values. The collected data indicate that the polymers themselves do not play a significant role in shaping the defective composition of nanocrystals. Instead, this crucial role is played by the pH solution. In Figure 7.6, the transmission spectra for CdS films within a gelatin matrix at different pH values are depicted. Optical measurements allowed us to estimate the size of the nanoparticles to be in the range 5-8 nm. These experimental findings align with the production processes. Specifically, to achieve a higher concentration of nanocrystals, high concentrations of the initial components must be employed within the matrix.

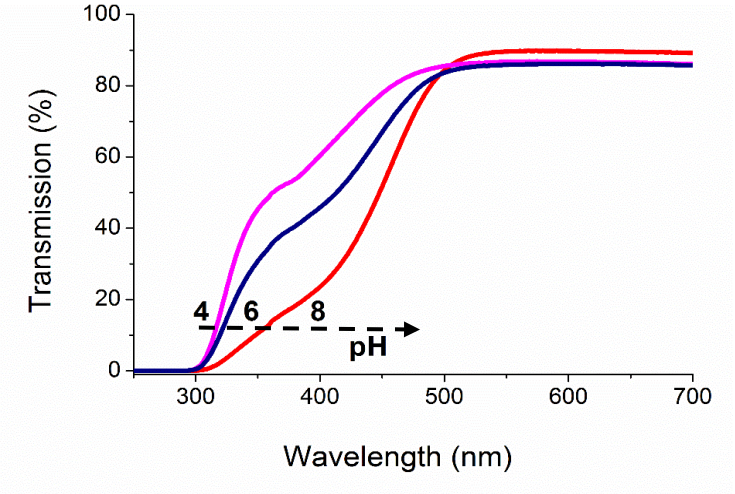


**Figure 7.6**. Spectral transmission characteristics of CdS in a gelatin matrix at varied pH values.

## 7.3. Electroforming of nanodielectrics based on CdS nanoparticles in different polymer host matrices

### 7.3.1 Electrical characterization

In recent times, there has been a growing interest in materials containing nanostructures capable of modulating or influencing their dielectric properties. These materials are known as nanodielectrics [58], [120], [189]–[192].

Due to their promising attributes for applications in both organic and inorganic field effect transistors, significant attention has been directed towards molecular and macromolecular high-permittivity gate dielectric materials. Two categories of thin films have shown particular potential: self-assembled nanodielectrics and cross-linked polymer blends [193], [194]. The approaches for computing the effective permittivity of nanodielectric have also been under discussion. This pursuit aims to design enhanced nanostructures characterized by higher capacitances, reduced leakage current densities, and lower operating voltages.

This section describes electroforming of nanodielectrics based on nanoparticles CdS in the PVP matrix. In order to understand the role of the host matrix on the electrical properties, CdS thin films were prepared in different host materials including gelatin, PVP, PSSNa and PEDOT:PSS. Furthermore, several device architectures were also prepared and characterized. These include sandwich structures, field effect transistors and heterojunctions established with a highly n-type doped ($n^{++}$) silicon substrate. The following sections describe and discuss the basic electrical properties recorded using different host matrices materials and device architectures.

**(a) Sandwich structures (Au/CdS (PVP)/Au) fabricated using CdS free standing films.**

Drop casts thin films of CdS NP easily peel-off from the substrate. These free-standing films were used to fabricate sandwich structures with thermal evaporated gold electrodes on both sides of the film.

Fig. 7.7 illustrates a typical *I-V* curve recorded in these free-standing films. The *I-V* curve is highly asymmetric, characterized by a large hysteresis loop. This electrical asymmetry is a result of transient phenomena that occurs on the initial *I-V* curve. The application of a voltage ramp or a voltage step to the CdS samples alters the injection of charge carriers into the device. Consequently, during the subsequent voltage ramp the injected current remains low. The

alteration in the carrier injection is a transient phenomenon, resulting in a distinctive asymmetry in the *I-V* characteristics as illustrated on Figure 7.7 (a). This electrical asymmetry arises from the applied bias modifying the sample, and it is a long-lived change. During the reverse path of the voltage bias sweep, the current exhibits a comparatively lower magnitude.5

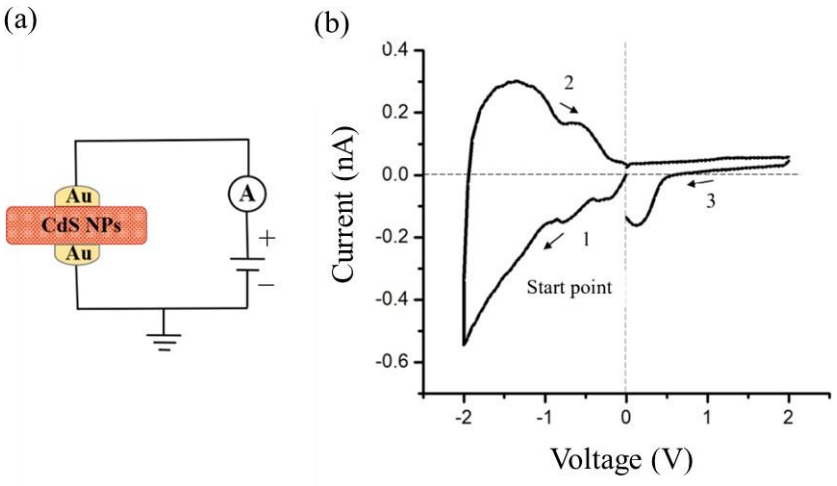


**Figure 7.7.** (a) Schematic diagram of the device structure and the electrical connections (sandwich structure fabricated using free standing film of CdS in PVP). (b) Current-voltage characteristic of sample with nanoparticles of CdS in a PVP matrix. The voltage ramp speed is 0.1 V/s.

The presence of an asymmetric hysteresis loop in Figure 7.7 (a) is attributed to the fact that the bias sweep scan was initially initiated with negative polarities.

If the positive polarities were instead applied first, the large hysteresis loop would have been recorded in the positive quadrant of the *I-V* plot. This asymmetry disappears when multiple *I-V* loops are recorded sequentially, as depicted in Figure 7.8. In Figure 7.8, three consecutive I-V loops are presented. While the first *I-V* loop is strongly asymmetric the third *I-V* loop becomes fully symmetric. This transformation indicates that the sample undergoes modification, ultimately behaving like a pure capacitor. The residual recorded current (*I*) is essentially due to the displacement current ($I=C\frac{dV}{dt}$), where *C* is the device capacitance and $\frac{dV}{dt}$ represents the voltage ramp speed.

We can speculate that the initial current originates from oxidation/reduction of chemical species within the CdS thin film, possibly occurring at the interface between the PVP matrix and the CdS nanoparticles. This field-induced or current induced electrochemical process

blocks further carrier injection. However, it remains unclear whether this electrochemical mechanism results in a permanent alteration or if it represents a reversible effect. It's conceivable that, over time, perhaps after several months of storage under short-circuit conditions, the sample may regain its original behavior.

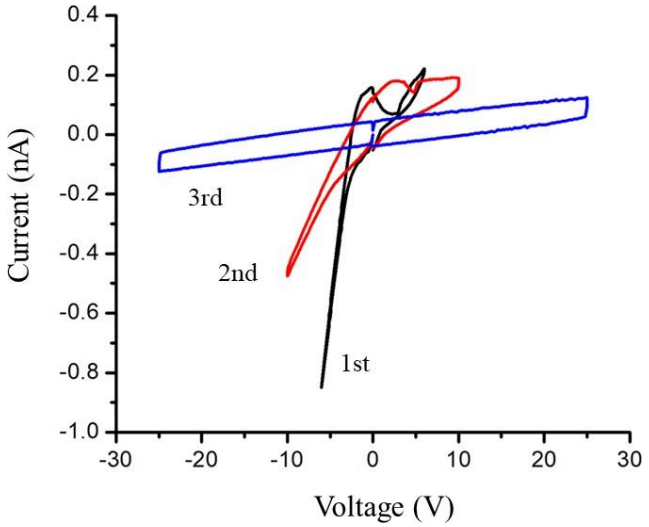


**Figure 7.8**. Evolution of I-V loop behavior following three sequential voltage ramps.

An electrical field of approximately $E \approx 10^8$ V/m can be applied across the junction without causing dielectric breakdown. Figure 7.9 shows a displacement current loop measure up to 50V. Remarkably, this field strength is nearly at the threshold required field to cause dielectric breakdown in conventional oxide layers such as aluminum oxide ($E=10^9$ V/m). This exceptional high dielectric strength is surprising in view of the high density of CdS nanoparticles present in the host polymer matrix.

We propose that the electrochemical mechanism generates specific defects or species capable of storing a cloud of charges on the surfaces of CdS nanoparticles. This charge accumulation must be compensated by nearby trapped charges within the polymer, potentially resulting in the creation a Coulomb blockade effect [195] which hinders the electrical conduction across the nanoparticles-polymer matrix. Nevertheless, further investigation are required to elucidate the origin of this high dielectric strength [196].

When metal or semiconductor particles, such as quantum dots, are scaled down to nanoscale, they exhibit an electrically insulating property known as the Coulomb blockade effect. The Coulomb blockade effect has been investigated for field-effect transistors by adjusting the tunnel resistance [197]. Recent findings [198], suggest that employing a dielectric

polymer with surface-engineered ceramic fillers exploiting the a Coulomb-blockade effect of metal NPs, could be a potential technique for high energy storage devices.. However, there has been limited research into dielectric energy storage systems thus far.

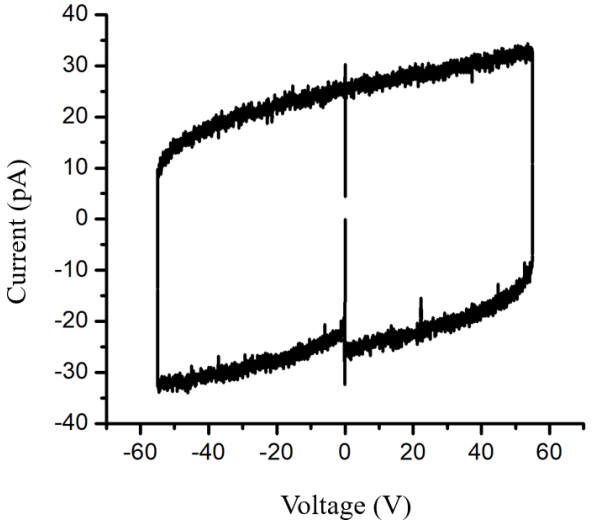


**Figure 7.9**. Current-voltage characteristic of a 2 µm thick free-standing film of CdS within a PVP matrix.

It is of interest to determine whether the process responsible for the electroforming of the CdS thin film is a voltage-drive or a current driven process. To gain insight into nature of the electroforming, we fabricated a Metal-Insulator-Semiconductor (MIS) Field Effect Transistor (FET) structures, hence referred to as MISFETs. In these structures, the channel layer of the transistor consists of a CdS thin-film drop cast on top of MIS structure. The drain and source terminals were fabricated with two gold fingers deposited by thermal evaporation and separated apart by 1mm. The dielectric layer is an ATO layer ($Al_2O_3$) deposited by atomic layer deposition (ALD) on top of an ITO coated glass substrate (see chapter on experimental and methods). These substrates are readily available commercially and were purchased from Planar Systems Inc, Finland. The MISFET device structure is depicted on the inset of Figure 7.10. Figure 7.10 illustrates the MISFET *I-V* characteristics in the voltage range *Vds*=[0;10] V with applied voltage on the gate *Vg*=[0V- 20V].

The drain-source current only initiates a noticeable increase above 4 V, indicating the presence of a built-in barrier at the electrodes. For voltages exceeding 4 V the current increases linearly with the applied voltage. The transversal field applied on the gate can modulate the electrical conduction on the CdS thin film. However, this modulation of the transistor channel

conduction is relatively poor. Modulation of the transistor channel was observed both for positive polarities as well as for negative polarities, which suggest that the CdS thin film is an ambipolar material. Increasing the gate voltage for voltages higher than 20 V, a saturation of the drain-source current modulation is observed. Since the ATO surface is $Al_2O_3$ layer which absorbs several chemical species (water and oxygen) which can act as charge carrier traps. We suspect that the device electrical behaviour (lack of channel current modulation at high fields) is determined by the presence of traps on the $Al_2O_3$/CdS interface.

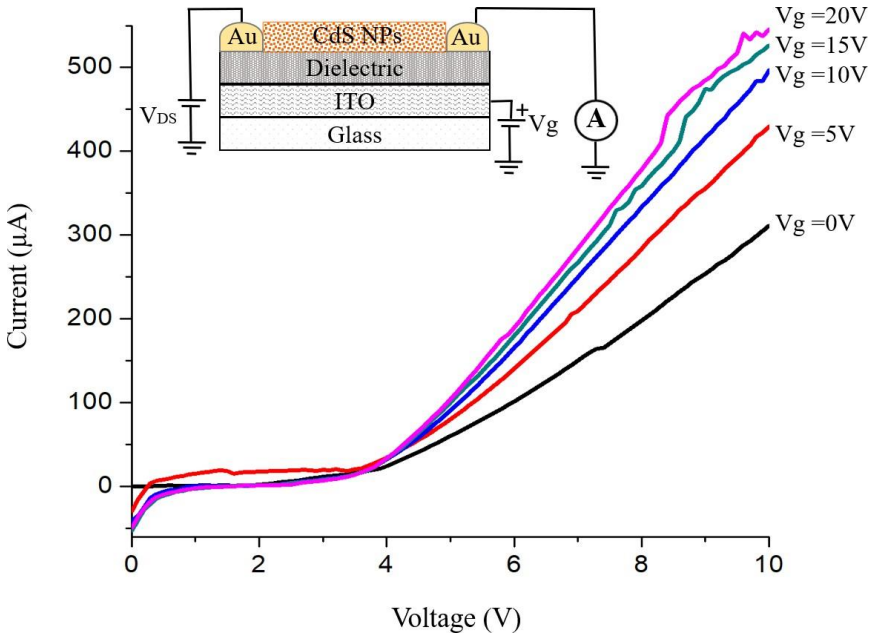


**Figure 7.10.** Measurements with applied voltage on the gate. The inset is a schematic diagram of the MISFET structure where the transistor channel is a drop cast CdS film, 1µm thick.

### (b) Planar structures (Au/CdS (PVP)/Au cast in glass substrates (Samples 2 and 3)

Samples of the sandwich type, previously described above, were fabricated with free standing thin films. Additionally, CdS thin-films were also fabricated on glass substrates by drop casting process. These substrates feature pre-existing interdigitated gold electrodes arranged in a planar architecture. The minimum distance between the electrodes is 1 mm. Consequently, the electrode spacing in these samples is significantly larger compared to the freestanding films discussed earlier, which typically have thicknesses in the range of 2-5 µm.

The electrical characterization of these type of samples confirms the insulating nature of the CdS thin films. Devices behave as pure capacitors up to ± 50 V as shown in the inset of Fig. 7.11. Leakage currents, and electrical instabilities only appear at voltages as high 125 V. This voltage corresponds to an electrical field of $E$=125/0.01=12.5 kV/cm. Typical *I-V* characteristics are shown on Figure 7.11.

During the electrical characterization of the planar samples, we did not initially observe the initial charging or electroforming phenomenon, as mentioned earlier for the freestanding samples. The primary reason for missing this behavior was our lack of awareness regarding this transient phenomenon at that time. It was only during later data analysis that we recognized the presence of transient charging currents. It is possible that the distinctive behavior of the first *I-V* loop went unnoticed, and we focused solely on the stable and reliable *I-V* curves.

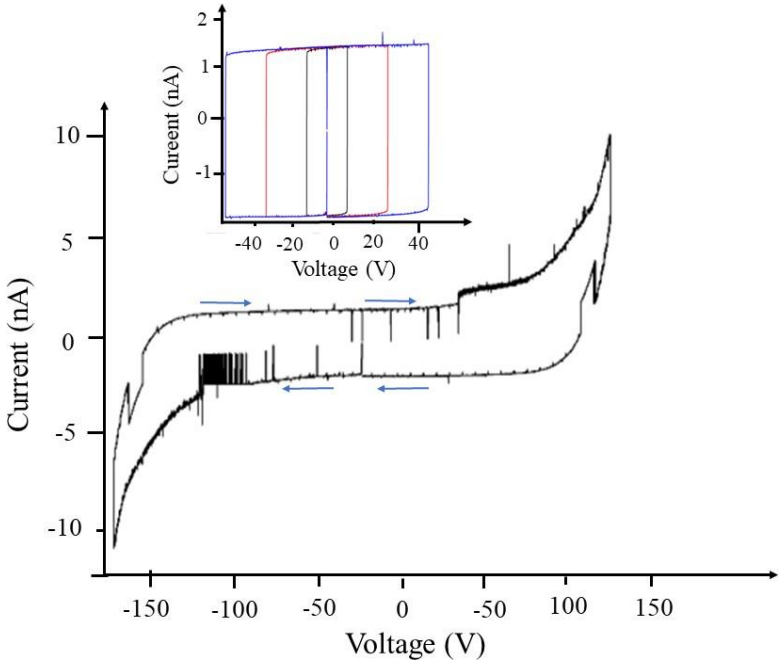


**Figure 7.11.** Current voltage characteristics of Au/CdS(PVP)/Au planar structures drop cast onto an ATO substrate.

### (c) Electrical properties of planar structures using gelatin (Au/CdS (gelatin)/Au).

Sample type 9, as indicated in Table 7.1, was fabricated with CdS within a gelatin host matrix. These thin films were dropping cast onto an insulating ATO substrate featuring pre-existing interdigitated gold electrodes. The *I-V* characteristics exhibited the expect capacitor-like behaviour, as illustrated in Fig. 7.12. Devices were exposed to ambient light, but no noticeable changes were detected.

To investigate whether the inclusion of PVP could influence the electrical behavior, samples with PVP incorporated into the gelatin matrix were also prepared (sample 12 in Table 7.1). Figure 7.13 shows a typical *I-V* characteristics for a gold/CdS (gelatin(PVP)/gold planar structure. In the first scan, the *I-V* curve shows a large hysteresis loop (for negative polarities). This hysteresis once again results in an apparent asymmetric *I-V* behavior mirroring the behavior of the free standing Au/CdS(PVP)/Au samples reported above. This finding suggests that the presence of PVP on the host matrix is responsible for the transient charging effect.

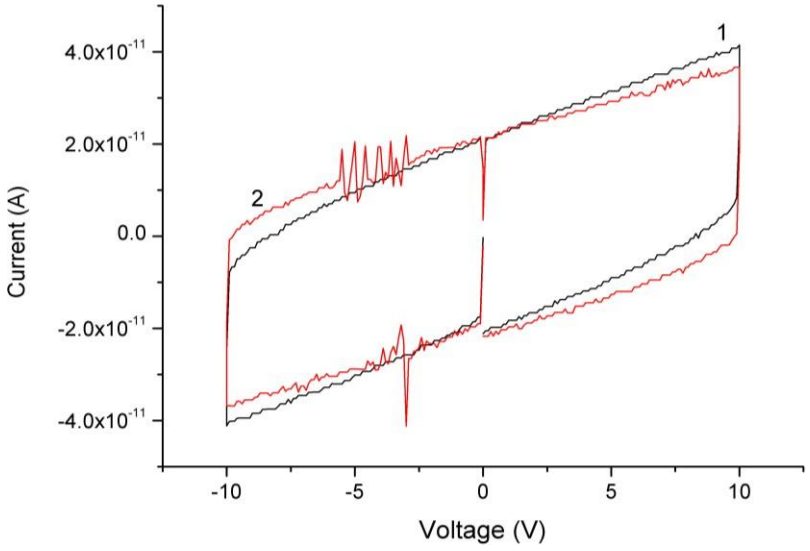


**Figure 7.12**. Current-voltage characteristics loops measured in a planar device using a CdS thin film within a gelatin matrix (Au/CdS (gelatin)/Au).

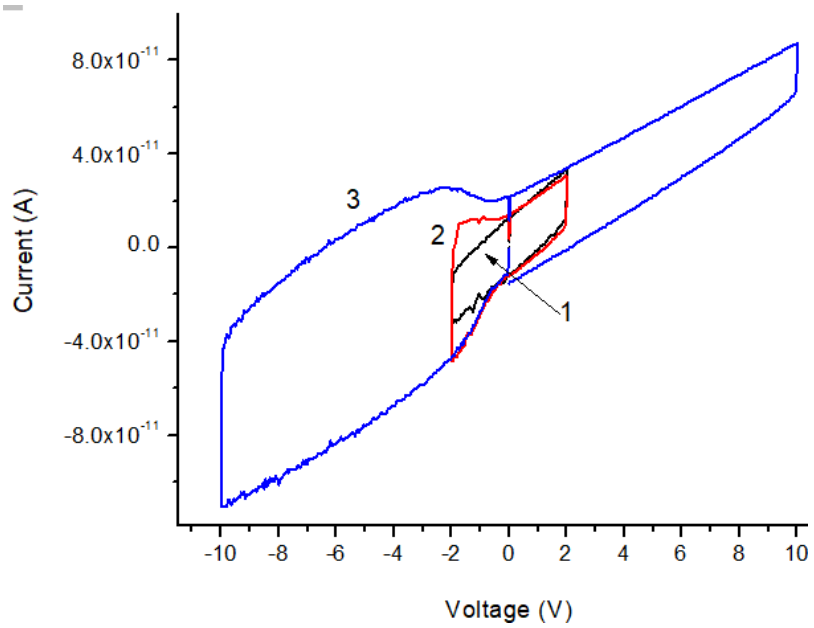


**Figure 7.13.** Typical *I-V* characteristics of a gold/CdS (gelatin(PVP)/gold planar structure.

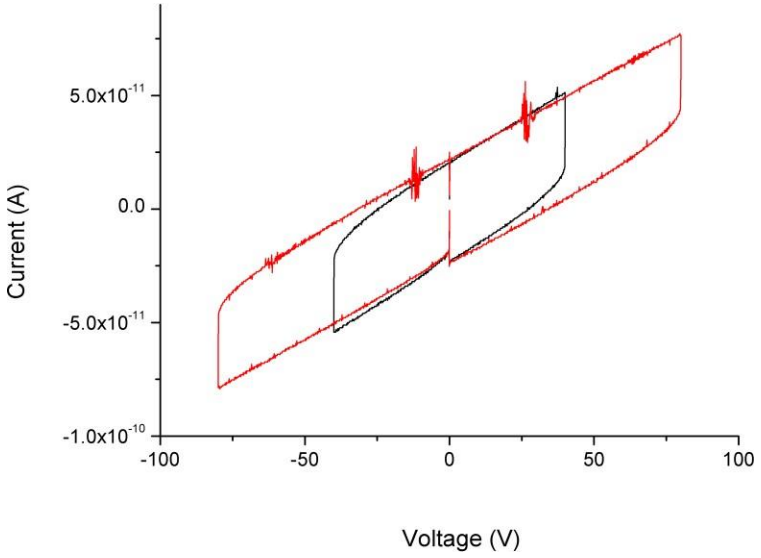


**Figure 7.14**. Typical *I-V* characteristics for an Au/CdS (gelatin (PVP)/Au planar structure (Sample type 12).

**(d) Electrical properties of planar devices using polystyrene sulfonate sodium salt/CdS (PSSNa)/Au.**

To investigate the influence of the polymer host matrix, PVP was also replaced by PSSNa. The testing device is a planar device architecture on top of an insulating $Al_2O_3$ (ATO substrate) and in top of thermally oxidized silicon wafers. Interdigitated gold fingers were used as electrical contacts. (Samples type 6, 7 and 8 in Table 7.1).

Figure 7.15 presents the *I-V* characteristics of the device based on the CdS:PSS thin film. Measurements were carried out at room temperature and dark conditions. The initial *I-V* characteristic has a large hysteresis loop indicative of significant charge trapping. This is visible through abrupt current jumps occurring at 2 nA when the amperemeter stops to change scale. This temporary pause of the voltage ramp at a particular fixed voltage during the measurement causes the current to decrease (see inset on Figure 7.15). Consequently, during a bias sweep, the current undergoes repeated drops to lower levels whenever the voltage remains constant.

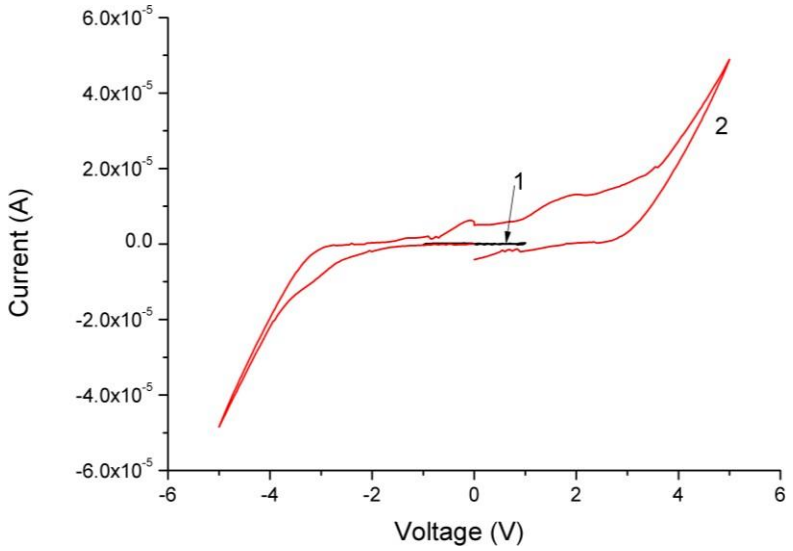


**Figure 7.15**. Typical *I-V* characteristics of a planar structure composed of Au/CdS (PSSNa)/Au (Sample type 6, 7 and 8 from Table 7.1)

Upon extending the voltage sweep to higher voltages (± 5V) reveals an *I-V* curve reveals humps and shoulders indicative of oxidation and reduction peaks. A typical *I-V* curve illustrating these distinctive features is shown on Figure 7.15. As the voltage continues to rise, up to approximately (± 10 V), the *I-V* curve becomes approximately linear. However, the *I-V* curve on Figure 7.16 shows that the CdS/PSSNa interface is not ohmic for low applied voltages

(V<|3V|). We speculate that this non-ohmic behavior is caused by a strong trapping phenomena occurring near the electrode/CdS interfaces.

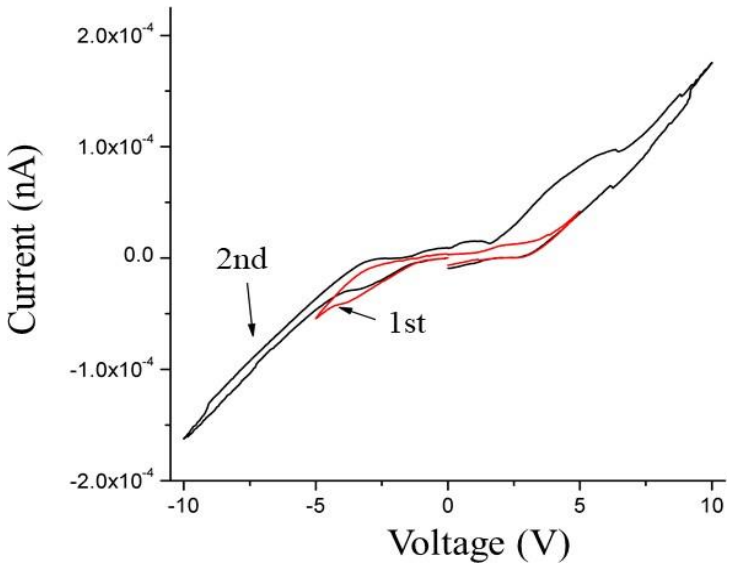


**Figure 7.16**. Typical *I-V* characteristics of a planar structure composed of (Au/CdS (PSSNa)/Au) (Sample type 6, 7 and 8 from Table 7.1).

**(e) Electrical properties of $n^{++}$Si/CdS-PVP/Ag heterojunction structures sandwich structures. Sample type 1 in Table 7.1.**

Heterojunctions fabricated using highly doped silicon substrates ($n^{++}$Si/CdS(PVP)/Ag) were also electrically characterized. A schematic diagram of the device structure is shown in Figure 7.17. Heterojunctions using highly doped silicon ($n^{++}$) and CdS thin films can exhibit resistive switching phenomena. The *I-V* curves can change from a high resistance state (HRS) to a low resistance state (LRS). Figure 7.17 (a) illustrates a typical swishing the *I-V* characteristic. The HRS state has the behavior of a typical capacitor (see Figure 7.17 (a)). The LRS has rectifying properties (see Figure 7.17 (c)).

The observation of a rectifying behavior in the LRS is particularly interesting, because until now all the resistive switching memories reported in the literature exhibit symmetric *I-V* characteristics when programmed into an LRS. Symmetric *I-V* curves can lead to crosstalk when memories are integrated in cross bar arrays. This crosstalk has been the major limitation on the commercialization of resistive switching memories.

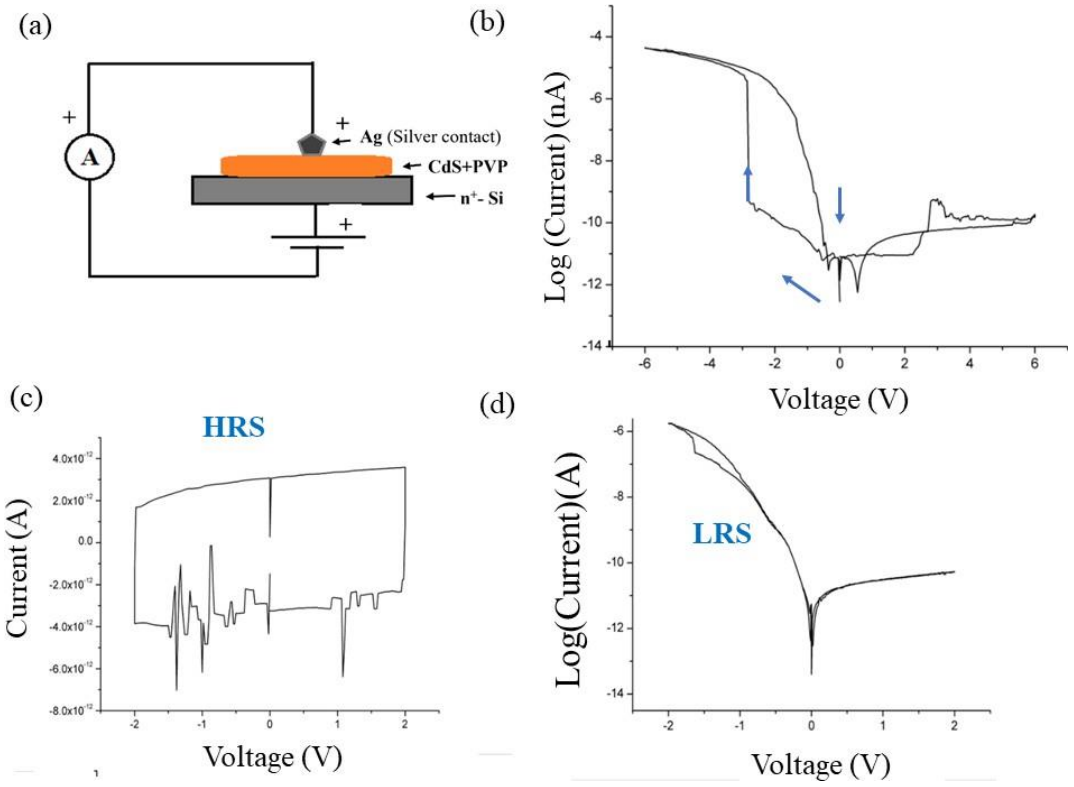


**Figure 7.17.** Heterojunction device structure and resistive switching behavior. (Schematic diagram showing the device structure, (b) Resistive switching from a HLR to an LRS. (b) Typical *I-V* curve for a HRS and (d) Typical *I-V* curve for the LRS.

To ensure that this behavior was not induced solely by the highly doped silicon substrate we also fabricated and characterized control samples where the heterojunction was fabricated without the CdS layer. A typical *I-V* curve is shown in Figure 7.18 although is clear that the rectification is due to the silicon substrate, the devices without the CdS layer do not exhibit resistive switching behaviour. A typical *I-V* curve for a heterojunction without the CdS layer is shown in Figure 7.18.

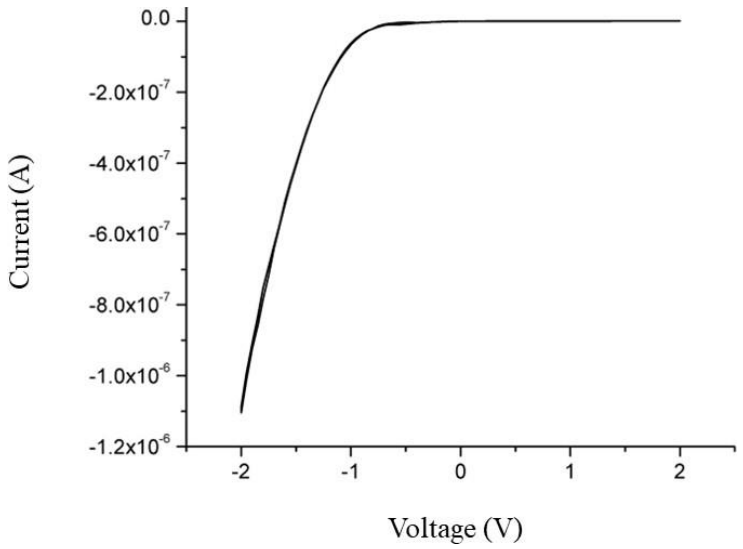


**Figure 7.18.** Current-voltage characteristic for $n^{++}$Si/Ag heterojunction without the CdS thin film.

## 7.4. Conclusions

Morphological, structural, optical, and electrical analysis were carried out on CdS nanoparticles embedded in different polymer matrices. The presence of CdS nanoparticles was confirmed by x-ray diffraction (XRD) spectra which exhibited the signature of the cubic structure of CdS. Structural characterization revealed the presence of spheres and rod-shaped structures.

Optical measurements allowed for the estimation of an average nanoparticle size ranging from 3 to 8.5 nm. The pH of the solution has a direct influence on the size of the nanoparticles, the higher the pH, the larger the nanoparticle size.

The photoluminescence of the obtained CdS nanocrystals has intensive luminescence with a broad band in the visible region of the spectrum. The peak of the luminescence band was found to be dependent on both the pH of the solution and type of the host polymer matrix.

Several CdS thin films were prepared using different host matrices. CdS thin films prepared using a PVP host matrix show a trapping process possibly driven by electrochemistry. Following this trapping the sample transformed into an insulating material, a phenomenon termed by us "electroforming of a dielectric." It remains uncertain whether this material modification is a permanent induced change, or it has only a very long lifetime (several weeks).

Once electroformed, the free-standing films CdS has a dielectric breakdown field higher than $10^8$ V/m. We propose that this insulation behavior is due to a charge coulomb effect in the CdS nanoparticles. It is also suggested that this electroforming process can potentially be explored to make write once and read many times (WORM) type of memory.

Heterojunctions involving $n^{++}$Si/CdS-PVP/Ag show resistive switching effect. The on-off ratio is 6 orders of magnitude at |4V|. The LRS has rectifying properties, which is a crucial property for the technological application of these memory devices in crossbar arrays. However, the switching is not reliable. HRS and LRS states can be recorded, yet the LRS was found to be somewhat unstable and often spontaneously decays to the HRS. It was not possible to assure a very long lifetime of the LRS. The lifetime of the LRS can be just a few minutes. The nature of the resistive switching also remains unclear. It is conceivable that mobile silver ions (from the silver top contact) may contribute to the formation of silver filaments across the CdS thin film. Since silver ions can be mobile, it is possible that silver filaments are created across the CdS thin film. To validate this hypothesis, it would be valuable to fabricate heterojunctions with gold metal contacts replacing the silver contacts.

MISFET type of devices where the conduction channel consists of is a CdS thin films show clear evidence for a field effect modulation of the channel layer conductivity. The transversal gate field cannot electroform the CdS layer as observed for the free-standing films. This finding suggests that electroforming is not a field induced process; instead, it implies that current plays a pivotal role in the electroforming phenomenon current plays a crucial role in the electroforming. This result supports the view that electroforming of the dielectric based on the CdS nanoparticles is driven by electrochemistry.

# Chapter 8

*Conclusions and future work*

The goal of this thesis is to study resistive switching devices. This study was divided into two main parts, each focusing on distinct materials. In the first part, the resistive switching phenomena on a wide band gap halide, the LiF, is presented and described. Subsequently, the second part of this study involves an exploration of the electrical properties of CdS nanoparticles within various host matrices. The motivation for studying nanoparticles was inspired by many reports of resistive switching systems based on nanoparticles.

The research conducted on LiF/polymer diodes has provided valuable insights into the underlying physical process occurring during the early stages of the electroforming. In the case of CdS based systems, we achieved successful observation of resistive switching exclusively when a heterojunction junction was fabricated. These devices exhibit two interesting characteristics; (i) a substantial on-off ratio differentiating the LRS from the HRS and, (ii) the LRS demonstrates rectifying properties. However, it remained unclear whether the observed resistive switching was related to CdS nanoparticles or the migration of silver ions across the CdS layer. Another relevant result within the CdS/PVP system was the observation of trapping phenomena or a current driven electrochemical process that modifies the CdS thin film into a dielectric material. This transformation requires a charging current, bearing some resemblance to the electroforming process observed by us in the halides and oxides (reported in Chapter 4). This process was named “electroforming of a nanodielectric”.

In the following sections, we highlight the major findings made throughout this thesis and their significance. Initially, we will provide a critical review of the findings from the LiF/polymer system, followed by a summary of the relevance and principal conclusions derived from the research involving CdS nanoparticles-based devices.

**(a) Resistive switching in LiF/polymer-based devices**

The primary novelty of this thesis work lies in the examination of the initial phases of electroforming. Despite the intense efforts of the scientific community, the microscopic physical mechanism responsible for transforming an oxide or a halide into a switchable material remained unknown. In our perspective, this knowledge gap can be attributed to the challenges associated with observing the transient electrical phenomena responsible for the generation of defects and the subsequent alteration of the material's electrical characteristics. The outcomes presented in this thesis indicate that the initial mechanism is primarily an electronic process instigated by a charge trapping phenomenon. The trapping of electrons at the interface

insulator/polymer induces a soft-dielectric breakdown in the insulator layer and metastable defects are created.

Interfacial traps (impurities) play an important role in initiating the resistive switching phenomena. Pure clean insulating materials do not exhibit resistive switching behavior. The presence of impurities rises several pertinent questions, including their specific location within the energy gap of the insulator. Another crucial question revolves around the existence of a critical trap density required to induce breakdown. Understanding the chemical origin of these impurities and devising methods to control their density and spatial distribution also represent significant research challenges.

To provide an answer to these questions, it is of utmost importance to map and get the signatures of the electronic sates and eventually establish a connection between device manufacturing and the memory performance. However, material and device properties make this study, a particularly challenging one. In resistive switching devices we are dealing with wide bandgap materials, traps in these insulators are so energetically deep that measuring their signatures (energetic depth and capture cross section) is difficult. In other words, deep traps readily capture charge carries, but they may take months or years to release them into the respective energy bands. Detecting the relaxation in the frequency domain caused by the trap filling /emptying mechanism is unpractical using small-signal impedance methods. To identify trap states using electrical techniques we must instead inspect for their enduring impacts on the quasi-static electrical behavior of the device.

The second challenge is related to the device architecture. Resistive switching devices typically adopt MIM structures. MIM structures perform well as switching devices because the charges carriers communicate directly with the nearby metal contact. This direct interaction results in fast charge carrier injection and extraction, leading to rapid switching speeds. However, this fast charge dynamics poses a challenge when attempting to observe these processes. To address this challenge, it becomes crucial to slow down the charge carrier dynamics responsible for the switching event. One effective approach is to introduce an additional semiconductor layer into the MIM structure, characterized by low charge carrier mobility, such as a $\pi$-conjugated polymer.

The device is turned into a metal-insulator-semiconductor (MIS) diode. The impedance of a MIS device is controlled by two layers in series, a high capacitive and high resistance insulating layer followed by a relatively low capacitance and low resistance semiconductive layer. The impedance of this two-layer system has a classical Maxwell-Wagner relaxation when the impedance is plotted as function of the frequency. The Maxwell-Wagner relaxation

results from the interplay between the two layers impedance. Furthermore, the low charge carrier mobility within the semiconductor layer slows down the trap filling and makes it possible to measure the transient current that fills the traps located at the insulator/semiconductor interface. In this thesis, we employed MIS devices as a strategic approach to gain insight into charge trapping at the LiF/polymer interface and about the subsequent electroforming process that changes the pristine device into a resistive switching memory.

Chapter 4 makes use of a MIS structures and presents a detail investigation on the trapping phenomena and their consequences on the device quasi-static impedance. It is concluded that when the device is in the pristine state, the current flowing through the device is a transient trapping current. Once the field is removed the trap emptying process generates a current of opposite sign which causes a NDR region on the *R-V* curves and an excess capacitance on the *C-V* curves. The excess capacitance is not a static capacitance but a small-signal capacitance. The slow diffusing of electrons out of the device causes an increase in the phase angle between voltage and current, which is interpreted by the impedance analyser as an additional capacitance.

The trapping of electrons at the LiF/polymer interface continues to take place even after the diode is electroformed. Evidence for these traps is provided by the frequency and voltage dependence of the capacitance and resistance. Therefore, it is proposed that LiF/polymer interfacial traps play an important role not only in causing the soft-dielectric breakdown of the LiF (electroforming) but also, they also influence the switching behavior in the switching properties of the electroformed diode.

**Suggestions for further work**

While we have presented compelling evidence for a trapping mechanism occurring at the interface between the insulator/semiconductor interface, we have yet to obtain detailed information about the characteristics of these traps. To gain insight into the nature of the traps, temperature dependent studies must be carried out. By changing the temperature, the activation energy of the process can in principle be determined. Temperature-dependent experiments can provide the energetic distribution of traps in the band gap. Preliminary results have shown that the traps are not discrete but are distributed in a broad impurity band. The data presented on Chapter 4 showed that in the electroformed state there is large density of shallow states that

can respond to the ac test signal frequency below 1 kHz. Based on this preliminary evidence we propose to use electroformed devices where the shallow states are clearly visible on the impedance *vs* frequency plots. We intend to conduct temperature-dependent experiments, particularly focusing on temperatures above room temperature.

Previous studies obtained by the research group have also showed that the traps are intimated related with the filamentary conduction. Essentially, traps act as micro-switches, when filled, induce a low resistance path (filament) across the insulator, when empty they switch-off the filament. Therefore, by probing filamentary conduction as function of the temperature, we can gain insight about the trap occupancy at a particular temperature and about the trap energetic depth and capture cross section. An interesting method to measure these micro-switching events is Random-Telegraph Noise (RTS) techniques. Therefore, we propose to measure the RTS noise as a function of the temperature for different applied bias.

Unpublished results from our group also suggest that traps are metastable, which is a typical feature of water-related traps. Indeed, water and oxygen impurities have been suggested as possible candidates. In summary, the following experiments are proposed.

1- Study the frequency dependence of the low frequency capacitance tail reported in Chapter 4 for the electroformed LiF diode. We propose conducting experiments within a temperature range spanning from 273 K and 350 K. This temperature range has been selected for specific reasons: temperatures below 273 K may render traps unresponsive to the AC signal, whereas temperatures exceeding 350 K could potentially induce defect annealing processes that may interfere with the observations.

2- Study the Random-Telegraph Noise (RTS) noise as function of the temperature. During these experiments it is important to prime a specific population of traps. In principle this selection can be done by an adequate selection of the applied bias and temperature.

3- Adjust the manufacturing parameters, specifically regarding the water contamination and closely monitor the resulting alterations on the resistive switching properties. Establishing a clear cause-and-effect relationship between manufacturing procedures and device properties is essential for identifying the specific chemical species.

### (b) Electrical properties of CdS nanoparticles embed into different host matrices

This thesis provided a morphological, structural, optical, and electrical characterization of CdS nanoparticles embedded in different host matrices.

In current work were prepared CdS nanoparticles incorporated in polymer matrix of photographic gelatin, PVP (polyvinylpyrrolidone), PSSNa - poly(sodium styrene sulfonate) and dimethylformamide (DMF) solvent. Cadmium sulfide (CdS) nanoparticles (NPs) were synthesized by a chemical method and have been characterized using such techniques as XRD analysis, Raman spectroscopy, absorption, and photoluminescence (PL) emission spectroscopy. The optical and morphological analysis for CdS nanoparticles were obtained by UV-Vis absorption spectroscopy and SEM electron microscope measurements. The synthesized CdS nanoparticles exhibit a spherical morphology, indicative of their cubic structure, and display a remarkably narrow size distribution. These CdS nanoparticles are known to manifest apparent excitonic absorption peaks and quantum confinement effects. Optical measurements reveal that the average size of these nanoparticles ranges from 3 nm to 22 nm in diameter.

This research uncovered the significant impact of varying pH levels and the type of host matrix on the size and stabilization properties of these nanoparticles. These influences are readily observable in the optical absorption and photoluminescence spectra, particularly in terms of the luminescence band's peak position and intensity. Moreover, the results underscore the efficacy of photographic gelatin and PVP as effective stabilizers for the formation of CdS nanoparticles.

Throughout this thesis a number of device structures incorporating thin films of CdS nanoparticles were fabricated and characterized. These structures encompassed a range of configurations, including free standing sandwich structures, planar structures using interdigitated gold electrodes, heterojunctions with highly doped *n*-type silicon, and a MISFET device.

The primary objective was to use the CdS thin films in in the development of resistive switching devices. Unexpectedly, it was observed that even when CdS nanoparticles were incorporated at very high concentrations within several host matrices, their behavior did not align with typical semiconductor characteristics, as initially anticipated. Instead, the CdS nanoparticles exhibited insulating properties, and this insulating behavior was induced when a small current was passed through the thin film containing a high concentration of CdS

nanoparticles. The findings reported in Chapter 7 indicate that this transient current causes an oxidation/reduction reaction which then blocks further carrier injection into the CdS film.

Comparison with the electrical behaviour of the MISFET device indicates that the application of a transversal electrical field does not causes permanent changes in the CdS film. Therefore, it was concluded that the process is a current driven electrochemical process. We speculate that during the application of the current, defects are created in the thin film. These electroformed defects are possible located at the interface CdS/polymer interface. The defects act as charge carrier traps in the CdS nanoparticles surface which are compensated by opposite charges of opposite sign located the bulk of the nanoparticles. To summarize, each individual nanoparticle behaves as a micro-capacitor and the overall film behaves as an insulator. The electrochemistry process leads to large hysteresis on first *I-V* loop. This changeis permanent or long-lived (lasting for several weeks).

Resistive switching behaviour was observed in heterojunction devices. However, it should be noted that the top contact in the heterojunction is established by printing a silver ink contact. Therefore, it cannot be ruled out that the presence of silver or silver oxide species, which may form upon contact with ambient air, could potentially influence or even dominate the observed resistive switching phenomenon.

The relevant finding from the electrical characterization of CdS heterojunctions is the observation of a low-resistance state (LRS) that exhibits a pronounced rectification, spanning approximately six orders of magnitude. To the best of our knowledge, this is the first time that it is reported a resistive switching memory device with a rectifying LRS. The presence of rectifying LRS state holds promise for addressing the critical issue of cross-talk between neighbouring memory pixels when integrated into crossbar arrays. Unfortunately, the lifetime of the LRS was not long enough, and exhibit a large variability on lifetime ranging from minutes to days. The origin of this variability is not clear but prevented us to claim that the heterojunction behaves as non-volatile memory.

**Suggestions for further work**

Based on the discussion above, it is evident that this work has raised significant questions regarding charge trapping and transport within thin films composed of CdS nanoparticles. Further studies are required to elucidate the electroforming of the insulating properties as well as the resistive switching behaviour in the heterojunctions. Towards that end, the following experiments are proposed:

1. Experiments on the heterojunction device.

The silver contact needs to be replaced with a gold contact to ascertain whether the observed resistive switching is intrinsic to the CdS nanoparticles or triggered by silver oxide species infiltrating the CdS layer. Addressing the short lifespan and associated instability of the LRS is imperative. It's plausible that this instability stems from electrostatic interactions between atmospheric species and the device surface. Consequently, all forthcoming experiments should be conducted with the devices maintained under vacuum or within a controlled atmosphere.

2. Experiments to elucidate the dielectric behaviour for the system CdS/polymer.

The first aspect to study is to measure the kinetics of the initial current that changes the electrical properties of the CdS thin film. The sample should be submitted to voltages steps with increasing amplitude and the corresponding decay in current monitored. The activation energy of the process should be quantified by recording the decay time constants at different temperatures.

The potential reversibility of the current-induced changes should be accurately quantified. After the samples have undergone electroforming, periodic monitoring is essential to assess the recovery time. Small-signal impedance techniques can play a crucial role in this regard, as they allow for monitoring the sample's resistance with minimal disturbance.

3. Device modelling.

A physical model needs to be formulated to elucidate the insulating behavior of CdS. This model should take into account the characteristics of CdS nanoparticles and their interactions within the surrounding polymer matrix. It is hypothesized that defects at the CdS/polymer interface might function as charge carrier traps. Compensatory charges within the bulk semiconductor could potentially create electrical dipoles that obstruct the flow of carriers between nanoparticles.

# References


[1] B. F. Bory, S. C. J. Meskers, R. A. J. Janssen, H. L. Gomes, and D. M. De Leeuw, "Trapping of electrons in metal oxide-polymer memory diodes in the initial stage of electroforming," *Appl. Phys. Lett.*, vol. 97, no. 22, pp. 1–4, 2010, doi: 10.1063/1.3520517.

[2] A. Kiazadeh *et al.*, "Operational stability of solution based zinc tin oxide/SiO2 thin film transistors under gate bias stress," *APL Mater.*, vol. 3, no. 6, 2015, doi: 10.1063/1.4919057.

[3] I. H. Inoue and A. Sawa, "Resistive Switchings in Transition-Metal Oxides," in *Functional Metal Oxides*, vol. 11, no. 6, Weinheim, Germany: Wiley-VCH Verlag GmbH & Co. KGaA, 2013, pp. 443–463.

[4] Q. Chen, H. L. Gomes, A. Kiazadeh, P. R. F. Rocha, D. M. De Leeuw, and S. C. J. Meskers, "Electroforming Process in Metal-Oxide-Polymer Resistive Switching Memories," in *IFIP Advances in Information and Communication Technology*, vol. 372 AICT, 2012, pp. 527–534.

[5] B. F. Bory, P. R. F. Rocha, R. A. J. Janssen, H. L. Gomes, D. M. De Leeuw, and S. C. J. Meskers, "Lithium fluoride injection layers can form quasi-Ohmic contacts for both holes and electrons," *Appl. Phys. Lett.*, vol. 105, no. 12, 2014, doi: 10.1063/1.4896636.

[6] S. Liu, C. L. Zhang, F. C. Wang, Y. Zhang, and H. X. Li, "Studying the attribution of LiF in OLED by the C-V characteristics," *Int. J. Photoenergy*, vol. 2010, 2010, doi: 10.1155/2010/291931.

[7] B. F. Bory, H. L. Gomes, R. A. J. Janssen, D. M. de Leeuw, and S. C. J. Meskers, "Electrical conduction of LiF interlayers in organic diodes," *J. Appl. Phys.*, vol. 117, no. 15, p. 155502, Apr. 2015, doi: 10.1063/1.4917461.

[8] M. I.Mishcenko and L. D.Travis, "Gustav Mie and the evolvingdiscipline of electromagnetic scattering by particles," *BAMS - Bull. Am. Sci. Soc.*, no. April, pp. 5–24, 2016.

[9] D. A. Pomogailo *et al.*, "Spectral luminescence properties of CdS nanocomposites in a polymer shell," *Compos. Mech. Comput. Appl.*, vol. 8, no. 2, pp. 171–180, 2017, doi: 10.1615/CompMechComputApplIntJ.v8.i2.50.

[10] R. Viter *et al.*, "Tuning of ZnO 1D nanostructures by atomic layer deposition and electrospinning for optical gas sensor applications," *Nanotechnology*, vol. 26, no. 10, p. 105501, Mar. 2015, doi: 10.1088/0957-4484/26/10/105501.

[11] L. Zheng *et al.*, "Metal Ions Redox Induced Repeatable Nonvolatile Resistive Switching Memory Behavior in Biomaterials," *ACS Appl. Bio Mater.*, vol. 1, no. 2, pp. 496–501, Aug. 2018, doi: 10.1021/acsabm.8b00226.

[12] G. U. Kamble, A. P. Patil, R. K. Kamat, J. H. Kim, and T. D. Dongale, "Promising Materials and Synthesis Methods for Resistive Switching Memory Devices: A Status Review," *ACS Appl. Electron. Mater.*, vol. 5, no. 5, pp. 2454–2481, May 2023, doi: 10.1021/acsaelm.3c00062.

[13] V. A. Smyntyna, V. M. Skobeeva, and T. F. Zavezion, “Imputity influence of the matrix solution on the size of Cdmium Sulfide nanocrystals, synthesized by sol-gel technology,” *Sens. Electron. Microsyst. Technol.*, vol. 5, no. 3, pp. 69–73, Jun. 2008, doi: 10.18524/1815-7459.2008.3.114998.

[14] Y. A. Nitsuk, M. I. Kiose, Y. F. Vaksman, V. A. Smyntyna, and I. R. Yatsunskyi, “Optical Properties of CdS Nanocrystals Doped with Zinc and Copper,” *Semiconductors*, vol. 53, no. 3, pp. 361–367, Mar. 2019, doi: 10.1134/S1063782619030138.

[15] F. Mitri, A. De Iacovo, M. De Luca, A. Pecora, and L. Colace, “Lead sulphide colloidal quantum dots for room temperature NO2 gas sensors,” *Sci. Rep.*, vol. 10, no. 1, p. 12556, Dec. 2020, doi: 10.1038/s41598-020-69478-x.

[16] S. Kim, B. Fisher, H.-J. Eisler, and M. Bawendi, “Type-II Quantum Dots: CdTe/CdSe(Core/Shell) and CdSe/ZnTe(Core/Shell) Heterostructures,” *J. Am. Chem. Soc.*, vol. 125, no. 38, pp. 11466–11467, Sep. 2003, doi: 10.1021/ja0361749.

[17] M. Maleki, M. Sasani Ghamsari, S. Mirdamadi, and R. Ghasemzadeh, “A facile route for preparation of CdS nanoparticles,” *Semicond. Physics, Quantum Electron. Optoelectron.*, vol. 10, no. 1, pp. 30–32, Jun. 2007, doi: 10.15407/spqeo10.01.030.

[18] S. I. Pokutnyi, “Interband absorption of light in semiconductor nanostructures,” *Semiconductors*, vol. 37, no. 6, pp. 718–722, Jun. 2003, doi: 10.1134/1.1582542.

[19] A. Eychmüller, “Structure and Photophysics of Semiconductor Nanocrystals,” *J. Phys. Chem. B*, vol. 104, no. 28, pp. 6514–6528, Jul. 2000, doi: 10.1021/jp9943676.

[20] B. Hwang and J.-S. Lee, “Recent Advances in Memory Devices with Hybrid Materials,” *Adv. Electron. Mater.*, vol. 5, no. 1, p. 1800519, Jan. 2019, doi: 10.1002/aelm.201800519.

[21] C.-C. Hsieh, A. Roy, A. Rai, Y.-F. Chang, and S. K. Banerjee, “Characteristics and mechanism study of cerium oxide based random access memories,” *Appl. Phys. Lett.*, vol. 106, no. 17, p. 173108, Apr. 2015, doi: 10.1063/1.4919442.

[22] K. Sattler, “The energy gap of clusters, nanoparticles, and quantum dots,” in *Handbook of Thin Films*, vol. 5, Elsevier, 2002, pp. 61–97.

[23] V. Smyntyna, B. Semenenko, and V. M. Skobeeva, “Effect of surface on the luminescence properties of CdS nanocrystals,” *Electron. Inf. Technol.*, no. 2, pp. 45–50, 2012.

[24] J. J. Yang, M. D. Pickett, X. Li, D. A. A. Ohlberg, D. R. Stewart, and R. S. Williams, “Memristive switching mechanism for metal/oxide/metal nanodevices,” *Nat. Nanotechnol.*, vol. 3, no. 7, pp. 429–433, Jul. 2008, doi: 10.1038/nnano.2008.160.

[25] D. Prime and S. Paul, “Overview of organic memory devices,” *Philos. Trans. R. Soc. A Math. Phys. Eng. Sci.*, vol. 367, no. 1905, pp. 4141–4157, Oct. 2009, doi: 10.1098/rsta.2009.0165.

[26] T. W. Hickmott, “Low-Frequency Negative Resistance in Thin Anodic Oxide Films,” *J. Appl. Phys.*, vol. 33, no. 9, pp. 2669–2682, Sep. 1962, doi: 10.1063/1.1702530.

[27] T. W. Hickmott, “Potential distribution and negative resistance in thin oxide films,” *J. Appl. Phys.*, vol. 35, no. 9, pp. 2679–2689, 1964, doi: 10.1063/1.1713823.

[28] J. G. Simmons and R. R. Verderber, “New conduction and reversible memory phenomena in thin insulating films,” *Proc. R. Soc. London. Ser. A. Math. Phys. Sci.*, vol. 301, no. 1464, pp. 77–102, Oct. 1967, doi: 10.1098/rspa.1967.0191.

[29] R. R. Sutherland, “A theory for negative resistance and memory effects in thin insulating films and its application to Au-ZnS-Au devices,” *J. Phys. D. Appl. Phys.*, vol. 4, no. 3, p. 318, Mar. 1971, doi: 10.1088/0022-3727/4/3/318.

[30] R. D. Gould and C. A. Hogarth, “Forming, negative resistance, and dead-time effects in thin films of CaBr2,” *Phys. Status Solidi*, vol. 23, no. 2, pp. 531–535, 1974, doi: 10.1002/pssa.2210230224.

[31] T. W. Hickmott, “Electron emission and ultraviolet electroluminescence from valence-band states and defect conduction bands of electroformed Al-Al 2 O 3 -Ag diodes,” *J. Appl. Phys.*, vol. 125, no. 2, p. 025305, Jan. 2019, doi: 10.1063/1.5024665.

[32] T. W. Hickmott, “Millimeter distance effects of surface plasmon polaritons in electroformed Al-Al 2 O 3 -Ag diodes,” *J. Appl. Phys.*, vol. 121, no. 8, p. 083101, Feb. 2017, doi: 10.1063/1.4976715.

[33] T. W. Hickmott, “Electroforming and Ohmic contacts in Al-Al2O3-Ag diodes,” vol. 063708, no. February 2012, 2015.

[34] M. B. H. Din and R. D. Gould, “Dielectric breakdown and electroforming phenomenon in the cadmium arsenide thin films devices,” in *ICSE’98. 1998 IEEE International Conference on Semiconductor Electronics. Proceedings (Cat. No.98EX187)*, 1998, no. 1, pp. 179–183, doi: 10.1109/SMELEC.1998.781175.

[35] G. Dearnaley, D. V. Morgan, and A. M. Stoneham, “A model for filament growth and switching in amorphous oxide films,” *J. Non. Cryst. Solids*, vol. 4, no. C, pp. 593–612, 1970, doi: 10.1016/0022-3093(70)90097-9.

[36] G. Dearnaley, D. V. Morgan, and A. M. Stoneham, “A model for filament growth and switching in amorphous oxide films,” *J. Non. Cryst. Solids*, vol. 4, no. C, pp. 593–612, Apr. 1970, doi: 10.1016/0022-3093(70)90097-9.

[37] D. P. Oxley, “Electroforming, Switching and Memory Effects in Oxide Thin Films,” *Electrocompon. Sci. Technol.*, vol. 3, no. 4, pp. 217–224, 1977, doi: 10.1155/APEC.3.217.

[38] A. J. Kenyon, M. Singh Munde, W. H. Ng, M. Buckwell, D. Joksas, and A. Mehonic, “The interplay between structure and function in redox-based resistance switching,” *Faraday Discuss.*, vol. 213, pp. 151–163, 2019, doi: 10.1039/c8fd00118a.

[39] T. N. Török, J. G. Fehérvári, G. Mészáros, L. Pósa, and A. Halbritter, “Tunable, Nucleation-Driven Stochasticity in Nanoscale Silicon Oxide Resistive Switching Memory Devices,” *ACS Appl. Nano Mater.*, vol. 5, no. 5, pp. 6691–6698, May 2022, doi: 10.1021/acsanm.2c00722.

[40] D. S. Jeong, H. Schroeder, U. Breuer, and R. Waser, “Characteristic electroforming behavior in Pt/TiO2/Pt resistive switching cells depending on atmosphere,” *J. Appl. Phys.*, vol. 104, no. 12, p. 123716, Dec. 2008, doi: 10.1063/1.3043879.

[41] S. Munjal and N. Khare, “Advances in resistive switching based memory devices,” *J. Phys. D. Appl. Phys.*, vol. 52, no. 43, p. 433002, Oct. 2019, doi: 10.1088/1361-6463/ab2e9e.

[42] X. Xing, M. Chen, Y. Gong, Z. Lv, S.-T. Han, and Y. Zhou, “Building memory devices from biocomposite electronic materials,” *Sci. Technol. Adv. Mater.*, vol. 21, no. 1, pp. 100–121, Jan. 2020, doi: 10.1080/14686996.2020.1725395.

[43] D. Porotnikov and M. Zamkov, “Progress and Prospects of Solution-Processed Two-Dimensional Semiconductor Nanocrystals,” *J. Phys. Chem. C*, vol. 124, no. 40, pp. 21895–21908, Oct. 2020, doi: 10.1021/acs.jpcc.0c06868.

[44] L. D. Bozano, B. W. Kean, V. R. Deline, J. R. Salem, and J. C. Scott, “Mechanism for bistability in organic memory elements,” *Appl. Phys. Lett.*, vol. 84, no. 4, pp. 607–609, 2004, doi: 10.1063/1.1643547.

[45] R. Waser and M. Aono, “Nanoionics-based resistive switching memories,” in *Nanoscience and Technology*, Co-Published with Macmillan Publishers Ltd, UK, 2009, pp. 158–165.

[46] H. L. Gomes, D. M. de Leeuw, and S. C. J. Meskers, “Resistive Switching in Metal Oxide/Organic Semiconductor Nonvolatile Memories,” in *Memristor and Memristive Neural Networks*, InTech, 2018.

[47] C. B. Lee *et al.*, “Effects of metal electrodes on the resistive memory switching property of NiO thin films,” *Appl. Phys. Lett.*, vol. 93, no. 4, p. 042115, Jul. 2008, doi: 10.1063/1.2967194.

[48] J. Wang *et al.*, “A unipolar nonvolatile resistive switching behavior in a layeredtransition metal oxide,” *Nanoscale*, vol. 11, no. 43, pp. 20497–20506, 2019, doi: 10.1039/C9NR07456B.

[49] M. Xiao, K. P. Musselman, W. W. Duley, and N. Y. Zhou, “Resistive Switching Memory of TiO2 Nanowire Networks Grown on Ti Foil by a Single Hydrothermal Method,” *Nano-Micro Lett.*, vol. 9, no. 2, p. 15, Apr. 2017, doi: 10.1007/s40820-016-0116-2.

[50] W.-Y. Chang, Y.-C. Lai, T.-B. Wu, S.-F. Wang, F. Chen, and M.-J. Tsai, “Unipolar resistive switching characteristics of ZnO thin films for nonvolatile memory applications,” *Appl. Phys. Lett.*, vol. 92, no. 2, p. 022110, Jan. 2008, doi: 10.1063/1.2834852.

[51] B. J. Choi *et al.*, “Resistive switching mechanism of TiO 2 thin films grown by atomic-layer deposition,” *J. Appl. Phys.*, vol. 98, no. 3, 2005, doi: 10.1063/1.2001146.

[52] J. Molina *et al.*, “Memristance effect of metal-insulator-metal structures using Al 2O3 film as active layer for emergent memory devices,” *Superf. y Vacio*, vol. 27, no. 1, pp. 1–6, 2014.

[53] Y.-C. Huang, P.-Y. Chen, T.-S. Chin, R.-S. Liu, C.-Y. Huang, and C.-H. Lai, “Improvement of resistive switching in NiO-based nanowires by inserting Pt layers,” *Appl. Phys. Lett.*, vol. 101, no. 15, p. 153106, Oct. 2012, doi: 10.1063/1.4758482.

[54] A. Zaffora, R. Macaluso, H. Habazaki, I. Valov, and M. Santamaria, “Electrochemically prepared oxides for resistive switching devices,” *Electrochim. Acta*, vol. 274, pp. 103–111, 2018, doi: 10.1016/j.electacta.2018.04.087.

[55] Y. Sharma, P. Misra, and R. S. Katiyar, “Unipolar resistive switching behavior of amorphous YCrO 3 films for nonvolatile memory applications,” *J. Appl. Phys.*, vol. 116, no. 8, p. 084505, Aug. 2014, doi: 10.1063/1.4893661.

[56] L. Hu *et al.*, "Unipolar resistive switching characteristics and scaling behaviors in La 2 Mo 2 O 9 thin films for nonvolatile memory applications," *J. Appl. Phys.*, vol. 120, no. 21, p. 215303, Dec. 2016, doi: 10.1063/1.4971762.

[57] J. S. Kwak, Y. H. Do, Y. C. Bae, H. Im, and J. P. Hong, "Reproducible unipolar resistive switching behaviors in the metal-deficient CoOx thin film," *Thin Solid Films*, vol. 518, no. 22, pp. 6437–6440, Sep. 2010, doi: 10.1016/j.tsf.2010.03.050.

[58] M. Roy *et al.*, "Polymer nanocomposite dielectrics - the role of the interface," *IEEE Trans. Dielectr. Electr. Insul.*, vol. 12, no. 4, pp. 629–643, Aug. 2005, doi: 10.1109/TDEI.2005.1511089.

[59] Q. Chen, H. Wang, J. Xu, C. Wei, X. Zhang, and L. Yang, "Low temperature synthesis of amorphous La0.7Zn0.3MnO3 films grown on p+-Si substrates and its resistive switching properties," *J. Wuhan Univ. Technol. Sci. Ed.*, vol. 31, no. 4, pp. 727–730, Aug. 2016, doi: 10.1007/s11595-016-1437-1.

[60] D. Liu *et al.*, "Nonvolatile bipolar resistive switching in amorphous Sr-doped LaMnO 3 thin films deposited by radio frequency magnetron sputtering," *Appl. Phys. Lett.*, vol. 102, no. 13, p. 134105, Apr. 2013, doi: 10.1063/1.4800229.

[61] Y. Zhang, H. Wang, J. Xu, Z. Li, and L. Yang, "Coexistence of Bipolar and Unipolar Resistive Switching Behavior in Ag/ZnMn2O4/p+-Si Device," *J. Wuhan Univ. Technol. Sci. Ed.*, vol. 33, no. 6, pp. 1433–1436, Dec. 2018, doi: 10.1007/s11595-018-1987-5.

[62] S. Gao *et al.*, "Improving Unipolar Resistive Switching Uniformity with Cone-Shaped Conducting Filaments and Its Logic-In-Memory Application," *ACS Appl. Mater. Interfaces*, vol. 10, no. 7, pp. 6453–6462, Feb. 2018, doi: 10.1021/acsami.7b19586.

[63] Q. Chen *et al.*, "Controlled Construction of Atomic Point Contact with 16 Quantized Conductance States in Oxide Resistive Switching Memory," *ACS Appl. Electron.Mater.*, vol. 1, no. 5, pp. 789–798, May 2019, doi: 10.1021/acsaelm.9b00191.

[64] D. Panigrahi, R. Hayakawa, X. Zhong, J. Aimi, and Y. Wakayama, "Optically Controllable Organic Logic-in-Memory: An Innovative Approach toward Ternary Data Processing and Storage," *Nano Lett.*, vol. 23, no. 1, pp. 319–325, Jan. 2023, doi: 10.1021/acs.nanolett.2c04415.

[65] R. Waser, R. Dittmann, G. Staikov, and K. Szot, "Redox-Based Resistive Switching Memories - Nanoionic Mechanisms, Prospects, and Challenges," *Adv. Mater.*, vol. 21, no. 25–26, pp. 2632–2663, Jul. 2009, doi: 10.1002/adma.200900375.

[66] Y. Li, S. Long, Q. Liu, H. Lü, S. Liu, and M. Liu, "An overview of resistive random access memory devices," *Chinese Sci. Bull.*, vol. 56, no. 28–29, pp. 3072–3078, Oct. 2011, doi: 10.1007/s11434-011-4671-0.

[67] L. Chua, "Memristor-The missing circuit element," *IEEE Trans. Circuit Theory*, vol. 18, no. 5, pp. 507–519, 1971, doi: 10.1109/TCT.1971.1083337.

[68] A. Petrov *et al.*, "On the way to a neuromorphic memristor computer platform," *Nanoindustry Russ.*, no. 1, pp. 94–109, 2016, doi: 10.22184/1993-8578.2016.63.1.94.109.

[69] P. K. Katkar *et al.*, "Binder-Free Synthesis of Nanostructured Amorphous Cobalt Phosphate for Resistive Memory and Artificial Synaptic Device Applications," *ACS Appl. Electron. Mater.*, vol. 4, no. 4, pp. 1852–1863, Apr. 2022, doi:

10.1021/acsaelm.2c00085.

[70] J. J. Yang, D. B. Strukov, and D. R. Stewart, “Memristive devices for computing,” *Nat. Nanotechnol.*, vol. 8, no. 1, pp. 13–24, Jan. 2013, doi: 10.1038/nnano.2012.240.

[71] S. Iqbal, M. Kumar, Q. A. Sial, L. T. Duy, and H. Seo, “Thermal Nanostructuring for Rectifying Resistive Switching Behaviors of Cobalt Oxide Neuromorphic Devices,” *ACS Appl. Electron. Mater.*, vol. 4, no. 11, pp. 5573–5581, Nov. 2022, doi: 10.1021/acsaelm.2c01167.

[72] J. T. Jang *et al.*, “One Transistor–Two Memristor Based on Amorphous Indium–Gallium–Zinc-Oxide for Neuromorphic Synaptic Devices,” *ACS Appl. Electron. Mater.*, vol. 2, no. 9, pp. 2837–2844, Sep. 2020, doi: 10.1021/acsaelm.0c00499.

[73] P. Pal, S. Mazumder, C.-W. Huang, D. D. Lu, and Y.-H. Wang, “Impact of the Barrier Layer on the High Thermal and Mechanical Stability of a Flexible Resistive Memory in a Neural Network Application,” *ACS Appl. Electron. Mater.*, vol. 4, no. 3, pp. 1072–1081, Mar. 2022, doi: 10.1021/acsaelm.1c01219.

[74] Z. Shen *et al.*, “Artificial Synaptic Performance with Learning Behavior for Memristor Fabricated with Stacked Solution-Processed Switching Layers,” *ACS Appl. Electron. Mater.*, vol. 3, no. 3, pp. 1288–1300, Mar. 2021, doi: 10.1021/acsaelm.0c01094.

[75] Z. Lv, Y. Wang, J. Chen, J. Wang, Y. Zhou, and S.-T. Han, “Semiconductor Quantum Dots for Memories and Neuromorphic Computing Systems,” *Chem. Rev.*, vol. 120, no. 9, pp. 3941–4006, May 2020, doi: 10.1021/acs.chemrev.9b00730.

[76] J. Kim *et al.*, “Switching Power Universality in Unipolar Resistive Switching Memories,” *Sci. Rep.*, vol. 6, no. 1, p. 23930, Apr. 2016, doi: 10.1038/srep23930.

[77] R. Waser, R. Dittmann, C. Staikov, and K. Szot, “Redox-based resistive switching memories nanoionic mechanisms, prospects, and challenges,” *Adv. Mater.*, vol. 21, no. 25–26, pp. 2632–2663, 2009, doi: 10.1002/adma.200900375.

[78] S. Clima *et al.*, “First-principles simulation of oxygen diffusion in HfO x : Role in the resistive switching mechanism,” *Appl. Phys. Lett.*, vol. 100, no. 13, p. 133102, Mar. 2012, doi: 10.1063/1.3697690.

[79] S. Ng, R. A. John, J. Yang, and N. Mathews, “Forming-Less Compliance-Free Multistate Memristors as Synaptic Connections for Brain-Inspired Computing,” *ACS Appl. Electron. Mater.*, vol. 2, no. 3, pp. 817–826, Mar. 2020, doi: 10.1021/acsaelm.0c00002.

[80] B. F. Bory, P. R. F. Rocha, H. L. Gomes, D. M. de Leeuw, and S. C. J. Meskers, “Unipolar resistive switching in metal oxide/organic semiconductor non-volatile memories as a critical phenomenon,” *J. Appl. Phys.*, vol. 118, no. 20, p. 205503, Nov. 2015, doi: 10.1063/1.4936349.

[81] M. V. Fedorov and A. A. Kornyshev, “Ionic Liquids at Electrified Interfaces,” *Chem. Rev.*, vol. 114, no. 5, pp. 2978–3036, Mar. 2014, doi: 10.1021/cr400374x.

[82] H.-D. Kim, H.-M. An, and T. G. Kim, “Ultrafast Resistive-Switching Phenomena Observed in NiN-Based ReRAM Cells,” *IEEE Trans. Electron Devices*, vol. 59, no. 9, pp. 2302–2307, Sep. 2012, doi: 10.1109/TED.2012.2202237.

[83] R. Seoudi, A. A. Shabaka, M. Kamal, E. M. Abdelrazek, and W. Eisa, “Dependence of

spectroscopic and electrical properties on the size of cadmium sulfide nanoparticles," *Phys. E Low-dimensional Syst. Nanostructures*, vol. 45, pp. 47–55, Aug. 2012, doi: 10.1016/j.physe.2012.07.006.

[84] L. Liu *et al.*, "Inorganic–organic hybrid semiconductor nanomaterials: (ZnSe)(N2H4)x(C5H5N)y," *Mater. Res. Bull.*, vol. 44, no. 6, pp. 1385–1391, Jun. 2009, doi: 10.1016/j.materresbull.2008.11.023.

[85] V. Singh and P. Chauhan, "Structural and optical characterization of CdS nanoparticles prepared by chemical precipitation method," *J. Phys. Chem. Solids*, vol. 70, no. 7, pp. 1074–1079, Jul. 2009, doi: 10.1016/j.jpcs.2009.05.024.

[86] V. Singh, P. K. Sharma, and P. Chauhan, "Synthesis of CdS nanoparticles with enhanced optical properties," *Mater. Charact.*, vol. 62, no. 1, pp. 43–52, Jan. 2011, doi: 10.1016/j.matchar.2010.10.009.

[87] P. Kumar, "Directed Self-Assembly: Expectations and Achievements," *Nanoscale Res. Lett.*, vol. 5, no. 9, pp. 1367–1376, Sep. 2010, doi: 10.1007/s11671-010-9696-9.

[88] P. Bansal, N. Jaggi, and S. Rohilla, "' Green ' Synthesis of CdS nanoparticles and effect of capping agent concentration on crystallite size," *Res. J. Chem. Sci.*, vol. 2, no. 8, pp. 69–71, 2012.

[89] S. D. Bompilwar, S. B. Kondawar, and V. A. Tabhane, "Impedance Study of Nanostructure Cadmium Sulfide and Zinc Sulfide," *Arch. Appl. Sci. Res.*, vol. 2, no. 3, pp. 225–230, 2010.

[90] M. Bangal *et al.*, "Semiconductor Nanoparticles," *Hyperfine Interact.*, vol. 160, no. 1–4, pp. 81–94, Jan. 2005, doi: 10.1007/s10751-005-9151-y.

[91] M. Maleki, "A facile route for preparation of CdS nanoparticles," *Semicond. physics, quantum Electron. Optoelectron.*, vol. 10, no. 1, pp. 30–32, Jun. 2007, doi: 10.15407/spqeo10.01.030.

[92] S. S. Kawar, "Chalcogenide thin films having nanometer grain size for photovoltaic applications," *Res. J. Chem. Sci. ISSN*, vol. 2231, no. December 2011, p. 606X, 2011.

[93] V. Belgamwar, M. Gaikwad, G. Patil, and S. Surana, "Pulsatile drug delivery system," *Asian J. Pharm.*, vol. 2, no. 3, p. 141, 2008, doi: 10.4103/0973-8398.43297.

[94] R. A. Vaia and R. Krishnamoorti, "Polymer Nanocomposites: Introduction," in *Polymer Nanocomposites: Introduction*, 2001, pp. 1–5.

[95] R. Chapman and P. Mulvaney, "Electro-optical shifts in silver nanoparticle films," *Chem. Phys. Lett.*, vol. 349, no. 5–6, pp. 358–362, Dec. 2001, doi: 10.1016/S0009-2614(01)01145-9.

[96] O. Wilson, G. J. Wilson, and P. Mulvaney, "Laser Writing in Polarized Silver Nanorod Films," *Adv. Mater.*, vol. 14, no. 13–14, pp. 1000–1004, Jul. 2002, doi: 10.1002/1521-4095(20020705)14:13/14<1000::AID-ADMA1000>3.0.CO;2-E.

[97] M. M. M. Gudrun Schmidt*, "Properties of polymer–nanoparticle composites," *Curr. Opin. Colloid Interface Sci.*, vol. 8, pp. 103–108, 2003, doi: 10.1016/S1359-0294.

[98] A. M. Smith and S. Nie, "Semiconductor Nanocrystals: Structure, Properties, and Band Gap Engineering," *Acc. Chem. Res.*, vol. 43, no. 2, pp. 190–200, Feb. 2010, doi:

10.1021/ar9001069.

[99] M. Amelia, C. Lincheneau, S. Silvi, and A. Credi, “Electrochemical properties of CdSe and CdTe quantum dots,” *Chem. Soc. Rev.*, vol. 41, no. 17, p. 5728, 2012, doi: 10.1039/c2cs35117j.

[100] E. Rabani, B. Hetényi, B. J. Berne, and L. E. Brus, “Electronic properties of CdSe nanocrystals in the absence and presence of a dielectric medium,” *J. Chem. Phys.*, vol. 110, no. 11, pp. 5355–5369, Mar. 1999, doi: 10.1063/1.478431.

[101] X. H. Fan, H. J. Liu, Y. M. Chen, and T. Sun, “Synthesis and Characterization of CdS Nanoparticles,” *Adv. Mater. Res.*, vol. 848, no. 01, pp. 3–6, Nov. 2013, doi: 10.4028/www.scientific.net/AMR.848.3.

[102] M. Amelia, C. Lincheneau, S. Silvi, and A. Credi, “Electrochemical properties of CdSe and CdTe quantum dots,” *Chem. Soc. Rev.*, vol. 41, no. 17, pp. 5728–5743, 2012, doi: 10.1039/c2cs35117j.

[103] P. Sobrova, M. Ryvolova, J. Hubalek, V. Adam, and R. Kizek, “Voltammetry as a Tool for Characterization of CdTe Quantum Dots,” *Int. J. Mol. Sci.*, vol. 14, no. 7, pp. 13497–13510, Jun. 2013, doi: 10.3390/ijms140713497.

[104] A. Tang *et al.*, “Optical properties and electrical bistability of CdS nanoparticles synthesized in dodecanethiol,” *Appl. Phys. Lett.*, vol. 96, no. 16, p. 163112, Apr. 2010, doi: 10.1063/1.3402770.

[105] S. K. Haram, B. M. Quinn, and A. J. Bard, “Electrochemistry of CdS Nanoparticles: A Correlation between Optical and Electrochemical Band Gaps,” *J. Am. Chem. Soc.*, vol. 123, no. 36, pp. 8860–8861, Sep. 2001, doi: 10.1021/ja0158206.

[106] S. S. Liji Sobhana, M. Vimala Devi, T. P. Sastry, and A. B. Mandal, “CdS quantum dots for measurement of the size-dependent optical properties of thiol capping,” *J. Nanoparticle Res.*, vol. 13, no. 4, pp. 1747–1757, 2011, doi: 10.1007/s11051-010-9934-1.

[107] A. P. Alivisatos, “Semiconductor Clusters, Nanocrystals, and Quantum Dots,” *Science (80-. ).*, vol. 271, no. 5251, pp. 933–937, Feb. 1996, doi: 10.1126/science.271.5251.933.

[108] Y. Wang, “Semiconductor nanocrystals in photoconductive polymers: Charge generation and charge transport,” in *Studies in Surface Science and Catalysis*, vol. 103, no. C, 1997, pp. 277–295.

[109] H. Nur, E. Rismana, and S. Endud, “Dielectric enhancement in cadmium sulfide—poly(methacrylic acid-ethylene glycol dimethacrylic acid) nanocomposite through interfacial interaction,” *J. Compos. Mater.*, vol. 45, no. 19, pp. 2023–2030, Sep. 2011, doi: 10.1177/0021998310394692.

[110] A. A. Ahmed Al-Dulaimi, S. Hashim, and M. I. Khan, “Corrosion protection of carbon steel using polyaniline composite with aluminium oxide,” *Pertanika J. Sci. Technol.*, vol. 19, no. 2, pp. 329–337, 2011.

[111] C. Buzea, I. I. Pacheco, and K. Robbie, “Nanomaterials and nanoparticles: Sources and toxicity,” *Biointerphases*, vol. 2, no. 4, pp. MR17–MR71, Dec. 2007, doi: 10.1116/1.2815690.

[112] E. A. Guliants, R. Schwarb, H. Bearbower, J. R. Gord, and C. E. Bunker, “Functional

nanoparticles in thin films as sensing media," *Rev. Adv. Mater. Sci.*, vol. 10, no. 4, pp. 289–294, 2005.

[113] N. Kundachira Subramani and Siddaramaiah, "Opto-Electrical Characteristics of Poly(vinyl alcohol)/Cesium Zincate Nanodielectrics," *J. Phys. Chem. C*, vol. 119, no. 35, pp. 20244–20255, Sep. 2015, doi: 10.1021/acs.jpcc.5b03652.

[114] A. B. El-Bially, R. Seoudi, W. Eisa, A. A. Shabaka, R. K. Abd El-Hamid, and R. A. Ramadan, "Preparation, characterization and physical properties of CdS nanoparticles with different sizes," *J. Appl. Sci. Res.*, vol. 8, no. 2, pp. 676–685, 2012.

[115] O. Mangla, A. Srivastava, Y. Malhotra, and K. Ostrikov, "Metal-insulator-metal capacitors based on lanthanum oxide high-κ dielectric nanolayers fabricated using dense plasma focus device," *J. Vac. Sci. Technol. B Microelectron. Nanom. Struct.*, vol. 32, no. 3, 2014, doi: 10.1116/1.4862093.

[116] C. Vatankhah and A. Ebadi, "Quantum Size Effects on Effective Mass and Band gap of Semiconductor Quantum Dots," *Res. J. Recent Sci.*, vol. 2, no. 1, pp. 21–24, 2013.

[117] H. Döllefeld, K. Hoppe, J. Kolny, K. Schilling, H. Weller, and A. Eychmüller, "Investigations on the stability of thiol stabilized semiconductor nanoparticles," *Phys. Chem. Chem. Phys.*, vol. 4, no. 19, pp. 4747–4753, 2002, doi: 10.1039/B202101C.

[118] J.-S. Lee, "Progress in non-volatile memory devices based on nanostructured materials and nanofabrication," *J. Mater. Chem.*, vol. 21, no. 37, p. 14097, 2011, doi: 10.1039/c1jm11050k.

[119] Z. Liu, C. Lee, V. Narayanan, G. Pei, and E. C. Kan, "Metal nanocrystal memories. I. Device design and fabrication," *IEEE Trans. Electron Devices*, vol. 49, no. 9, pp. 1606–1613, Sep. 2002, doi: 10.1109/TED.2002.802617.

[120] R. Bikky, N. Badi, and a Bensaoula, "Effective Medium Theory of Nanodielectrics for Embedded Energy Storage Capacitors," *Comsol.De*, pp. 1–9, 2010.

[121] J. K. Nelson and Y. Hu, "Nanocomposite dielectrics—properties and implications," *J. Phys. D. Appl. Phys.*, vol. 38, no. 2, pp. 213–222, Jan. 2005, doi: 10.1088/0022-3727/38/2/005.

[122] D. Yoo, M. S. Choi, S. C. Heo, C. Chung, D. Kim, and C. Choi, "Structural, optical and chemical analysis of zinc sulfide thin film deposited by RF-mganetron sputtering and post deposition annealing," *Met. Mater. Int.*, vol. 19, no. 6, pp. 1309–1316, Nov. 2013, doi: 10.1007/s12540-013-6026-7.

[123] A. N. Rodríguez, M. T. S. Nair, and P. K. Nair, "Structural, optical and electrical properties of chemically deposited silver sulfide thin films," *Semicond. Sci. Technol.*, vol. 20, no. 6, pp. 576–585, Jun. 2005, doi: 10.1088/0268-1242/20/6/017.

[124] S. Gedi, V. R. Minnam Reddy, C. Park, J. Chan-Wook, and R. R. K.T., "Comprehensive optical studies on SnS layers synthesized by chemical bath deposition," *Opt. Mater. (Amst).*, vol. 42, pp. 468–475, Apr. 2015, doi: 10.1016/j.optmat.2015.01.043.

[125] W. Li *et al.*, "Fabrication of CdSe/CdTe Quantum Dots Co-Sensitized TiO 2 Nanorods by Electrochemical Atomic Layer Deposition Method," *J. Electrochem. Soc.*, vol. 162, no. 4, pp. D137–D141, Jan. 2015, doi: 10.1149/2.0111504jes.

[126] R. González-Lúa, J. Escorcia-García, D. Pérez-Martínez, M. T. S. Nair, J. Campos, and

P. K. Nair, “Stable Performance of Chemically Deposited Antimony Sulfide-Lead Sulfide Thin Film Solar Cells under Concentrated Sunlight,” *ECS J. Solid State Sci. Technol.*, vol. 4, no. 3, pp. Q9–Q16, 2015, doi: 10.1149/2.0111503jss.

[127] A. B. F. Martinson, S. C. Riha, E. Thimsen, J. W. Elam, and M. J. Pellin, “Structural, optical, and electronic stability of copper sulfide thin films grown by atomic layer deposition,” *Energy Environ. Sci.*, vol. 6, no. 6, p. 1868, 2013, doi: 10.1039/c3ee40371h.

[128] S. Srinivasa Rao *et al.*, “Cobalt sulfide thin film as an efficient counter electrode for dye-sensitized solar cells,” *Electrochim. Acta*, vol. 133, pp. 174–179, Jul. 2014, doi: 10.1016/j.electacta.2014.04.010.

[129] K. Assili, K. Alouani, and X. Vilanova, “Structural and optical properties of tin (II) sulfide thin films deposited using organophosphorus precursor (Ph 3 PS),” *Semicond. Sci. Technol.*, vol. 32, no. 2, p. 025002, Feb. 2017, doi: 10.1088/1361-6641/32/2/025002.

[130] G. J. A. H. Wetzelaer and P. W. M. Blom, “Diffusion-driven currents in organic-semiconductor diodes,” *NPG Asia Mater.*, vol. 6, no. 7, pp. e110-13, 2014, doi: 10.1038/am.2014.41.

[131] O. V. Salata, P. J. Dobson, S. Sabesan, P. J. Hull, and J. L. Hutchison, “Preparation of nanoparticulate CdS films suitable for opto-electronic device applications,” *Thin Solid Films*, vol. 288, no. 1–2, pp. 235–238, Nov. 1996, doi: 10.1016/S0040-6090(96)08866-9.

[132] E. A. A. León Pérez *et al.*, “Indium-oxide nanoparticles for RRAM devices compatible with CMOS back-end-off-line,” *Solid. State. Electron.*, vol. 143, no. November, pp. 20–26, 2018, doi: 10.1016/j.sse.2017.11.011.

[133] A. Kiazadeh, H. L. Gomes, A. M. R. Da Costa, J. A. Moreira, D. M. De Leeuw, and S. C. J. Meskers, “Non-volatile memory device using a polymer modified nanocrystal,” *Mater. Sci. Eng. B Solid-State Mater. Adv. Technol.*, vol. 176, no. 19, pp. 1552–1555, 2011, doi: 10.1016/j.mseb.2011.01.021.

[134] S. Kolliopoulou *et al.*, “Field effect devices with metal nanoparticles integrated by Langmuir-Blodgett technique for non-volatile memory applications,” *J. Phys. Conf. Ser.*, vol. 10, no. 1, pp. 57–60, 2005, doi: 10.1088/1742-6596/10/1/015.

[135] S. Kolliopoulou *et al.*, “Hybrid silicon-organic nanoparticle memory device,” *J. Appl. Phys.*, vol. 94, no. 8, pp. 5234–5239, 2003, doi: 10.1063/1.1604962.

[136] R. Attota, P. P. Kavuri, H. Kang, R. Kasica, and L. Chen, “Nanoparticle size determination using optical microscopes,” *Appl. Phys. Lett.*, vol. 105, no. 16, p. 163105, Oct. 2014, doi: 10.1063/1.4900484.

[137] C. Gollwitzer *et al.*, “A comparison of techniques for size measurement of nanoparticles in cell culture medium,” *Anal. Methods*, vol. 8, no. 26, pp. 5272–5282, 2016, doi: 10.1039/C6AY00419A.

[138] F. Caputo, J. Clogston, L. Calzolai, M. Rösslein, and A. Prina-Mello, “Measuring particle size distribution of nanoparticle enabled medicinal products, the joint view of EUNCL and NCI-NCL. A step by step approach combining orthogonal measurements with increasing complexity,” *J. Control. Release*, vol. 299, no. February, pp. 31–43, Apr. 2019, doi: 10.1016/j.jconrel.2019.02.030.

[139] M. Baalousha, A. Prasad, and J. R. Lead, “Quantitative measurement of the nanoparticle size and number concentration from liquid suspensions by atomic force microscopy,” *Environ. Sci. Process. Impacts*, vol. 16, no. 6, pp. 1338–1347, 2014, doi: 10.1039/C3EM00712J.

[140] G. A. Dorofeev, A. N. Streletskii, I. V. Povstugar, A. V. Protasov, and E. P. Elsukov, “Determination of nanoparticle sizes by X-ray diffraction,” *Colloid J.*, vol. 74, no. 6, pp. 675–685, Nov. 2012, doi: 10.1134/S1061933X12060051.

[141] M. Ramrakhiani, “Luminescence of Cadmium Sulphide Nanoparticles and Nanocomposites,” vol. 3, pp. 15–22, 2013.

[142] V. A. Smyntyna, V. M. Skobeeva, K. A. Verheles, and N. V. Malushin, “Influence of Technology on the Formation of Luminescence Centers in CdS Quantum Dots,” *J. Nano- Electron. Phys.*, vol. 11, no. 5, pp. 05031-1-05031–4, 2019, doi: 10.21272/jnep.11(5).05031.

[143] K. A. Verheles, V. A. Smyntyna, V. M. Skobeeva, and N. V. Malushin, “The dependence of photoluminescence spectra of CdS QDs on stoichiometry,” *Visnyk Lviv Univ. Ser. Phys.*, vol. 56, no. July, p. 3, 2019, doi: 10.30970/vph.56.2019.3.

[144] A. Srivastava and H. L. Vishwakarma, “Photoluminescence of Chemically Synthesized CdS Nanoparticles,” *Int. J. Pure Appl. Phys.*, vol. 6, no. 3, pp. 347–351, 2010.

[145] V. Smyntyna and V. M. Skobeeva, “Influence of matrix on photoluminescence of CdS nanocrystals .,” no. 15, pp. 38–42, 2006.

[146] J. M. Cowley, *Surface and Interface Characterization by Electron Optical Methods*. Boston, MA: Springer US, 1989.

[147] S. Anu Mary Ealia and M. P. Saravanakumar, “A review on the classification, characterisation, synthesis of nanoparticles and their application,” *IOP Conf. Ser. Mater. Sci. Eng.*, vol. 263, no. 3, p. 032019, Nov. 2017, doi: 10.1088/1757-899X/263/3/032019.

[148] J. Roller, “X-Ray Diffraction,” in *Basic Elements of Crystallography*, Jenny Stanford Publishing, 2016, pp. 259–278.

[149] V. Sharma and L. J. M. Rao, “An Overview on Chemical Composition, Bioactivity and Processing of Leaves of Cinnamomum tamala,” *Crit. Rev. Food Sci. Nutr.*, vol. 54, no. 4, pp. 433–448, Jan. 2014, doi: 10.1080/10408398.2011.587615.

[150] G. S. Bumbrah and R. M. Sharma, “Raman spectroscopy – Basic principle, instrumentation and selected applications for the characterization of drugs of abuse,” *Egypt. J. Forensic Sci.*, vol. 6, no. 3, pp. 209–215, 2016, doi: 10.1016/j.ejfs.2015.06.001.

[151] B. F. Bory, J. Wang, H. L. Gomes, R. A. J. Janssen, D. M. De Leeuw, and S. C. J. Meskers, “Relation between the electroforming voltage in alkali halide-polymer diodes and the bandgap of the alkali halide,” *Appl. Phys. Lett.*, vol. 105, no. 23, 2014, doi: 10.1063/1.4903831.

[152] F. Verbakel *et al.*, “Reproducible resistive switching in nonvolatile organic memories,” *Appl. Phys. Lett.*, vol. 91, no. 19, p. 192103, Nov. 2007, doi: 10.1063/1.2806275.

[153] B. F. Bory, P. R. F. Rocha, H. L. Gomes, D. M. De Leeuw, and S. C. J. Meskers, “Unipolar resistive switching in metal oxide/organic semiconductor non-volatile memories as a critical phenomenon,” *J. Appl. Phys.*, vol. 118, no. 20, 2015, doi:

10.1063/1.4936349.

[154] K. T D and R. S P, “Studies on Synthesis and Electrical Properties of CdS-Polyaniline Nanocomposite via Oxidation Polymerization,” *Int. J. Compos. Mater.*, vol. 2, no. 4, pp. 44–47, 2012, doi: 10.5923/j.cmaterials.20120204.01.

[155] T. D. Kose and S. P. Ramteke, “Studies on Synthesis and Electrical Properties of CdS-Polyaniline Nanocomposite via Oxidation Polymerization,” *Int. J. Compos. Mater.*, vol. 2, no. 4, pp. 44–47, Aug. 2012, doi: 10.5923/j.cmaterials.20120204.01.

[156] S. S. Gasaymeh, S. Radiman, L. Y. Heng, and E. Saion, “Gamma irradiation synthesis and influence the optical and thermal properties of cadmium sulfide (CdS)/poly (Vinyl pyrolidone) nanocomposites,” *Am. J. Appl. Sci.*, vol. 7, no. 4, pp. 500–508, 2010, doi: 10.3844/ajassp.2010.500.508.

[157] E. Tian *et al.*, “A study of poly (sodium 4-styrenesulfonate) as draw solute in forward osmosis,” *Desalination*, vol. 360, no. March, pp. 130–137, Mar. 2015, doi: 10.1016/j.desal.2015.01.001.

[158] M. M. Heravi, M. Ghavidel, and L. Mohammadkhani, “Beyond a solvent: triple roles of dimethylformamide in organic chemistry,” *RSC Adv.*, vol. 8, no. 49, pp. 27832–27862, 2018, doi: 10.1039/C8RA04985H.

[159] V. M. Skobeeva, V. A. Smyntyna, O. I. Sviridova, D. A. Struts, and A. V. Tyurin, “Optical properties of cadmium sulfide nanocrystals obtained by the sol-gel method in gelatin,” *J. Appl. Spectrosc.*, vol. 75, no. 4, pp. 576–582, Jul. 2008, doi: 10.1007/s10812-008-9074-x.

[160] V. A. Smyntyna, V. M. Skobeeva, and M. V. Malushin, “Method for obtaining cadmium sulfide nanoparticles,” *Ukr. Pat. No. 29893*, 2008.

[161] H. P. and S. SotnikG., “Bistable Switching in Electroformed Metal-Insulator-Metal Devices,” *J. Mater. Sci. Lett.*, vol. 7, no. 11, pp. 1235–1236, Nov. 1988, doi: 10.1007/BF00722347.

[162] T. Menke, R. Dittmann, P. Meuffels, K. Szot, and R. Waser, “Impact of the electroforming process on the device stability of epitaxial Fe-doped SrTiO3 resistive switching cells,” *J. Appl. Phys.*, vol. 106, no. 11, 2009, doi: 10.1063/1.3267485.

[163] C. M. M. Rosário *et al.*, “Resistive switching and impedance spectroscopy in SiO -based metal-oxide-metal trilayers down to helium temperatures,” *Vacuum*, vol. 122, pp. 293–299, Dec. 2015, doi: 10.1016/j.vacuum.2015.05.007.

[164] F. Gomez-Marlasca, N. Ghenzi, M. J. Rozenberg, and P. Levy, “Understanding electroforming in bipolar resistive switching oxides,” *Appl. Phys. Lett.*, vol. 98, no. 4, p. 042901, Jan. 2011, doi: 10.1063/1.3537957.

[165] I. Salaoru, T. Prodromakis, A. Khiat, and C. Toumazou, “Resistive switching of oxygen enhanced TiO 2 thin-film devices,” *Appl. Phys. Lett.*, vol. 102, no. 1, p. 013506, Jan. 2013, doi: 10.1063/1.4774089.

[166] D. S. Jeong, B. J. Choi, and C. S. Hwang, “Electroforming Processes in Metal Oxide Resistive-Switching Cells,” in *Resistive Switching*, Weinheim, Germany: Wiley-VCH Verlag GmbH & Co. KGaA, 2016, pp. 289–316.

[167] T. W. Hickmott, “6 Electronic Phenomena, Electroforming, Resistive Switching, and

Defect Conduction Bands in Metal-Insulator-Metal Diodes," pp. 101–128, 2021.

[168] K. Szot, M. Rogala, W. Speier, Z. Klusek, A. Besmehn, and R. Waser, "TiO 2 —a prototypical memristive material," *Nanotechnology*, vol. 22, no. 25, p. 254001, Jun. 2011, doi: 10.1088/0957-4484/22/25/254001.

[169] A. Sawa, "Resistive switching in transition metal oxides," *Mater. Today*, vol. 11, no. 6, pp. 28–36, Jun. 2008, doi: 10.1016/S1369-7021(08)70119-6.

[170] P. Dimitrakis *et al.*, "Electrical behavior of memory devices based on fluorene-containing organic thin films," *J. Appl. Phys.*, vol. 104, no. 4, 2008, doi: 10.1063/1.2968551.

[171] T. W. Hickmott, "Čerenkov phonon radiation and phonon structure in electron emission, electroluminescence, and current-voltage characteristics of electroformed Al-Al2O3-Ag diodes," *J. Appl. Phys.*, vol. 127, no. 16, 2020, doi: 10.1063/1.5130758.

[172] Q. Chen *et al.*, "Opto-electronic characterization of electron traps upon forming polymer oxide memory diodes," *Appl. Phys. Lett.*, vol. 99, no. 8, pp. 2–4, 2011, doi: 10.1063/1.3628301.

[173] X. Zhou *et al.*, "Low-voltage inverted transparent vacuum deposited organic light-emitting diodes using electrical doping," *Appl. Phys. Lett.*, vol. 81, no. 5, pp. 922–924, 2002, doi: 10.1063/1.1496502.

[174] J. Werner, A. F. J. Levi, R. T. Tung, M. Anzlowar, and M. Pinto, "Origin of the Excess Capacitance at Intimate Schottky Contacts," *Phys. Rev. Lett.*, vol. 60, no. 1, pp. 53–56, Aug. 1988, doi: 10.1097/BRS.0b013e31813426fd.

[175] V. I. Boshernitsan, V. A. Smyntyna, V. M. Skobeeva, and N. V. Malushin, "Synthesis of CdS Nanocrystalsin the Gelatin Matrix with Different pH Values and their Optical Properties," *Phys. Chem. SOLID STATE*, vol. 16, no. 4, pp. 692–694, Dec. 2015, doi: 10.15330/pcss.16.4.692-694.

[176] Y. Wang and L. Chen, "Quantum dots, lighting up the research and development of nanomedicine," *Nanomedicine Nanotechnology, Biol. Med.*, vol. 7, no. 4, pp. 385–402, Aug. 2011, doi: 10.1016/j.nano.2010.12.006.

[177] W. W. Yu, L. Qu, W. Guo, and X. Peng, "Experimental Determination of the Extinction Coefficient of CdTe, CdSe and CdS Nanocrystals.," *Chem. Mater.*, vol. 16, no. 3, pp. 560–560, Feb. 2004, doi: 10.1021/cm033007z.

[178] V. Smyntyna, V. Skobeeva, and N. Malushin, "The nature of emission centers in CdS nanocrystals," *Radiat. Meas.*, vol. 42, no. 4–5, pp. 693–696, Apr. 2007, doi: 10.1016/j.radmeas.2007.01.068.

[179] V. Smyntyna, V. Boshernitsan, V. Skobeeva, and N. Malushin, "The influence of inter-phase physical and chemical processes on the optical properties of CdS nanocrystals in gelatin," *Electron. Inf. Technol.*, vol. 2, no. ISSN 2224-087X, pp. 51–56, 2012.

[180] V. A. Smyntyna, V. M. Skobeeva, K. A. Verheles, and M. V. Malushin, "Influence of Organic Molecules on the Luminescent Properties of Composites Based on CdS Quantum Dots," *Solid state Phys. Chem.*, vol. 18, no. 4, pp. 426–430, Dec. 2017, doi: 10.15330/pcss.18.4.430.

[181] V. Smyntyna, B. Semenenko, V. Skobeeva, and N. Malushin, "Photoactivation of

luminescence in CdS nanocrystals," *Beilstein J. Nanotechnol.*, vol. 5, no. 1, pp. 355–359, Mar. 2014, doi: 10.3762/bjnano.5.40.

[182] V. M. Skobeeva, V. A. Smyntyna, O. I. Sviridova, D. A. Struts, and A. V. Tyurin, "Optical properties of cadmium sulfide nanocrystals obtained by the sol-gel method in gelatin," *J. Appl. Spectrosc.*, vol. 75, no. 4, pp. 576–582, 2008, doi: 10.1007/s10812-008-9074-x.

[183] W. Wang, I. Germanenko, and M. S. El-Shall, "Room-Temperature Synthesis and Characterization of Nanocrystalline CdS, ZnS, and Cd x Zn 1 - x S," *Chem. Mater.*, vol. 14, no. 7, pp. 3028–3033, Jul. 2002, doi: 10.1021/cm020040x.

[184] S. R. Dhage, H. A. Colorado, and T. Hahn, "Morphological variations in cadmium sulfide nanocrystals without phase transformation," *Nanoscale Res. Lett.*, vol. 6, no. 1, p. 420, Dec. 2011, doi: 10.1186/1556-276X-6-420.

[185] D. Ayodhya, M. Venkatesham, A. S. Kumari, G. B. Reddy, D. Ramakrishna, and G. Veerabhadram, "Synthesis, Characterization, Fluorescence, Photocatalytic and Antibacterial Activity of CdS Nanoparticles Using Schiff Base," *J. Fluoresc.*, vol. 25, no. 5, pp. 1481–1492, Sep. 2015, doi: 10.1007/s10895-015-1639-5.

[186] A. Rasool, T. Z. Rizvi, S. Nayab, and Z. Iqbal, "Electrical properties of Cadmium Sulfide quantum dots and polyaniline based nanocomposites," *J. Alloys Compd.*, vol. 854, p. 156661, Feb. 2021, doi: 10.1016/j.jallcom.2020.156661.

[187] K. A. Svit *et al.*, "Crystal Structure and Predominant Defects in CdS Quantum Dots Fabricated by the Langmuir–Blodgett Method," *Langmuir*, vol. 37, no. 18, pp. 5651–5658, May 2021, doi: 10.1021/acs.langmuir.1c00526.

[188] B. Vaishnavi, T. Sreelakshmi, M. K. Rahina, M. S. Murari, and R. M. Pattabi, "Enhancing the photocatalytic efficiency of CdS nanostructures by ZnS: A case study on the degradation of methylene blue," *Mater. Today Proc.*, no. 3, Jul. 2023, doi: 10.1016/j.matpr.2023.07.001.

[189] S. K. Saha, "Nanodielectrics with giant permittivity," *Bull. Mater. Sci.*, vol. 31, no. 3, pp. 473–477, Jun. 2008, doi: 10.1007/s12034-008-0074-5.

[190] M. Fréchette, "Reflecting on Material Trends: the Case of Nanodielectrics," in *Proceedings of the Symposium on Electrical and Electronic Insulating Materials and Applications in Systems*, 2004, vol. 35, no. April, pp. 25–32.

[191] S. Zhong, Z. Dang, W. Zhou, and H. Cai, "Past and future on nanodielectrics," *IET Nanodielectrics*, vol. 1, no. 1, pp. 41–47, Apr. 2018, doi: 10.1049/iet-nde.2018.0004.

[192] A. S. Vaughan, "Nanodielectrics: The Role of Structure in Determining Electrical Properties," in *Controlling the Morphology of Polymers*, no. January 2010, Cham: Springer International Publishing, 2016, pp. 237–262.

[193] K. Stallings *et al.*, "Systematic Analysis of Self-Assembled Nanodielectric Architecture and Organization Effects on Organic Transistor Switching," *ACS Appl. Electron. Mater.*, vol. 4, no. 4, pp. 2015–2025, Apr. 2022, doi: 10.1021/acsaelm.2c00177.

[194] S. A. DiBenedetto, I. Paci, A. Facchetti, T. J. Marks, and M. A. Ratner, "High-Capacitance Organic Nanodielectrics: Effective Medium Models of Their Response," *J. Phys. Chem. B*, vol. 110, no. 45, pp. 22394–22399, Nov. 2006, doi: 10.1021/jp062096a.

[195] D. Xiang, J. Wu, and R. Gordon, “Coulomb Blockade Plasmonic Switch,” *Nano Lett.*, vol. 17, no. 4, pp. 2584–2588, Apr. 2017, doi: 10.1021/acs.nanolett.7b00360.

[196] H. Dhaouadi, O. Ghodbane, F. Hosni, and F. Touati, “Nanoparticles: Synthesis, Characterization, and Dielectric Properties,” *ISRN Spectrosc.*, vol. 2012, pp. 1–8, Feb. 2012, doi: 10.5402/2012/706398.

[197] Y. Suzuki *et al.*, “Kinetics of Distance-Dependent Recombination between Geminate Charge Carriers by Diffusion under Coulomb Interaction,” *J. Phys. Chem. C*, vol. 119, no. 10, pp. 5364–5373, Mar. 2015, doi: 10.1021/acs.jpcc.5b00417.

[198] S.-Y. Ji *et al.*, “Enhanced Energy Storage Performance of Polymer/Ceramic/Metal Composites by Increase of Thermal Conductivity and Coulomb-Blockade Effect,” *ACS Appl. Mater. Interfaces*, vol. 13, no. 23, pp. 27343–27352, Jun. 2021, doi: 10.1021/acsami.1c01177.

# List of Publications


1. V. I. Boshernitsan, “Luminescence of ZnSe:Fe crystals”, Proceedings of 66th Scientific Conference of the Odessa I. I. Mechnikov National University, 2010.
2. V. Boshernitsan, Y. Vaksman, V. Yatsun, E. Beregnoy, “ZnT:Ni crystals as a material for photorefractors”, *Sensor’s electronics and microsystems technology (SEMST-4)*, 2010. http://dspace.onu.edu.ua:8080/handle/123456789/585
3. V. I. Boshernitsan, “Photoconductivity and optical properties of single crystals of ZnSe:Fe,Ni”, Proceedings of 67th Scientific Conference of the Odessa I. I. Mechnikov National University, 2011.
4. V. Boshernitsan, V. Smyntyna, V. Skobeeva, N. Malushin, “Influence of interfacial physic-chemical processes in the optical properties of CdS nanocrystals in gelatin” Proceedings of the International Conference of students and young researchers in theoretical and experimental physics Eureka 2012, Lviv, Ukraine, - p.6.
5. V. Smyntyna, V. Boshernitsan, V. Skobeeva, and N. Malushin, “The influence of interphase physical and chemical processes on the optical properties of CdS nanocrystals in gelatin,” *Electronics and Information Technology*, vol. 2, no. ISSN 2224-087X, pp. 51–56, 2012.
6. V. Boshernitsan, V. Smyntyna, V. Skobeeva, N. Malushin, “Effect of pH on the synthesis of nanocrystals of cadmium sulfide and their optical properties” Proceedings of the International Conference of students and young researchers in theoretical and experimental physics Eureka 2013.
7. V.I. Boshernitsan, “Synthesis and optical properties of CdS nanocrystals in a gelatin matrix with different values of pH of the solution” Physics, Electronics, Electrical materials and application of scientific and technical conferences, Sumy, 2013, p. 72, http://essuir.sumdu.edu.ua/handle/123456789/43862
8. V. Boshernitsan, V. Smyntyna, V. Skobeeva, H. L. Gomes, “Electrical characterization of CdS quantum dots embedded in polymer matrix”, Proceedings of the International Conference of students and young researchers in theoretical and experimental physics Eureka 2014.

9. V. Smyntyna, V. Boshernitsan, V. Skobeeva, N. Malushin “Influence of pH solution on the synthesis of nanocrystals and their optical properties” *Electronics and Infor- mation Technology*, Issue 3, 2014, pp. 74-80.
10. V. Boshernitsan “Morphological and structural characterization of CdS nanoparticles in different insulating polymer matrices” Proceedings of the International Conference of students and young researchers in theoretical and experimental physics Eureka 2015.
11. V. Boshernitsan, V. Smyntyna, V. Skobeeva, N. Malushin “Synthesis of CdS Nanocrystals in the Gelatin Matrix with Different pH Values and their Optical Properties”, *Physics and Chemistry of Solid State,* 2015, №4, vol. 16, pp.692-694. https://doi.org/10.15330/pcss.16.4.692-694
12. V.I. Boshernitsan, “Synthesis of cadmium sulfide nanoparticles embedded in polymer matrices and fabrication of electronic devices based on it”, *Chemistry and chemical technology issues – Vhht.* 2016, vol. 2 (106). UDK 546. ISSN 0321-4095.
13. V. Boshernitsan, S. C. J. Meskers, D. M. de Leeuw and H. L. Gomes, “Resistive switching memories based on metal oxide-polymer interfaces: insight into the microscopic switching mechanism” Materials 2019, Portugal.
14. V. Boshernitsan, “Nanodielectrics based on CdS nanoparticles”, proceedings of the International Conference of students and young researchers in theoretical and experimental physics Heureka 2020.
15. V. Boshernitsan, “Nanoparticle-based electronic devices”, International students and young scientists conference in theoretical and experimental physics, Heureka 2021.
16. V. Boshernitsan, “Establishment of formation mechanisms for optical and electrophysical properties of nanofilms of CdS’’, the presentation in a section “Nanomaterials and Nanotechnology”. International students and young scientists conference in theoretical and experimental physics, Heureka 2023.